

https://dspace.org/

Structuring light to control photon entanglement

Lovemore, Michael Andrew Charles

2022
University of the Witwatersrand, Johannesburg
https://hdl.handle.net/10539/34557
Lovemore, Michael Andrew Charles. (2022). Structuring light to control photon entanglement. [Master's dissertation, University of the Witwatersrand, Johannesburg]. WIReDSpace. https://hdl.handle.net/10539/34557

Downloaded from a DSpace repository. https://dspace.org/



UNIVERSITY OF THE WITWATERSRAND

MASTERS THESIS

STRUCTURING LIGHT TO CONTROL PHOTON ENTANGLEMENT

Author:
Michael Andrew Charles
LOVEMORE

Supervisor:
Prof. Andrew FORBES

A project submitted in fulfillment of the requirements
for the degree of Masters in Physics

in the

Structured Light Laboratory
School of Physics
Natural Science

May 18, 2022

Abstract of report entitled

STRUCTURING LIGHT TO CONTROL PHOTON ENTANGLEMENT

Submitted by

Michael Andrew Charles LOVEMORE

for the degree of Masters in Physics

at The University of the Witwatersrand

in May, 2022

Photon entanglement, either spatially, temporally, or even in terms of its polarization, has become an increasingly important field of interest in the world of quantum mechanics. The importance becomes apparent when looking at quantum protocols such as quantum teleportation, communication, and quantum information. These entangled photons are often generated through a well known non-linear process known as spontaneous parametric down-conversion (SPDC), where a high-energy pump beam impinges on a non-linear crystal and generates two lower energy down-converted entangled photons. The intensity and phase profile of the pump beam influences the dimension of entanglement that exists between the two generated photons. This pump beam shape can be altered through the use of optical devices such as spatial light modulators (SLMs) in order to achieve desired entanglement spectra. This dissertation serves as an introduction to structured light and photonics with an emphasis on the spatial modes of light and the intersection of quantum mechanics with optics. A description concerning the tailoring of the field of light with spatial light modulators is presented. These SLMs are also useful when measuring some properties related to entangled photons. Some of the quantum measurements that are discussed here include the spiral bandwidth, Bell measurements, and quantum state tomography measurements. Lastly, some novel work is presented, where we demonstrate a basis-independent approach to shaping the pump beam, in order to achieve a desired entanglement spectrum.

STRUCTURING LIGHT TO CONTROL PHOTON ENTANGLEMENT

by

Michael Andrew Charles LOVEMORE

A project Submitted in Fulfilment
of the Requirements for the Degree of
Masters in Physics

at

University of the Witwatersrand
May, 2022

Declaration

I, Michael Andrew Charles LOVEMORE, declare that this project titled, "STRUCTURING LIGHT TO CONTROL PHOTON ENTANGLEMENT", which is submitted in fulfillment of the requirements for the Degree of Masters in Physics, represents my own work except where due acknowledgement has been made. I further declare that it has not been previously included in a thesis, dissertation, or report submitted to this University or to any other institution for a degree, diploma or any other qualifications.

Signed: *Michael Andrew Charles Lovemore*

Date: May 18, 2022

Dedicated to my Mother and Father

Acknowledgements

I would like to thank Prof. Andrew Forbes for the effort, dedication, willingness and guidance that was offered toward me during the course of the preparation and construction of this thesis. I would also like to thank him for putting up with me and teaching me to realize what has to be understood and applied when. A thank you also goes out to Doctor Wagner Tavares Buono who has consistently been approachable and willing to put in the time to explain concepts to me until I understand it.

I want to thank my best friend, Liam Botha, for picking me up off the floor countless times, pushing me to do my best, staying by my side through all this time and being the brother he is. I also thank Donovan Slabbert for the chess and jokes and the countless meals at the post graduate club. I would like to thank and dedicate this project to my mother, Ronel Lovemore, and father, Rowan Lovemore, who have both been the biggest cornerstones in my life. Consistently motivating me to succeed, helping me with all the late nights of homework, all the love and cherishing they gave me, guiding me to be who I am today and most of all, I want to thank them for being by my side, no matter what my decision, supporting me and guiding me along the way in life. I would like to also thank my grannymother, grannyfather, ouma, oupa for helping me mentally, physically and by challenging me to do and learn my best. I would like to thank my brother, for checking in on me and helping me whenever I need, and keeping our brotherly bond strong. Lastly, I would like to thank my girlfriend Esmari Strydom, for keeping me strong in times of need, pushing me to perfect everything I do, and I want to thank her for being by my side no matter what.

Michael Andrew Charles LOVEMORE
University of the Witwatersrand
May 18, 2022

List of Figures

1.1 **Hermite-Gaussian modes:** These are the intensity profiles (left) and phase profiles (right) of the Hermite-Gaussian modes. They are respectively determined by the equations from before, (1.15) and (1.16). A trend can be seen where the n index dictates the amount of dark nodes in the horizontal direction and m the amount of dark nodes in the vertical direction [10]. 5

1.2 **Twisting OAM wavefront:** This shows what is meant by the twisting of light. The wavefront forms a helix about the direction of propagation. It can easily be noticed that for $\ell = 1$ ($a.$), the helix spirals clockwise and for $\ell = -1$ ($b.$) the helix spirals anti-clockwise. 7

1.3 **Laguerre-Gaussian modes:** The left side in each image represents the intensity profile of the LG beam, while the right side represents the phase profile. It is clearly noticeable that the intensity profile is the same for ℓ values of opposite sign, but the phase profiles are not. The optical vortex also becomes larger for a higher topological charge ℓ, and when we increase the radial index p, rings are added around the initial doughnut structure. 7

1.4 **Electric and magnetic field oscillation:** The electric ($\bar{E}$) and magnetic fields ($\bar{B}$) oscillate perpendicular to one another, and the direction of propagation ($\hat{z}$). 11

1.5 **Poincaré sphere:** By setting $\theta = 0$ with $\phi = 0$, and examining the sphere, the state corresponding to right circular polarization is realized. This logic can be repeated for all other states by simply searching for the desired polarization state on the surface of the sphere, and reading off the respective corresponding θ and ϕ values. 12

2.1 **Liquid crystal rotation:** The effective extraordinary index of refraction varies as the rotation angle changes. The choice for the refractive indices, merely for demonstrative purposes, were $n_e = 1.7$ and $n_o = 1.5$. This rotation angle is further affected by the applied voltage to the liquid crystals. There is clearly a minimum and maximum value for the refractive index corresponding to different rotations of the liquid crystal. 25

2.2 **SLM setup:** The object plane (represented by the red star) on the right is imaged by means of a telescope (T_1), consisting of lenses L_1 and L_2, onto the SLM. This object plane is then further imaged by telescope T_2 to the next object plane (star at the bottom of the image). The aperture is placed between lenses L_3 and L_4 for the purpose of spatial filtering. 27

2.3 **Phase and Amplitude Modulation:** The green circle shows the unitary circle that defines phase only modulation. To perform the amplitude modulation as well involves moving to a point within this circle (the brown dot) say between two points A and B. This can be generalized for any position within the circle allowing one to effectively modulate to attain any phase and amplitude required. 28
2.4 **Calibration setup:** It can be seen here that an expanded beam passes through a double pinhole, creating two thinner beams hitting either side of the SLM and reflecting off of it. These two beams pass through the same lens and focuses to the same point, at which a CCD camera is placed. 31
2.5 **Shifting fringes during calibration:** The red crosshair represents the reference point about which the fringes shift. The goal is to set the voltages of the SLM such that with a 2π phase shift, the crosshair appears on the bright fringe next to the initial one. These images show the crosshair at various locations as the phase shift was changed. The phase shifts in a, b, c, d, and e are $0, 0.5\pi, \pi, 1.5\pi$, and 2π respectively. 32
2.6 **Zernike modes:** These represent the contribution of the main lower order Zernike modes to what the wavefront would like. These are thus also the modes one would adjust to correct for the corresponding abberation. The Z_0^0 mode is usually referred to as the piston mode. When one would like to correct for squashing in either the vertical or horizontal direction, the y-tilt (Z_1^{-1}) and x-tilt (Z_1^1) is respectively adjusted. To correct for astigmatism either the Z_2^{-2} mode or Z_2^2 mode is adjusted, and if the aberration occurs in the centre, the defocus (Z_2^0) is used [44, 45]. 33
2.7 **Generated modes:** Each of these images shows a different mode to which the light intensity profile was shaped. The holograms corresponding to the modulated modes, other than the Gaussian mode, is given on the inset of each image. 34

3.1 **Spontaneous Parametric Down Conversion:** The concept of SPDC is illustrated as well as the momentum and energy conservation between the signal, idler, and pump beams. 37
3.2 **Theoretical spiral bandwidth plots:** The concept of the OAM spectrum is depicted here. This is for the case when $\ell_p = 0$. As discussed, the probability is maximum at the centre when $\ell_s = \ell_i = 0$ and drops off for higher order modes. The reason that we only have an anti-diagonal in a. in this case is due to the restriction imposed on the values of ℓ_s and ℓ_i. Since there are only elements along the anti-diagonal, it is easy to visualize a 2D cross-sectional probability distribution as show in b. 41
3.3 **Bloch Sphere:** This demonstrates what is meant by the Bloch sphere. The states on the surface of the Bloch sphere represent the state of the photon. The substates $|\ell\rangle$ are used since one works in the OAM subspace. 44

3.4 **Bell Measurement:** This is a simulated perfect Bell measurement case displaying the trend of the bell measurement curve. The normalized coincidence counts would usually be plotted as a function of the relative angle between the superposition of OAM states. The θ_s (corresponding to the signal photons hitting its SLM) values are kept at a constant value, while the θ_i (corresponding to the idler photons hitting its SLM) values are varied. This is done for four cases of $\theta_s = \{0, \frac{\pi}{4}, \frac{\pi}{2}, \frac{3\pi}{4}\}$. 46

3.5 **Higher Order Bloch Sphere:** This depicts what is meant by the higher order Bloch sphere. The states on the surface of the first two Bloch spheres represent the state of each individual photon respectively. The substates $|\ell\rangle$ are used since the OAM subspace is used. 47

3.6 **Two-Dimensional QST:** This shows the full tomography measurement of the coincidence counts of an entangled two-photon system, projected into the measurement states corresponding to the given phase maps $(a.)$, as well as the real $(b.)$, and imaginary $(c.)$ components of the density matrix. 50

3.7 **4-dimensional QST:** This shows the complete QST measurement $(a.)$ for a four-dimensional ($\ell = \{-2, -1, 1, 2\}$) case of a two-photon entangled system. The block in $(c.)$ represents the four pure states (The bras and kets are omitted for notational simplicity). Each mini block indicates the normalized coincidence counts for the corresponding states. The block in $(b.)$ shows how the QST measurement can be read, in terms of the superposition of two states. The equations in $(a.)$ display the superposition OAM states that correspond to each curly bracket. 51

4.1 **Experimental setup:** The labels f_i refer to the lenses used in the setup. They are set up in pairs of two to work as a telescope imaging system. HWP 1 and 2 refer to the half wave plates before the crystal and SLM respectively. NLC is the non-linear crystal which in this case was a PPKTP crystal. BS is the beam splitter, and the two orange boxes before the fibres and fibre couplers are the $810nm$ bandpass filters which allow only photons with that wavelength to pass through. 52

4.2 **Reciprocity of light:** Passing a Gaussian through a hologram would result in a particular desired mode. When reversing the procedure, and passing this mode through the hologram with the conjugate phase of the current mode encoded on it, the returned mode would then be a Gaussian again. 53

4.3 **Crystal temperature:** The evolution of the down-converted photons, in a room with an ambient temperature of $18°C$, is shown as the temperature is altered. $a.$ represents temperatures from $49°C - 53°C$, $b.$ from $54°C - 58°C$, and $c.$ from $59°C - 63°C$. As the temperature increases, the trend noticed is that the region of light occupies a smaller region on the camera, this means that the two down-converted beams becomes more and more collinear. In our experiment, the optimal choice was when the temperature reached $61°C$. This was chosen because the physical profile of the light had a larger cross-sectional area at the chosen temperature, which allowed for more higher order modes to be detected. 56

4.4 **Temperature dependence:** In *a*. the relationship between the quantum contrast and temperature is shown while in *b*. the relationship between the coincidence counts and temperature is shown. 56
4.5 **Integration time dependence:** In *a*. the plot of the quantum contrast vs the integration time is shown. In *b*. the numbers of coincidences per second is plotted against the integration time. In *c*. a plot of the total coincidence counts as a function of the changing integration time can be seen. 57
4.6 **Gating time dependence:** In *a*. a plot of the quantum contrast as a function of the gating time is shown, while *b*. shows the plot of the coincidences as a function of the gating time. 58
4.7 **Spiral bandwidth for $\ell = \{-5, 5\}$:** *a*. displays the OAM intensity spectrum when the measurement is made in a completely dark room. In *b*. one can see an OAM intensity spectrum where external light sources have been introduced. The spiral bandwidth for the 'good' case (shown in *a*.) is shown in *c*. 60
4.8 **Accidental component of the coincidence counts:** *a*. gives an indication of the spiral bandwidth with the accidentals not being removed from the data. *b*. shows what the spectrum of only the accidental coincidences looks like. Clearly the contribution of the accidentals cannot be noticed by simply examining the spectrum from **Figure** 4.7 *c*. One has to explicitly aim to notice this contribution which could potentially result in a large error if this is not accounted for. 60
4.9 **Cross-sections of the $\ell = \{-5, 5\}$ spectrum:** The cross-section in *a*. shows the well defined peak at $\ell_s = 0$, where the cross-section has also been created by looking at the elements corresponding to $\ell_i = 0$. It can be seen that most elements, other than the peak, is near but not precisely at 0. The same trend can be seen in *b*. only this time with the defined peak at $\ell_s = -5$ for the cross-section about $\ell_i = 5$. 61
4.10 **Spiral bandwidth analysis for $\ell = \{-15, 15\}$:** *a*. is once again the OAM intensity spectrum and *b*. is the corresponding spiral spectrum for the entangled photons. *c*. shows the spectrum when the accidentals are included in the data set and *d*. is the spectrum showing the contribution of only the accidentals. Cross-sections of the spiral bandwidths about $\ell_i = 0$ and $\ell_i = -10$ is shown in *e*. and *f*. respectively. . . 62
4.11 **Spiral bandwidth analysis for $\ell = \{-25, 25\}$:** The OAM intensity spectrum is presented in *a*. while *b*. shows the corresponding spiral spectrum. In *c*. and *d*. one can see the spiral spectrum of the total coincidences and accidentals respectively. The spectrum of the cross-section about $\ell_i = 0$ is shown in *e*., and about $\ell_i = 10$, whose corresponding highest peak is at $\ell_s = -10$, is shown in *f*. 62
4.12 **Bell measurements using the CHSH inequality:** These results show the normalized coincidence counts plotted as a function of the θ_i values while keeping the θ_s values constant as shown in the legends. This is done for the $|\ell| = 1$ subspace in *a*. and the $|\ell| = 2$ subspace in *b*. 63
4.13 **2D QST:** This figure shows a QST measurement, as well as the reconstructed real and imaginary density matrices for the basis states $\ell = 1$ and $\ell = -1$. The blocks with labels 0, $\frac{\pi}{4}$, $\frac{\pi}{2}$, and $\frac{3\pi}{4}$ correspond to the phase difference between the superposition states (blocks with 1 and -1). 64

4.14 **3D QST:** A 3D QST measurement is displayed with its corresponding density matrices. The labels denoted with square brackets show which OAM states are superpositioned with one another. 65
4.15 **4D QST:** A 4D QST and its density matrices are shown here. 66

5.1 **LG spectrum from $\ell_{s,i} = -4$ to $\ell_{s,i} = 4$:** The desired spectrum with equalized coefficients $C_{-4,-4} = C_{-2,-2} = C_{0,0} = C_{2,2} = C_{4,4} = \frac{1}{\sqrt{5}}$ is shown here. 73
5.2 **LG pump profile:** The requisite pump profile for the chosen desired coefficients $C_{-4,-4} = C_{-2,-2} = C_{0,0} = C_{2,2} = C_{4,4} = \frac{1}{\sqrt{5}}$. 74
5.3 **HG spectrum from $m_{s,i} = 0$ to $m_{s,i} = 8$:** The desired spectrum with coefficients $C_{0,0} = C_{1,1} = C_{2,2} = C_{3,3} = C_{4,4} = C_{5,5} = C_{6,6} = C_{7,7} = C_{8,8} = \frac{1}{\sqrt{9}}$ is shown here. . 75
5.4 **HG pump profile:** The pump profile for the chosen desired spectrum whose coefficients are given by $C_{0,0} = C_{1,1} = C_{2,2} = C_{3,3} = C_{4,4} = C_{5,5} = C_{6,6} = C_{7,7} = C_{8,8} = \frac{1}{\sqrt{9}}$. 75

Contents

Abstract i

Declaration

Acknowledgements ii

List of Figures iii

Preface x

1 Quantum mechanics and spatial modes of light 1

1.1 Schrödinger equation and spatial modes of light . . . 1
1.1.1 Schrödinger equation . . . 1
1.1.2 Paraxial wave equation . . . 3
1.1.3 Spatial modes of light . . . 4
1.2 The wave vector and some simple mathematical quantities . . . 8
1.3 The Hilbert Space . . . 9
1.4 Polarization . . . 10
1.5 Mixed and Pure States . . . 12
1.6 Density Matrix . . . 13
1.7 Reduced Density Matrix . . . 16
1.8 Concept of factorability and quantum entanglement . . . 17
1.9 Measures of Entanglement - Entropy . . . 18
1.9.1 Shannon Entropy . . . 19
1.9.2 Other classical information measures using Entropy . . . 19
1.9.3 Von-Neumann Entropy . . . 20
1.9.4 Linear Entropy . . . 21
1.10 Measures of entanglement - Concurrence . . . 22
1.10.1 Concurrence . . . 22
1.11 Fidelity . . . 23

2 Techniques to shape and structure light 24

2.1 Spatial Light Modulators (SLMs) . . . 24
2.1.1 What is an SLM and how does it work? . . . 24
2.1.2 Encoding a hologram . . . 26
2.1.3 Calibration of an SLM . . . 30

2.1.4 Investigating the efficiency of an SLM . . . 31
2.2 Aberrations . . . 32
2.2.1 Zernike polynomials . . . 32
2.3 Generated modes using an SLM . . . 33
2.4 Chapter conclusion . . . 34

3 Understanding entangled photons **35**
3.1 Spontaneous parametric down-conversion . . . 35
3.1.1 Phase Matching Conditions . . . 35
3.1.2 SPDC Quantum State . . . 37
3.2 Spiral Bandwidth . . . 39
3.3 Bell Measurement . . . 41
3.3.1 Understanding the origins of entanglement - CHSH inequality . . . 41
3.3.2 CHSH inequality . . . 43
3.4 Quantum State Tomography . . . 45
3.4.1 Theory of QST . . . 46
3.4.2 Extracting information from QST measurements . . . 49
3.5 Chapter conclusion . . . 51

4 Building a quantum optical setup **52**
4.1 Physics of building the setup . . . 52
4.2 Possible practical limitations . . . 54
4.3 Establishing control over the setup . . . 55
4.3.1 Temperature: . . . 55
4.3.2 Integration Time: . . . 57
4.3.3 Gating time: . . . 57
4.4 Measurement results . . . 58
4.5 Chapter conclusion . . . 66

5 Pump Shaping and Entanglement Control **68**
5.1 Theory and mathematics . . . 69
5.1.1 LG basis . . . 72
5.1.2 HG basis . . . 73
5.2 Chapter conclusion . . . 76

6 Conclusion **77**

Preface

This thesis is structured for coherence from start to finish, to allow the skills used in later chapters, to be introduced and understood in earlier chapters. The aim is to introduce key concepts crucial to photonics and structured light, but relevant to a quantum optics interpretation. The first chapter introduces these structured light concepts and describes the spatial modes of light, as well as a few basic mathematical formulae related to quantum optics and quantum entanglement.

Since this field is dependent on structuring light, a quintessential skill is realizing how one can physically perform this tailoring of the field of light. This is the intention of the second chapter, to understand how to shape light, with an emphasis on spatial light modulators (SLMs). These SLMs are useful, not only for shaping light, but to measure some properties related to quantum optics. Arguably, the most important of these properties is that two photons can be entangled with one another through a process of spontaneous parametric down-conversion (SPDC). This is the key focus of the third chapter, using the mathematics introduced in chapter 1, and the skills of shaping light with SLMs from chapter 2, to entangle photons and take measurements on these entangled photon states. Some of the measurements highlighted here include the spiral bandwidth, a Bell measurement (which verifies the entanglement of the photons), and a quantum state tomography measurement.

Chapter 4 is an experimental realization of the quantum concepts introduced in chapter 3, with an emphasis on gaining full control over the different parameters in a quantum optics experiment. The final chapter presents novel work related to controlling the entanglement in an experiment by shaping the light for a desired outcome.

Chapter 1

Quantum mechanics and spatial modes of light

This chapter aims to familiarize the reader with a few topical concepts pertaining to the thesis as a whole. A general overview concerning these concepts is presented, with an emphasis on the related mathematical quantities, if any, which is also specified for relevance. The key takeaways from this chapter include the following:

- Understanding what is meant by the spatial modes of light and how to define these spatial modes mathematically,
- knowing how to determine the state of a quantum system, both mixed and pure, using the density matrix formulation,
- realizing what is meant by entanglement and hence being able to determine whether a system is entangled or not, and
- being able to make a measure of the degree of entanglement of a quantum system.

1.1 Schrödinger equation and spatial modes of light

This section guides the reader through the interpretation of the wave equation and the formulation of the paraxial wave equation. The latter is important to find the relevant spatial modes of light.

1.1.1 Schrödinger equation

The Schrödinger equation describes the evolution of the wave function (essentially as a probability evolution). The Schrödinger equation is formulated as a partial differential equation given by:

$$\left[\frac{-\hbar^2}{2m}\nabla^2 + V(\mathbf{r})\right]\Psi(\mathbf{r},t) = i\hbar\frac{\partial}{\partial t}\Psi(\mathbf{r},t), \tag{1.1}$$

where

$$\nabla = (\frac{\partial}{\partial x}, \frac{\partial}{\partial y}, \frac{\partial}{\partial z}), \tag{1.2}$$

is a vector differential operator,

$$\hbar = \frac{h}{2\pi}\ , \tag{1.3}$$

is a modified version of Planck's constant (h) known as the reduced Planck's constant, $\mathbf{r} = (x, y, z)$ is the position vector, V is a time-independent potential that the system is subjected to, and $\Psi(\mathbf{r}, t)$ is the wave function defining the state of the system.

This is the mathematical definition for the wave equation which depends on spatial and temporal coordinates. By performing separation of variables, $\Psi(\mathbf{r}, t) = \psi(\mathbf{r})T(t)$, the Schrödinger equation can be simplified to a time-independent form:

$$\left[\frac{-\hbar^2}{2m}\nabla^2 + V(\mathbf{r})\right]\psi(\mathbf{r}) = \mathbb{E}\psi(\mathbf{r}). \tag{1.4}$$

This equation can be seen as a tool used to describe the permitted energy levels of a quantum system [1]. By using the Hamiltonian operator,

$$H = \frac{-\hbar^2}{2m}\nabla^2 + V(\mathbf{r}), \tag{1.5}$$

the Schrödinger equation can be written as,

$$H\psi(\mathbf{r}) = \mathbb{E}\psi(\mathbf{r}), \tag{1.6}$$

which now becomes an eigenvalue problem with the Hamiltonian operator operating on the wave function. Solving this differential Eq. (1.6), returns an eigenstate $\psi(\mathbf{r})$ with a corresponding eigenvalue $\mathbb{E}$ - the energy of the system. There are almost always multiple solutions for this eigenstate ($\psi_n(\mathbf{r})$), with its corresponding eigenvalues ($\mathbb{E}_n$).

Quantum mechanics is an extensively researched field in physics and there have been many different attempts to explain how the mathematical theory of quantum mechanics maps to reality. The interpretation used in this dissertation is that proposed by Bohr and Heisenberg - the Copenhagen interpretation. In this interpretation, the most general wave function describing the state of a system is said to be described by the superposition of all the possible eigenstates of the eigenvalue problem given in Eq. (1.6) [2]:

$$\psi_{sys} = \sum_n c_n \psi_n(\mathbf{r}). \tag{1.7}$$

In this superposition, each state ($\psi_n(\mathbf{r})$) is multiplied with a coefficient (c_n) , whose squared norm ($|c_n|^2$) can be interpreted as the probability of finding an outcome of a particular measurement [3, 4], for instance by making an energy measurement on the system, one would notice a returned value of $\mathbb{E}_n$ with a corresponding probability of $|c_n|^2$. Each Hermitian operator ($\hat{A} = \hat{A}^\dagger$) has its own corresponding observable that is analogous to measurable quantities in classical mechanics, such as the momentum or angular momentum of a classical system.

When one considers the wave function $|\psi(\mathbf{r})\rangle$ to be a finite-dimensional vector, the Hamiltonian operator will be a matrix. To determine the eigenvalues with each corresponding probability would require this Hamiltonian matrix to be diagonalized.

1.1.2 Paraxial wave equation

Consider the electric field of an electromagnetic wave to be given by E. The three dimensional wave equation for this electric field , derived from Maxwell's equations [3], is represented by

$$\nabla^2 \mathrm{E}(\mathbf{r}, t) - \frac{1}{c^2} \frac{\partial^2 \mathrm{E}(\mathbf{r}, t)}{\partial t^2} = 0, \tag{1.8}$$

and by utilizing separation of variables with $\Psi(\mathbf{r}, t) = \mathrm{E}(\mathbf{r})T(t)$ one finds:

$$(\nabla^2 + k^2)\mathrm{E}(\mathbf{r}) = 0, \tag{1.9}$$

with $k^2 = -\frac{1}{c^2 T} \frac{d^2 T}{dt^2}$. This is known as the Helmholtz equation [5].

One solution to this Helmholtz equation can be found by choosing the k^2 term to be written in terms of energies as follows,

$$\left[\nabla^2 - \frac{2m(V(\mathbf{r}) - \mathbb{E})}{\hbar^2}\right] \mathrm{E}(\mathbf{r}) = 0, \tag{1.10}$$

where $k^2 = -\frac{2m(V(\mathbf{r}) - \mathbb{E})}{\hbar^2}$. This choice of k is possible as it simply reproduces the Schrödinger wave equation for the Hydrogen atom.

We choose the electric field amplitude to take the form of a plane wave equation propagating in the $\hat{z}$-direction, therefore

$$\mathrm{E}(\mathbf{r}) = A(\mathbf{r}) e^{ikz}. \tag{1.11}$$

There is a very useful approximation that can be applied to the Helmholtz equation, known as the paraxial approximation, which is related to the slow varying envelope approximation. Through this approximation, it is assumed that the complex amplitude of the electric field ($\Psi(x, y, z, t)$) varies slowly with respect to z. This allows one to neglect higher-order derivative terms of the

electric field, as the variation occurs slowly, hence $|\frac{\partial^2 A(\mathbf{r})}{\partial z^2}| << |2ik\frac{\partial}{\partial z}A(\mathbf{r})|$. Applying this approximation, and the plane wave equation, to Eq. (1.9) thus ultimately yields the paraxial wave equation (PWE) [6]:

$$\nabla^2 A(\mathbf{r}) + 2ik\frac{\partial}{\partial z}A(\mathbf{r}) = 0. \tag{1.12}$$

The paraxial wave equation can be solved in a number of ways. The solutions to this differential equation is given in terms of modes, with each mode representing a different energy eigenstate of the wave. The solutions to this differential equation in elliptical coordinates is given by Ince-Gaussian (IG) modes, in cylindrical coordinates the solutions are given by Laguerre-Gaussian (LG) modes, and in cartesian coordinates the solutions are Hermite-Gaussian (HG) modes. The choice of a cartesian coordinate system would yield spatial profiles with a cartesian symmetry and the same goes for choosing a cylindrical or elliptical coordinate system. The spatial profiles may look different, but since each coordinate system would yield an orthogonal set of solutions, one would be able to write the solutions in one coordinate system as the superposition of the solutions in another coordinate system. For instance one can take the superposition of LG modes and create an HG mode [7].

1.1.3 Spatial modes of light

As discussed in the previous subsection, there are several solutions to the paraxial wave Eq. (1.12). The LG and HG modes will be the two modes that are addressed. The first set of solutions presented are the Hermite-Gaussian modes (HG_m^n), a complete set of solutions to the paraxial wave equation that is mathematically determined as follows [8]:

$$\begin{aligned} HG_m^n(x,y,z) = A_{m,n}\frac{\omega_0}{\omega(z)}H_n\left(\frac{\sqrt{2}x}{\omega(z)}\right)H_m\left(\frac{\sqrt{2}y}{\omega(z)}\right)\exp\left[i(n+m+1)\text{Arctan}\left(\frac{z}{z_R}\right)\right] \\ \times\exp\left[-\frac{ik\rho^2}{2R(z)}\right]\exp[-ikz], \end{aligned} \tag{1.13}$$

with:

$$\begin{aligned} \rho &= \sqrt{x^2+y^2}, \\ \omega(z) &= \omega_0\sqrt{1+\left(\frac{z}{z_R}\right)^2}, \\ R(z) &= z\left[1+\left(\frac{z_R}{z}\right)^2\right], \\ z_R &= \frac{\pi\omega_0^2}{\lambda}. \end{aligned} \tag{1.14}$$

In these equations x, y, and z are the cartesian coordinates of the system, n and m are positive integers, $A_{m,n}$ is a constant, λ is the wavelength, and $R(z)$ is the radius of curvature of Eq. (1.13)

which is a variable required since this equation represents a paraboloidal wave. Furthermore, ω_0 is the beam waist where the radius of the beam profile is at its minimum, $\omega(z)$ is the radius of the beam at any other z position, z_R is the Rayleigh Range, a constant representing the distance for which the beam remains well collimated, and $H_n(x)$ are the orthogonal Hermite polynomials [9].

Two spatial properties of light that can be extracted from these Hermite-Gaussian modes, are the phase and intensity components. The intensity can be determined by computing the product of the field amplitude, with its conjugate,

$$I = |HG_m^n|^2 = [HG_m^n][HG_m^n]^*, \tag{1.15}$$

whereas the phase is calculated by taking the argument of the mode,

$$\phi = \text{Arg}[HG_m^n]. \tag{1.16}$$

Through plotting the intensity and phase profiles of these HG modes, one can visualize the properties. They are shown in **Figure** 1.1.

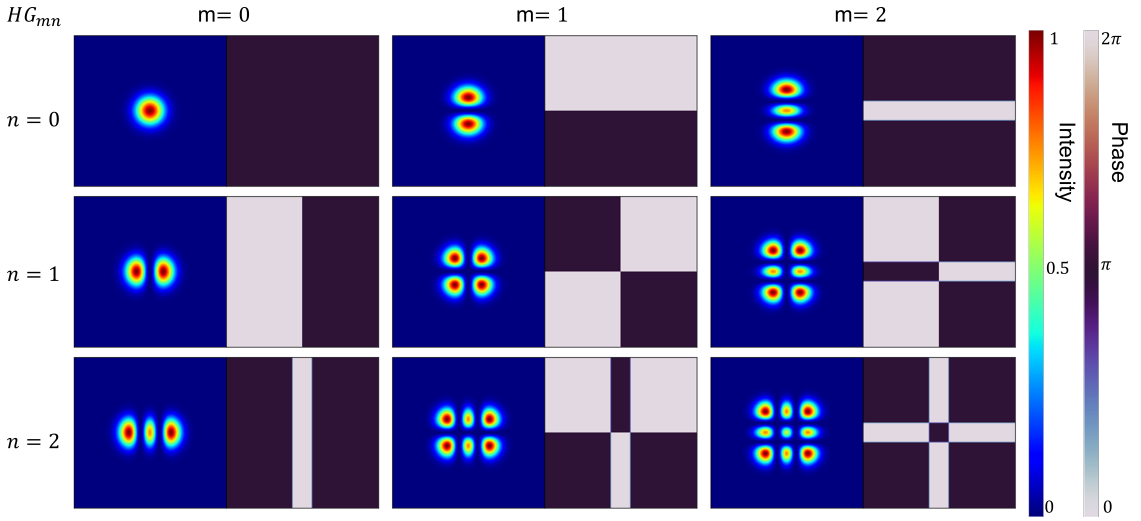


Figure 1.1: Hermite-Gaussian modes: These are the intensity profiles (left) and phase profiles (right) of the Hermite-Gaussian modes. They are respectively determined by the equations from before, (1.15) and (1.16). A trend can be seen where the n index dictates the amount of dark nodes in the horizontal direction and m the amount of dark nodes in the vertical direction [10].

The next set of solutions discussed are the Laguerre-Gaussian modes (LG_ℓ^p) [8], which are also a complete set of solutions for the paraxial wave equation (in cylindrical coordinates). The mathematical description is given by:

$$LG_{\ell}^{p}(\rho,\phi,z) = A_{\ell,p}\frac{\omega_0}{\omega(z)}\left(\frac{\rho}{\omega(z)}\right)^{|\ell|} L_{|\ell|}^{p}\left[2\left(\frac{\rho}{\omega(z)}\right)^2\right]\exp\left[i(2p+|\ell|+1)\text{Arctan}\left(\frac{z}{z_R}\right)\right] \times \exp\left[-\left(\frac{\rho}{\omega(z)}\right)^2\right]\exp\left[\frac{-ik\rho^2}{2R(z)}\right]\exp[-i\ell\phi]\exp[-ikz]. \tag{1.17}$$

In this equation L_{ℓ}^{p} are the Laguerre polynomials [9] with $A_{\ell,p}$ a constant, $p \geq 0$ as the radial index, and ℓ which is an integer azimuthal index expressing how many helical wave fronts are intertwined. The $\phi = \text{Arctan}(\frac{y}{x})$ is the azimuthal angle, and all other parameters are as stated before for the case of the Hermite-Gaussian modes.

Photons carry a linear momentum (**P**). This can clearly be seen when considering a plane wave with angular frequency ω and wave vector **k**. The linear momentum of this plane light wave is known to be $\hbar\mathbf{k}$ per photon [11]. Light, however, can also carry an angular momentum, $\mathbf{L} = \mathbf{r} \times \mathbf{P}$. This angular momentum can get further broken down into a spin angular momentum (analogous to the Earth's spin about its own axis) which depends on the polarisation of the light, and an orbital angular momentum (analogous to the Earth's orbit around the sun) which is present in wave fronts of helical (wave front twists about the axis of propagation) nature [12].

The $\exp(-i\ell\phi)$ term in Eq. (1.17) arises due to the twisting nature of the helical wave fronts of LG modes. **Note:** On the axis of propagation, the light waves effectively cancel each other resulting in a null intensity centre, this is called a phase singularity or an optical vortex. This vortex is given an integer number known as the topological quantum number (or topological charge ℓ) describing the amount of windings about this singularity [13]. The value of the topological charge provides an indication as to how the twisting topology of the wavefront changes. A higher value of the topological charge means more twists of the wavefront about the optical vortex.

The phase dependence of $\exp(-i\ell\phi)$ is seemingly familiar from quantum mechanical wave theory, a wave function with such a phase dependence is an eigenstate of the orbital angular momentum operator,

$$\hat{L_z} = -i\hbar\frac{\partial}{\partial\phi}, \tag{1.18}$$

with an eigenvalue of $\ell\hbar$ per photon. Photons can therefore carry an orbital angular momentum of $\ell\hbar$, dependent on the topological charge ℓ.

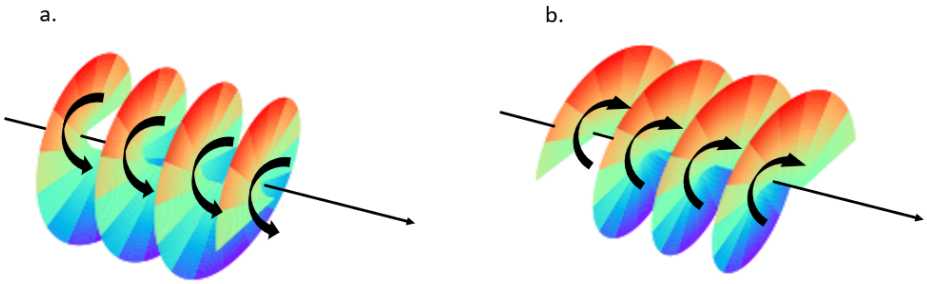


Figure 1.2: Twisting OAM wavefront: This shows what is meant by the twisting of light. The wavefront forms a helix about the direction of propagation. It can easily be noticed that for $\ell = 1$ (*a.*), the helix spirals clockwise and for $\ell = -1$ (*b.*) the helix spirals anti-clockwise.

Following an approach parallel to analysing the Hermite-Gaussian equation, the amplitude intensity and phase for the LG modes may also be computed as,

$$I = |LG_\ell^p|^2 = [LG_\ell^p][LG_\ell^p]^*, \tag{1.19}$$

and

$$\phi = \text{Arg}[LG_\ell^p]. \tag{1.20}$$

The intensity and phase profiles for the LG modes are shown in **Figure** 1.3.

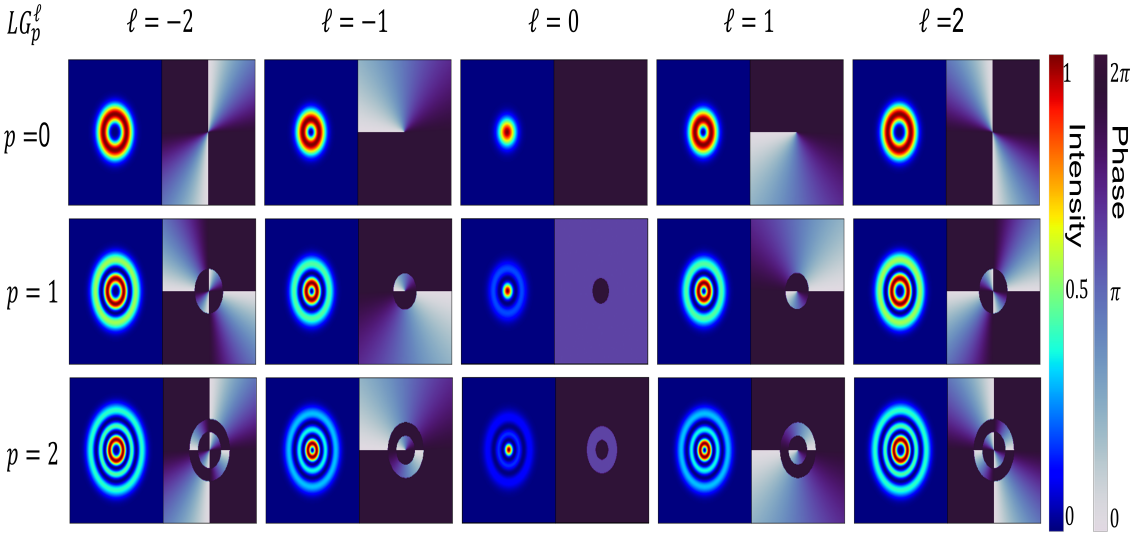


Figure 1.3: Laguerre-Gaussian modes: The left side in each image represents the intensity profile of the *LG* beam, while the right side represents the phase profile. It is clearly noticeable that the intensity profile is the same for ℓ values of opposite sign, but the phase profiles are not. The optical vortex also becomes larger for a higher topological charge ℓ, and when we increase the radial index p, rings are added around the initial doughnut structure.

1.2 The wave vector and some simple mathematical quantities

In quantum mechanics we work with wave vectors represented using the Dirac notation [3]. The notation introduces two new representations for vectors, called a bra and a ket. Consider the wave function of the state, which is usually represented as $\Psi(\mathbf{r}, t)$. In the Dirac notation it is denoted, in vectorial form as $|\Psi\rangle = \sum_m a_m |v_m\rangle$ which is called a ket and is usually associated with an infinite-dimensional column vector known as the state vector. $\langle\Psi|$ is known as a bra and is the complex conjugate transpose (dagger †) of the ket [14]. Though the ket is indeed a vector, the bra is a linear function of vectors in the sense that when this bra operates on the ket, it returns a complex number [3]. This operation is known as the inner product and will be discussed later in this section [3]. Of course, the wave function can also be in a finite dimensional space, which will be put to use for the sake of explanation. Consider the following illustration:

Let the wave function be represented as a 3-dimensional vector for the purpose of this illustration. It is represented as:

$$|\Psi\rangle = \begin{pmatrix} a \\ ib \\ ic \end{pmatrix}, \tag{1.21}$$

where a, b, and c represent any complex-valued numbers and i, is the imaginary representation of $\sqrt{-1}$.

Given (1.21) as the ket, the corresponding bra is given by

$$\langle\Psi| = (a^*, -ib^*, -ic^*). \tag{1.22}$$

There are two important quantities commonly used in quantum mechanics. The inner and outer product.

The inner product is defined to be the sum of the norm of the wave-vector squared

$$\langle\Psi|\Psi\rangle = \sum_m \sum_{m'} a_m a^*_{m'} \langle v_{m'}|v_m\rangle. \tag{1.23}$$

If instead the wave function was defined on a continuous space with $v_m(\mathbf{r}) = \langle\mathbf{r}|v_m\rangle$, then the inner product becomes an integral of the norm of the wave-vector squared,

$$\langle\Psi|\Psi\rangle = \sum_m \sum_{m'} a_m a^*_{m'} \langle v_{m'}|v_m\rangle, \tag{1.24}$$

where

$$\langle v_{m'}|v_m\rangle = \int v_m v^*_{m'} d^3\mathbf{r}. \tag{1.25}$$

The outer product of a wave function, again defined on a finite-dimensional space, is defined to be

$$|\Psi\rangle\langle\Psi| = \sum_m \sum_{m'} a_m a^*_{m'} |v_m\rangle\langle v_{m'}|, \tag{1.26}$$

which is now the multiplication of a column vector on the left with a row vector on the right.

To see how these work:

Let

$$|v_1\rangle = \begin{pmatrix} a_1 \\ b_1 \\ c_1 \end{pmatrix}, \tag{1.27}$$

and

$$\langle v_1| = (a_1^*, b_1^*, c_1^*), \tag{1.28}$$

then

$$\langle v_1|v_1\rangle = a_1 a_1^* + b_1 b_1^* + c_1 c_1^*, \tag{1.29}$$

and

$$|v_1\rangle\langle v_1| = \begin{pmatrix} a_1 a_1^* & a_1 b_1^* & a_1 c_1^* \\ b_1 a_1^* & b_1 b_1^* & b_1 c_1^* \\ c_1 a_1^* & c_1 b_1^* & c_1 c_1^*. \end{pmatrix}. \tag{1.30}$$

1.3 The Hilbert Space

A vector space over a scalar field S is a space containing a set of vectors, which should satisfy closure under vector addition and scalar multiplication. By closure, it is implied that the result of the vector addition or scalar multiplication is still a member belonging to the initial vector space. Take vectors **a** and **b**, contained in some vector space V, the inner product of **a** and **b** is not defined in V. We define a new space V_1 as an inner product space, which includes the vector space V and the inner product operation. Finally, if this inner product space is complete, then it is a Hilbert space [15].

Definition 1: Hilbert Space

A Hilbert Space is a vector space consisting of a set of vectors describing the wave function of a state in quantum mechanics. The Hilbert space should satisfy the following properties:

- The result of vector addition should be contained in this space,

- Any vector multiplied by any scalar, should also be contained in this space,
- The norm of these vectors should be contained in this space, as well as the inner product of these vectors.

In quantum mechanics, a composite state (describing the state of a composite system) is defined in a particular composite space. The Hilbert space in which this composite state is contained must be constructed from the spaces in which the sub-systems are contained. To clarify, let the state $|\Psi_A\rangle$ of a system A be defined in a Hilbert space $\mathcal{H}_A$, and let the state $|\Psi_B\rangle$ of a system B be defined in Hilbert space $\mathcal{H}_B$. The composite state, as defined by a product state, is contained in the composite Hilbert space. See the following illustration:

If $|\Psi_A\rangle \in \mathcal{H}_\mathcal{A}$ and $|\Psi_B\rangle \in \mathcal{H}_\mathcal{B}$ then $|\Psi_{AB}\rangle = |\Psi_A\rangle \otimes |\Psi_B\rangle \in \mathcal{H}_{\mathcal{AB}}$ (this is a product state) where $\mathcal{H}_{\mathcal{AB}} = \mathcal{H}_\mathcal{A} \otimes \mathcal{H}_\mathcal{B}$ and the symbol $\otimes$ represents a tensor product.

1.4 Polarization

The discovery of polarization precedes the discovery of the orbital angular momentum degree of freedom. The quantum polarization state vector is a qubit state identical to the classical Jones matrices from classical polarization. Polarization was therefore chosen as the natural choice for the qubit state used in understanding many quantum phenomena in the pioneering days of quantum mechanics. Seeing that polarization has historical significance as a natural choice for a qubit, it makes sense to briefly review the polarization of light. Polarization refers to the plane of oscillation of the electric and magnetic fields of an electromagnetic wave. These electric and magnetic fields oscillate perpendicular to one another, and to the direction of propagation of light (see **Figure** 1.4). The electric field for LG and HG modes introduced earlier, were shown as a scalar quantity, but since these fields represent waves that oscillate, we are required to stipulate the direction in which these oscillations occur. When referring to polarization, one usually only refers to the plane in which the electric fields oscillate [16]. Assume that the electric field can be broken down into two components E_x and E_y. If the electric field oscillation occurs only in the $\hat{x}$, or $\hat{y}$ direction (propagation is in the $\hat{z}$ direction), then it is said that the polarization is horizontal linear, or vertical linear, respectively.

The two components of the electric field can also be super-positioned through $E_x\hat{x} + e^{i\phi}E_y\hat{y}$. When the phase shift is $\phi = \frac{\pi}{4}$, the polarization that occurs is known as diagonal linear polarization, and when $\phi = \frac{-\pi}{4}$, it is known as anti-diagonal linear polarization. Depending on the phase shift ϕ between vertical and horizontal polarization, one can find many different types of polarization that could occur. The Jones vectors for these polarizations can be seen as the state vectors. They are given in Eq. (1.31) [17]:

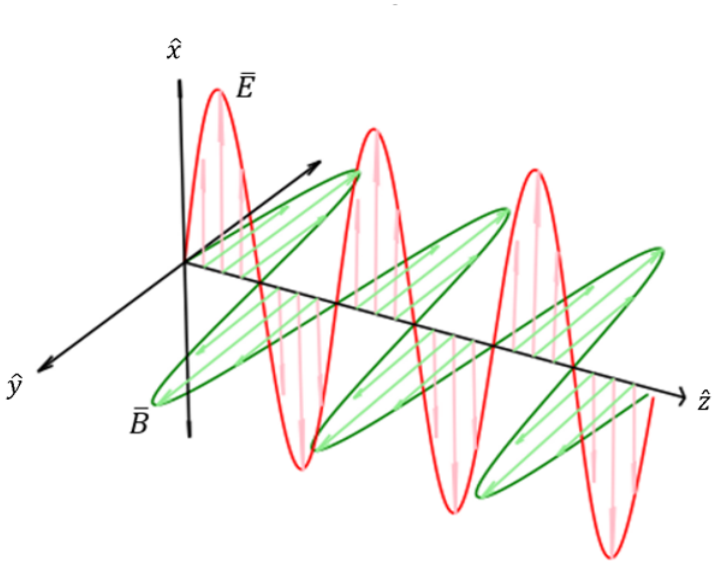


Figure 1.4: Electric and magnetic field oscillation: The electric ($\bar{E}$) and magnetic fields ($\bar{B}$) oscillate perpendicular to one another, and the direction of propagation ($\hat{z}$).

$$
\begin{aligned}
&\text{Vertical Polarization vector:} && |V\rangle = \begin{pmatrix} 0 \\ E_y \end{pmatrix}, \\
&\text{Horizontal Polarization vector:} && |H\rangle = \begin{pmatrix} E_x \\ 0 \end{pmatrix}, \\
&\text{Diagonal Polarization vector:} && |D\rangle = \frac{1}{\sqrt{2}}(|H\rangle + |V\rangle) = \frac{1}{\sqrt{2}}\begin{pmatrix} E_x \\ E_y \end{pmatrix}, \\
&\text{Anti-diagonal Polarization vector:} && |A\rangle = \frac{1}{\sqrt{2}}(|H\rangle - |V\rangle) = \frac{1}{\sqrt{2}}\begin{pmatrix} E_x \\ -E_y \end{pmatrix}, \\
&\text{Right-circular Polarization vector:} && |R\rangle = \frac{1}{\sqrt{2}}(|H\rangle - i|V\rangle) = \frac{1}{\sqrt{2}}\begin{pmatrix} E_x \\ iE_y \end{pmatrix}, \\
&\text{Left-circular Polarization vector:} && |L\rangle = \frac{1}{\sqrt{2}}(|H\rangle + i|V\rangle) = \frac{1}{\sqrt{2}}\begin{pmatrix} E_x \\ -iE_y \end{pmatrix}.
\end{aligned}
\tag{1.31}
$$

These polarization states can be neatly represented by a generalized equation that allows for the amplitude and phase shift between the two states to be adjusted. This generalized equation is given by,

$$|\psi\rangle = \cos(\theta/2)|R\rangle + e^{i\phi}\sin(\theta/2)|L\rangle, \tag{1.32}$$

where $|R\rangle$ and $|L\rangle$ are the basis states for Right and Left circular polarization respectively. This generalized equation (Eq. (1.32)) parameterizes the polarization states as a unit sphere depending

on θ and ϕ. This sphere is known as the Poincaré sphere [18]. Each polarization state vector corresponds to a specific point found on the surface of this unit sphere, see **Figure** 1.5

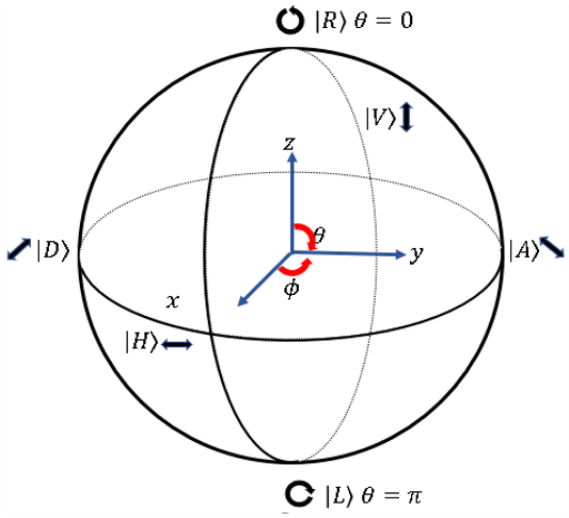


Figure 1.5: Poincaré sphere: By setting $\theta = 0$ with $\phi = 0$, and examining the sphere, the state corresponding to right circular polarization is realized. This logic can be repeated for all other states by simply searching for the desired polarization state on the surface of the sphere, and reading off the respective corresponding θ and ϕ values.

1.5 Mixed and Pure States

The definition of mixed and pure states is introduced here as it is incredibly important for defining quantum states in the sections to come. When the state of a system is known exactly ($|\psi\rangle$ is known), the quantum system being observed is said to be in a pure state. A density matrix for a pure state can be defined and is simply represented as the projector,

$$\rho = |\psi\rangle\langle\psi|. \tag{1.33}$$

This is also known as the density matrix for a pure state. There is only one exactly known state describing the system so there is no summation, and since this state is exactly known, the probability of measuring an observable of this state is 1.

If the system cannot be represented as a pure state then it is a mixed state. The understanding of mixed states is therefore an extension of the interpretation used above. A system is not necessarily described by only one exact state, it can be statistically defined by a set of pure states, resulting in a mixed state.

Consider an ensemble (set) of pure states represented by $\{|\psi_i\rangle, p_i\}$ where $i = 1, \ldots, N$. Each p_i is the probability corresponding to each state $|\psi_i\rangle$. These states are not required to satisfy orthogonality. The system cannot be defined to be in only one of these particular states, instead, the system is described as a complete state by taking the superposition (not to be confused with the usual quantum mechanical superposition of states) of the states in the ensemble, each multiplied

by the corresponding probability. This mixed state can therefore be represented by considering what is called, a pure state decomposition. Effectively, the task here is to represent the mixed state, in terms of all the pure states, as well as the corresponding probability in that ensemble $\{|\psi_i\rangle, p_i\}$, that make up the mixed state. This pure state decomposition gives the density matrix for a mixed state [19]:

$$\rho = \sum_i p_i |\psi_i\rangle \langle \psi_i|. \tag{1.34}$$

It should be mentioned that this is not the only pure state decomposition of the mixed state. There are multiple pure state decompositions in the ensemble $\{|\psi_l'\rangle, p_j'\}$ that gives rise to the exact same state ρ. Therefore, all pure state decompositions for this mixed state ρ is given by [20, 21]:

$$\rho = \sum_j p_j' |\psi_j'\rangle \langle \psi_j'|. \tag{1.35}$$

When one diagonalizes a matrix, one can obtain the eigenvalues on the diagonal elements of the matrix. Since this is true, the sum of the eigenvalues is the same as the trace of the matrix defining the state. A similar idea is used here. By multiplying the density matrix, and the observable, a new matrix is determined ρQ representing the probabilities of the observable corresponding to the pure states. Since the sum of the eigenvalues gives the expectation value, the same result is determined by taking the trace of this matrix ρQ. The expectation value of the observable is represented as $\langle Q \rangle$, and is defined by [22]

$$\langle Q \rangle = Tr(\rho Q). \tag{1.36}$$

There are a few tests that may assist in determining whether the density matrix represents a mixed or a pure state. A useful and well known example of such a test stands as follows:

If $\rho = \rho^2$ then ρ represents a pure state, otherwise it is a mixed state.

An equivalent statement for this would be:

For a pure state, $Tr(\rho^2) = 1$ and for a mixed state, $Tr(\rho^2) < 1$. This expression $Tr(\rho^2)$ is usually denoted as P and is usually titled as the purity of a state [23].

1.6 Density Matrix

A density matrix, or more correctly a density operator, is an operator that provides a way of describing a system's state that is not completely and exactly known. Suppose that a system, defined in a finite-dimensional space, can be in one of the states $|\psi_i\rangle$, where i is an index, and each state has associated with it a respective probability p_i assigned to the state ψ_i in the mixed state. The set $\{|\psi_i\rangle, p_i\}$ is known as an ensemble of states, for which the density matrix (operator) for this ensemble is determined by means of an outer product (1.26) [3, 20]:

$$\rho = \sum_m p_m |\psi_m\rangle\langle\psi_m|. \tag{1.37}$$

Some properties of this density matrix include [24]:

- The Trace (sum of diagonals) of $\rho = 1$; $Tr(\rho) = 1$, and
- the density matrix is Hermitian, $\rho = \rho^\dagger$.

By the first property, the trace of the diagonals of this density matrix must be equal to one, such that [20]:

$1 = Tr(\rho) = \sum_m p_m Tr(|\psi_m\rangle\langle\psi_m|) = \sum_m p_m \sum_m (|\psi_m\rangle\langle\psi_m|) = \sum_m p_m,$

and hence

$$\sum_m p_m = 1, \tag{1.38}$$

which ensures normalization among the states. The sum of these probabilities equals unity.

An example will be presented to demonstrate how the density matrix is generally applied for quantum systems.

Example 1

Consider a system of two photons (bipartite system). Each photon is in a normalized superposition state of two OAM states with opposing sign. These OAM states considered have the radial indices set to 0, so we only need to refer to the azimuthal indices. These photons are described by the same state, $|\psi_1\rangle = \frac{1}{\sqrt{2}}(|-\ell\rangle + |\ell\rangle)$ and $|\psi_2\rangle = \frac{1}{\sqrt{2}}(|-\ell\rangle + |\ell\rangle)$. Here the basis state

$$|-\ell\rangle = \begin{pmatrix} 0 \\ 1 \end{pmatrix}, \tag{1.39}$$

represents the negative OAM basis state and

$$|\ell\rangle = \begin{pmatrix} 1 \\ 0 \end{pmatrix}, \tag{1.40}$$

represents the positive OAM basis state.

The composite state of the two-qubit system is

$$|\psi_{comp}\rangle = |\psi_1\rangle \otimes |\psi_2\rangle = \frac{|-\ell,-\ell\rangle + |-\ell,\ell\rangle + |\ell,-\ell\rangle + |\ell,\ell\rangle}{2}, \tag{1.41}$$

which is determined by the tensor product of $|\psi_1\rangle$ and $|\psi_2\rangle$. Here the first index in each ket represents the first particle, and the second index is for the second particle. There are four corresponding basis states:

- $|\psi_{-\ell,\ell}\rangle = |-\ell,\ell\rangle$ where photon 1 has negative OAM and photon 2 has positive OAM,
- $|\psi_{\ell,-\ell}\rangle = |\ell,-\ell\rangle$ where photon 1 has positive OAM and photon 2 has negative OAM,
- $|\psi_{\ell,\ell}\rangle = |\ell,\ell\rangle$ where both photons have positive OAM, and
- $|\psi_{-\ell,-\ell}\rangle = |-\ell,-\ell\rangle$ where both photons have negative OAM.

Each basis state has a corresponding probability of $|\frac{1}{2}|^2 = \frac{1}{4}$.

Utilizing (1.37), $\rho = p_{comp}|\psi_{comp}\rangle\langle\psi_{comp}|$ where $p_{comp} = 1$. Explicitly expanding this projector yields the following:

$$\rho = p_1|\psi_{-\ell,-\ell}\rangle\langle\psi_{-\ell,-\ell}| + p_2|\psi_{-\ell,-\ell}\rangle\langle\psi_{-\ell,\ell}| + p_3|\psi_{-\ell,-\ell}\rangle\langle\psi_{\ell,-\ell}| + p_4|\psi_{-\ell,-\ell}\rangle\langle\psi_{\ell,\ell}| + p_5|\psi_{-\ell,\ell}\rangle\langle\psi_{-\ell,-\ell}| + p_6|\psi_{-\ell,\ell}\rangle\langle\psi_{-\ell,\ell}| + p_7|\psi_{-\ell,\ell}\rangle\langle\psi_{\ell,-\ell}| + p_8|\psi_{-\ell,\ell}\rangle\langle\psi_{\ell,\ell}| + p_9|\psi_{\ell,-\ell}\rangle\langle\psi_{-\ell,-\ell}| + p_{10}|\psi_{\ell,-\ell}\rangle\langle\psi_{-\ell,\ell}| + p_{11}|\psi_{\ell,-\ell}\rangle\langle\psi_{\ell,-\ell}| + p_{12}|\psi_{\ell,-\ell}\rangle\langle\psi_{\ell,\ell}| + p_{13}|\psi_{\ell,\ell}\rangle\langle\psi_{-\ell,-\ell}| + p_{14}|\psi_{\ell,\ell}\rangle\langle\psi_{-\ell,\ell}| + p_{15}|\psi_{\ell,\ell}\rangle\langle\psi_{\ell,-\ell}| + p_{16}|\psi_{\ell,\ell}\rangle\langle\psi_{\ell,\ell}|.$$

Each of these coefficients $(p_1, \ldots, p_{16})$ represent an element on the density matrix. It is determined by taking into consideration the coefficient of each of the basis states. The coefficient of the basis ket is multiplied with the complex conjugate coefficient of the basis bra. In this particular case, the coefficients are real and equal. Take a look for instance at the first term of ρ:

$p_1|\psi_{-\ell,-\ell}\rangle\langle\psi_{-\ell,-\ell}| = (\frac{1}{2})(\frac{1}{2})|\psi_{-\ell,-\ell}\rangle\langle\psi_{-\ell,-\ell}| = \frac{1}{4}|\psi_{-\ell,-\ell}\rangle\langle\psi_{-\ell,-\ell}|$ such that $p_1 = \frac{1}{4}$.

This will be the case for all of the coefficients p_i as the coefficients of each of the basis states is exactly the same, therefore $p_1 = p_2 = \ldots = p_{15} = p_{16} = \frac{1}{4}$

The density matrix is thus given by:

$$\rho = \begin{pmatrix} \frac{1}{4} & \frac{1}{4} & \frac{1}{4} & \frac{1}{4} \\ \frac{1}{4} & \frac{1}{4} & \frac{1}{4} & \frac{1}{4} \\ \frac{1}{4} & \frac{1}{4} & \frac{1}{4} & \frac{1}{4} \\ \frac{1}{4} & \frac{1}{4} & \frac{1}{4} & \frac{1}{4} \end{pmatrix}. \tag{1.42}$$

For verification purposes, notice that $Tr(\rho) = \frac{1}{4} + \frac{1}{4} + \frac{1}{4} + \frac{1}{4} = 1$, which indeed is a property of the density matrix.

The use of the probability density matrix becomes apparent when considering instances such as the one discussed above. Each element on the matrix essentially represents the probability of an observable of one of these combined states to be observed. The classification of the probability density is not restricted to multi-particle (multipartite) systems, as it can characterize the state of a single particle system as well.

It will soon be seen that the density matrix can be used to describe the sub-states of an entangled state, which would not be possible by means of a single wave function [25].

1.7 Reduced Density Matrix

In many instances, a case may arise where only a composite system, comprised of sub-systems A and B, is given, but there is a requirement that state A needs to be determined. To do this, one makes use of what is called the partial trace of the density matrix.

The partial trace is an operation mapping the density matrix ρ_{AB}, defined on a composite Hilbert space $\mathcal{H}_{\mathcal{AB}}$, onto a density matrix ρ_A defined on the Hilbert space $\mathcal{H}_{\mathcal{A}}$. The operation works as follows [20]:

$$Tr(|b_h\rangle\langle b_i|) = Tr(\langle b_i|b_h\rangle) = \langle b_i|b_h\rangle. \tag{1.43}$$

The above follows due to the property of traces such that $Tr(AB) = Tr(BA)$ where A and B are both $n \times n$ matrices [26, 27].

Let $\{|a_i\rangle\}$ be the set of basis states for $\mathcal{H}_A$ and let $\{|b_i\rangle\}$ be the set of basis states for $\mathcal{H}_B$. Denote then, any composite system density matrix as ρ_{AB} defined on $\mathcal{H}_{AB} = \mathcal{H}_A \otimes \mathcal{H}_B$. In this representation:

$$\rho_{AB} = \sum_{fghi} |a_f\rangle\langle a_g| \otimes |b_h\rangle\langle b_i|. \tag{1.44}$$

Now, by taking the partial trace of the density matrix ρ_{AB}, the state of system B is effectively traced out of the composite system density matrix. The result is the reduced/marginal density matrix, ρ_A, representing the state of only system A:

$$\rho_A = Tr_B(\rho_{AB}) = \sum_{fghi} |a_f\rangle\langle a_g|\langle b_i|b_h\rangle. \tag{1.45}$$

An example is provided to ensure clarity regarding the concept of using the partial trace to determine the reduced/marginal density matrix [20]

Example 2

Consider an orthonormal qubit triplet state defined by

$|\psi\rangle = \frac{1}{\sqrt{2}}(|-\ell,\ell\rangle + |\ell,-\ell\rangle)$,

$|\psi\rangle\langle\psi| = \frac{1}{2}(|-\ell,\ell\rangle\langle-\ell,\ell| + |\ell,-\ell\rangle\langle\ell,-\ell| + |\ell,-\ell\rangle\langle-\ell,\ell| + |-\ell,\ell\rangle\langle\ell,-\ell|)$.

By making use of Eqs. (1.44) and (1.45), where $|\psi\rangle\langle\psi|$ plays the role of ρ_{AB} in (1.44), the equation to find ρ_A (reduced density matrix) by using (1.45) is done in the following manner (keep in mind that the states here are orthonormal):

$$\begin{aligned} Tr_B(|\psi\rangle\langle\psi|) &= \tfrac{1}{2}(|-\ell\rangle\langle-\ell|\langle\ell|\ell\rangle + |\ell\rangle\langle\ell|\langle-\ell|-\ell\rangle + |\ell\rangle\langle-\ell|\langle-\ell|\ell\rangle + |-\ell\rangle\langle\ell|\langle\ell|-\ell\rangle) \\ &= \tfrac{1}{2}(|-\ell\rangle\langle-\ell|\langle\ell|\ell\rangle + |\ell\rangle\langle\ell|\langle-\ell|-\ell\rangle + 0 + 0) \\ &= \tfrac{1}{2}(|-\ell\rangle\langle-\ell| + |\ell\rangle\langle\ell|) \\ &= \tfrac{1}{2}I. \end{aligned}$$

In this case, the reduced density matrix ρ_A is $\frac{1}{2}I$, where I is the Identity matrix.

1.8 Concept of factorability and quantum entanglement

When a state of a system, can be represented as a product of two states, it is known to be a factorable state: Consider a bipartite (two particle) system with one particle in state $|\psi\rangle_A$ and another particle in state $|\psi\rangle_B$.

The state of this bipartite system is written as

$$|\psi\rangle = |\psi\rangle_A \otimes |\psi\rangle_B, \tag{1.46}$$

and is known as a factorable, or a separable, state.

The concept of factorability is the key to understanding entanglement, although it should be made clear that entanglement is not restricted to only a two-particle system, one can have entanglement between properties of multiple particles, and even entanglement between two properties of a single particle [28].

Consider for the time being a bipartite system, as described in **Example 1**. Photon 1 is found to be in state $|\psi_1\rangle$, which is mathematically defined to be contained in the domain of the Hilbert space $\mathcal{H}_1$, and for photon 2, the state is $|\psi_2\rangle$ which is defined in the domain of $\mathcal{H}_2$. The composite state is given by $|\psi_{sep}\rangle = |\psi_1\rangle \otimes |\psi_2\rangle$, where $|\psi_{sep}\rangle$ is an element of the composite domain $\mathcal{H}_{12} = \mathcal{H}_1 \otimes \mathcal{H}_2$.

If the $|\psi_{sep}\rangle$ can be represented as a direct product of two states, then it is considered to be a non-entangled, or synonymously separable, state. If the state cannot be represented in this factorized way, then it is an entangled, or non-separable, state. An example should suffice to make this more visually descriptive.

Example 3

In this example, two photons whose states are defined in the Laguerre-Gaussian LG_p^ℓ basis are used. We set $p = 0$ for both photons. Let us assume that each photon can be in a superposition state with azimuthal indices (also referred to as the topological charge), ℓ_1 and ℓ_2. We will therefore represent the possible states that each photon can be in, in a simplistic fashion, again given by $|\ell_1\rangle$ and $|\ell_2\rangle$. The states of the two photons can then be represented as:

$|\psi_A\rangle := a|\ell_1\rangle + b|\ell_2\rangle$,

for photon 1 with $a^2 + b^2 = 1$ since a and b are the complex coefficients for the respective sub-states of particle 1, and

$|\psi_B\rangle := c|\ell_1\rangle + d|\ell_2\rangle$,

for photon 2 with $c^2 + d^2 = 1$ again since c and d are the respective complex coefficients factors for the sub-states for particle 2.

$|\psi_{sep}\rangle = |\psi_A\rangle \otimes |\psi_B\rangle$ is the factorized, non-entangled state, this is also known as a separable state. This can be expanded in the usual way as follows:

$$|\psi_{sep}\rangle = (a|\ell_1\rangle + b|\ell_2\rangle) \otimes (c|\ell_1\rangle + d|\ell_2\rangle)$$
$$= ac|\ell_1\rangle|\ell_1\rangle + ad|\ell_1\rangle|\ell_2\rangle + bc|\ell_2\rangle|\ell_1\rangle + bd|\ell_2\rangle|\ell_2\rangle.$$

Where the first ket represents the state for particle one and the second ket for particle two. Relabel the probabilities as real-valued numbers with $a' = ac$, $b' = ad$, $c' = bc$ and $d' = bd$, where the usual property holds, $a'^2 + b'^2 + c'^2 + d'^2 = 1$. The sub-states can also be represented in a simplified manner for instance by representing $|\ell_1\rangle|\ell_2\rangle$ as $|\ell_1\ell_2\rangle$. This notation will be used throughout the thesis. The separable state can then be simplified to:

$|\psi_{sep}\rangle = a'|\ell_1\ell_1\rangle + b'|\ell_1\ell_2\rangle + c'|\ell_2\ell_1\rangle + d'|\ell_2\ell_2\rangle$.

Any state that is a linear combination of $|\ell_1\ell_1\rangle$, $|\ell_1\ell_2\rangle$, $|\ell_2\ell_1\rangle$ and $|\ell_2\ell_2\rangle$, such that it can be represented in this way, is a non-entangled state. If it cannot be written in this given form, and cannot be factorized, it is not a separable state and is considered to be **entangled**.

The following three states are examples of non-separable (NS) entangled states, as neither of them can be factorized in the required way.

- $|\psi_{NS}\rangle = a'|\ell_1\ell_1\rangle + b'|\ell_2\ell_2\rangle$ with $a'^2 + b'^2 = 1$
- $|\psi_{NS}\rangle = a'|\ell_1\ell_2\rangle + b'|\ell_2\ell_1\rangle$ with $a'^2 + b'^2 = 1$
- $|\psi_{NS}\rangle = a'|\ell_1\ell_1\rangle + b'|\ell_1\ell_2\rangle + c'|\ell_2\ell_1\rangle$ with $a'^2 + b'^2 + c'^2 = 1$

It is important to recognise that entanglement can occur between two properties of the same particle and that this reasoning can be extended to more than a two-particle system. If these multipartite states cannot be represented as a direct product of each particle's state, then it is entangled. Likewise, if a single particle's state cannot be represented as a direct product of the states describing the properties of the particle, then these properties are also entangled with one another, this is identified as self-entanglement.

1.9 Measures of Entanglement - Entropy

One often has to extract the relevant information present in a system. To ensure that the concept is fully understood, the reader is first introduced to classical information theory. These concepts are then mapped over to quantum information theory where a description of Von-Neumann entropy is presented. These entropy measures lay a foundation for determining the measure of entanglement present in a quantum system.

1.9.1 Shannon Entropy

In classical information theory, a key measure is used when determining the amount of information present in a system, it is called the Shannon entropy. This measure essentially quantifies how much information about a variable is gained *after* determining the value of this variable. An alternative view to this entropy is that it represents the **uncertainty** of the information of the variable, *before* measuring the value of this variable. In an ensemble system of these variables, with each variable having a probability p_x, the Shannon Entropy is mathematically defined to be [20]

$$H(p) = -\sum_x p_x \log(p_x), \tag{1.47}$$

where x indicates each variable in this ensemble. Conventionally, a log of base 2 is employed for convenience, such that the unit of entropy becomes the bit [26]. When $p_x = 0$, immediately the first thought is that this becomes an issue as $\log(0)$ is undefined. However logically, it should make intuitive sense that when an event cannot occur, it should not contribute to the measurement. It is thus defined that $0 \log(0) = 0$ by continuity [20].

1.9.2 Other classical information measures using Entropy

Making use of the Shannon entropy, several other measures of information relating two random variables, X and Y, can be defined. They are mentioned below [19, 20]:

- Relative Entropy, $H(X||Y)$, which is used to measure the similarity between these variables.
- Joint Entropy,

$$H(X,Y) = -\sum_{xy} p(x,y) \log(p(x,y)), \tag{1.48}$$

  which is a combined measurement of these 2 random variables. It is interpreted as a measure of the uncertainty (unknown information) about the (X,Y) pair.

- Conditional Entropy,

$$H(X|Y) = H(X,Y) - H(Y), \tag{1.49}$$

  which is a measure of the uncertainty of measuring X, with having the outcome of Y already determined.

- Mutual entropy,

$$H(X:Y) = H(X) + H(Y) - H(X,Y) = H(X) - H(X|Y), \tag{1.50}$$

  which is a measure indicating the amount of information that A and B have in common. This is an important measure indicating the correlation between the variables.

1.9.3 Von-Neumann Entropy

The definitions defined in the previous two subsections, 1.9.1, 1.9.2, have analogous definitions in quantum physics. The Von-Neumann entropy plays the role of Shannon Entropy in quantum mechanics. Mathematically, the Von-Neumann entropy is described by the following equation:

$$S(\rho) = -Tr(\rho \log(\rho)). \tag{1.51}$$

[20, 25].

Though one cannot directly determine the logarithm of a matrix, one can diagonalize the matrix to attain the eigenvalues (λ_k, these are non-negative) and use these eigenvalues instead. This is possible since the trace operation is invariant under unitary transformation (a unitary operator is any operator that obeys the relation $\hat{A}^\dagger = \hat{A}^{-1}$). The entropy is then determined as follows:

$$S(\rho) = -\sum_k \lambda_k \log(\lambda_k). \tag{1.52}$$

The entropy is also definite as there are no non-negative eigenvalues. Keep in consideration that there are instances where the eigenvalues are zero, but as mentioned in Section 1.9.1 this is no cause for alarm as $0 \log(0) = 0$.

This entropy can be seen as the quantity of information about the system that is unknown. To this extent, when the entropy is zero, then no information about the system is unknown, and the system is in a pure state. Consequently, when the entropy measurement is non-zero, then it indicates a mixed system [29].

Let us now assume that the dimension of the Hilbert space is n. If all the eigenvalues are equal, then each eigenvalue must be equal to $\frac{1}{n}$ to ensure that the sum of all the eigenvalues adds up to 1. By doing this, the normalization condition is maintained. When a situation such as this arises, it is said that the state is maximally mixed in this Hilbert space of dimension n and the entropy is thus one, which is the maximum value it can attain. The density matrix here then is equivalent to the identity matrix multiplied with the inverse of the size of the dimension (n in this case) [25]:

$$\rho = \frac{1}{n} I. \tag{1.53}$$

The importance of the Von-Neumann entropy is that for a discrete pure state $|\psi_{AB}\rangle$, the measure of entanglement is defined as the Von-Neumann entropy of either sub-system A or B [30]:

$$E(|\psi_{AB}\rangle) = -Tr(\rho_A \log(\rho_A)) = -Tr(\rho_B \log(\rho_B)), \tag{1.54}$$

where ρ_A and ρ_B are the reduced density matrices of the sub-systems [19]:

$$\rho_A = Tr_B(|\psi_{AB}\rangle\langle\psi_{AB}|), \tag{1.55}$$

$$\rho_B = Tr_A(|\psi_{AB}\rangle\langle\psi_{AB}|). \tag{1.56}$$

When the reduced density matrix is maximally mixed, it indicates that the global state (the state of the composite system between systems A and B) has maximal entanglement.

When one refers to maximal entanglement between two sub-systems, it is meant that these two sub-systems have to share the maximum amount of information between each other, or in other words, the maximal mutual entropy between the two sub-systems.

Since Von-Neumann entropy is the quantum analogue of the classical Shannon entropy, it would make sense that there is a quantum mutual entropy as well, it is given by [19]:

$$I(\rho_{AB}) = S(\rho_A) + S(\rho_B) - S(\rho_{AB}). \tag{1.57}$$

Since entanglement is essentially an indication of the information shared between two parties, if the two parties have maximal mutual entropy, then it should make sense that there is maximal entanglement between the two parties. This corresponds to when the Von-Neumann entropy is equal to its maximum value of 1.

Interestingly, the Von-Neumann entropy also possesses a property whereby it obeys a strong subadditivity inequality. In a bipartite system (with sub-systems A and B), this inequality is given by [20]:

$$S(\rho_{AB}) \leq S(\rho_A) + S(\rho_B), \tag{1.58}$$

and equivalently, for a tripartite system (with sub-systems A,B and C), this inequality is given by [20]:

$$S(\rho_{ABC}) + S(\rho_B) \leq S(\rho_{AB}) + S(\rho_{BC}). \tag{1.59}$$

1.9.4 Linear Entropy

There is another entropy measure for entangled states that is incredibly useful. It makes use of the purity P which was previously defined to be the trace of the square of the density matrix, $P = Tr(\rho^2)$. This entropy measure is represented as follows [21]:

$$S_{lin}(\rho) = 2(1 - Tr(\rho^2)). \tag{1.60}$$

Conveniently, since the square of the density matrix is utilized, there is no need to diagonalize ρ. This makes the computation of the linear entropy quite easy [19]. This measure presents the degree of mixedness of the density matrix. As for evaluating this measure for a pure bipartite entangled system $|\psi_{AB}\rangle$, comprised of sub-systems A and B, the entanglement is defined as the linear entropy of either sub-system A or B [19, 21]:

$$E(|\psi_{AB}\rangle) = 2(1 - Tr(\rho_A^2)) = 2(1 - Tr(\rho_B^2)), \tag{1.61}$$

where ρ_A and ρ_B are the reduced density matrices as described in Eqs. (1.55) and (1.56).

1.10 Measures of entanglement - Concurrence

1.10.1 Concurrence

Another measure of the degree of entanglement is a measure called the concurrence and is mathematically defined by [31, 32]:

$$C(\rho) = \max\{0, \lambda_1 - \lambda_2 - \lambda_3 - \lambda_4\}. \tag{1.62}$$

The approach is to make use of a density matrix that takes the form of [18]

$$\tilde{\rho} = (\gamma)\rho^*(\gamma), \tag{1.63}$$

where ρ^* is the complex conjugate of ρ in the basis above and γ is an anti-unitary operator that satisfies $\langle\psi|\gamma|\phi\rangle = \langle\phi|\gamma^{-1}|\psi\rangle$ for any states ϕ and ψ [18].

The $\lambda_i's$ above are the eigenvalues, in decreasing order, of the Hermitian matrix R given by

$$R = \sqrt{\sqrt{\rho}\tilde{\rho}\sqrt{\rho}}. \tag{1.64}$$

The concurrence also takes on values between 0 and 1 with 0 indicating no entanglement and 1 indicating the maximal entanglement.

Using **Example 1**:

$$\rho = \begin{pmatrix} \frac{1}{4} & \frac{1}{4} & \frac{1}{4} & \frac{1}{4} \\ \frac{1}{4} & \frac{1}{4} & \frac{1}{4} & \frac{1}{4} \\ \frac{1}{4} & \frac{1}{4} & \frac{1}{4} & \frac{1}{4} \\ \frac{1}{4} & \frac{1}{4} & \frac{1}{4} & \frac{1}{4} \end{pmatrix}. \tag{1.65}$$

The anti-unitary operator for a two qubit state is utilized, and is given by $\gamma = \sigma_y \otimes \sigma_y$ with σ_y as the spin-flip pauli matrix. Therefore:

$$\gamma = \sigma_y \otimes \sigma_y = \begin{pmatrix} 0 & 0 & 0 & -1 \\ 0 & 0 & 1 & 0 \\ 0 & 1 & 0 & 0 \\ -1 & 0 & 0 & 0 \end{pmatrix}. \tag{1.66}$$

Therefore,

$$\tilde{\rho} = \begin{pmatrix} 0 & 0 & 0 & 0 \\ 0 & 0 & 0 & 0 \\ 0 & 0 & 0 & 0 \\ 0 & 0 & 0 & 0 \end{pmatrix}. \tag{1.67}$$

such that R is the null matrix with all eigenvalues as 0. It can further be deduced then that $C(\rho) = 0$ thus implying that the density matrix corresponds to a separable state, which indeed was the case.

1.11 Fidelity

Often in quantum mechanics, one is tasked with attempting to quantify how similar two mixed states (or two pure states) are to one another. This is incredibly useful for error analysis in assessing the noise in a quantum system when a density matrix needs to be reconstructed in an experiment [20, 18, 33]. The expression for fidelity is presented as:

$$F = Tr\left(\sqrt{\sqrt{\rho_1}\rho_2\sqrt{\rho_1}}\right)^2, \tag{1.68}$$

where ρ_1 is your state you use as a reference and ρ_2 is the state you compare to the first. The result is bounded by 0 and 1, such that $0 \leq F \leq 1$. When $F = 1$ we know that the two matrices are completely identical, and when $F = 0$ they have no similarity.

Chapter 2

Techniques to shape and structure light

The modes that we are interested in are those that are transverse to the direction of propagation of the beam of light (such as the phase and amplitude of the wavefront) [34], the spatial modes. When one refers to shaping a beam (or shaping light) it is implied that the spatial structure is tailored in a desired way [34]. This is accomplished by manipulating the intensity and phase profiles of the laser beam. There are two devices that are employed in our lab to perform this shaping of light, namely: Spatial Light Modulators (SLMs) [35, 36, 37, 38], and Digital Micro-mirror Devices (DMDs) [39, 40, 41]. This chapter focuses on the functionality and calibration of the former.

2.1 Spatial Light Modulators (SLMs)

2.1.1 What is an SLM and how does it work?

A Spatial Light Modulator (SLM), in its simplest form, is a pixelated optical component used to tailor the spatial structure of light by altering the optical path of a beam of incident photons. Physically, it is a pixelated display device with each pixel consisting of many liquid crystal (LC) cells [37, 42], that are sandwiched between two electrode layers. The liquid crystals in each of these pixels can be controlled independently by altering the electric field within these cells. This is achieved by means of a grayscale computer generated hologram with the grayscale indicating how much the LC molecules have to twist. There has to thus be a relation between the phase shift and the gray levels of the image.

SLMs can be split into two categories, reflective, made from liquid crystals on silicon (LCoS), and transparent, made from traditional liquid crystal displays (LCDs, interestingly these SLMs are responsible for the images projected from a standard projector). These can then further be divided into more categories based on how these molecules align with respect to the pixels of the physical display. These can either be vertically aligned nematic (VAN), parallel aligned nematic (PAN), and the most common form, twisted nematic (TN). When a voltage (hence electric field) is applied to a pixel, the molecules in the pixel rotate by an angle $\theta(V)$, such that the extraordinary index of refraction changes according to [37]:

$$\frac{1}{n_e^2(\theta)} = \left(\frac{\cos\theta}{n_e}\right)^2 + \left(\frac{\sin\theta}{n_0}\right)^2. \tag{2.1}$$

In this equation, the ordinary index of refraction stays constant. Setting $V = V_{min}$, such that ideally $\theta(V_{min}) = 0$ should then imply that in (2.1), one would have no change in the effective extraordinary index of refraction $n_e(\theta)$. On the opposing side, for $V = V_{max}$ one would see that $\theta(V_{max})$ results in maximal rotation. What often happens is that the SLM is not yet calibrated and one would have to perform a calibration procedure in order to continue with the experiment. One method to calibrate the SLM will be addressed later in this paper (see 2.1.3).

Since this applied voltage affects the index of refraction, and hence the phase of an incoming wave, the SLM can be considered as a phase retarder. The incoming wave is phase shifted according to the input voltage as governed by the following equation [37]:

$$\Delta\Phi(V) = \frac{2\pi}{\lambda}(n_e(V) - n_o)d. \tag{2.2}$$

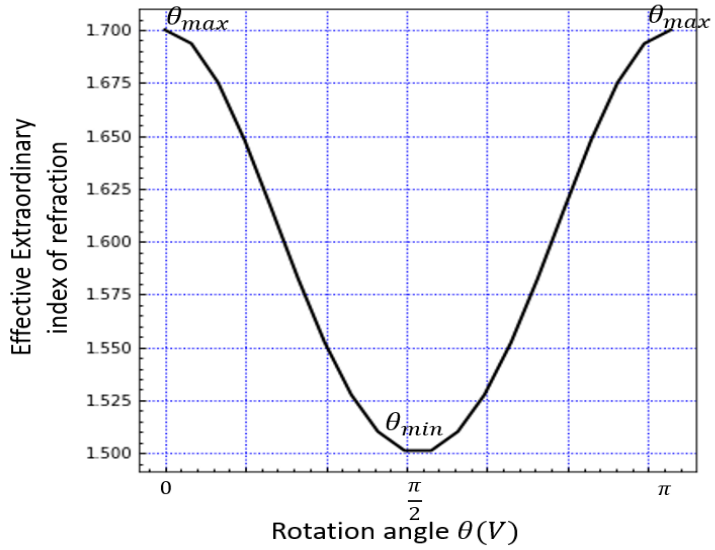


Figure 2.1: Liquid crystal rotation: The effective extraordinary index of refraction varies as the rotation angle changes. The choice for the refractive indices, merely for demonstrative purposes, were $n_e = 1.7$ and $n_o = 1.5$. This rotation angle is further affected by the applied voltage to the liquid crystals. There is clearly a minimum and maximum value for the refractive index corresponding to different rotations of the liquid crystal.

Even though this phase shift will shape the light in a particular way, there are a few key issues that need to be addressed. First of all, the input beam (the one that gets shaped) has to be polarized along a particular direction since only the polarization component that is parallel to the extraordinary axis of the crystal is phase shifted [37, 43]. Secondly, the SLM is a screen constructed from millions of pixels, with tiny gaps between each of these pixels. The incoming light is affected by these gaps as if they were slits, and hence the light gets diffracted off of the SLM in many directions. The result of these contributions is a loss in the efficiency of the reflected/transmitted light.

The 'mode of interest' is the zeroth order diffracted mode which exhibits $> 80\%$ of the original light beam's power [37, 42]. One would filter out these unwanted diffracted orders to eliminate unwanted interference.

The task now is to somehow encode a grayscale image (hologram) onto this SLM which is how the light gets shaped, hence the hologram depends on the desired light structure. Imagine this grayscale image to have 'values of gray' scaling from black (0) to white (256). This information has to be relayed to the SLM which recalls phase shift values from 0 to 2π. This implies that the grayscale image has to induce a phase shift dependent on the level of gray encoded onto each pixel. The grayscale image modulates the light, but only the light along the extraordinary axis is modulated. This modulated light can propagate along the same direction that some of the unmodulated light (which is of no interest to us) travels. The task now is to split the modulated and unmodulated beams up more to see only the desired modulated light mode. To accomplish this, one superimposes a grating onto the original hologram to diffract the already lower intensity zeroth order mode. The new zeroth order is unmodulated and hence discarded, and we focus our attention to the first order modes which are those that are modulated.

2.1.2 Encoding a hologram

The typical properties of light that are modulated include the phase and amplitude. The SLMs used in our lab are phase-only modulating, however with some sleight of hand, one can generate a hologram that is capable of modulating both the phase and amplitude properties of light. There are several techniques enabling one to convert the phase-only response of an SLM, to a complete amplitude and phase response desired for the spatial structuring of light. An analogy to understand this is beautifully represented by stating that the phase-only response traces out a unit circle in the complex plane, and to get a full amplitude and phase response one would require a filled circle in the complex plane [37]. The technique used mainly in our lab are those presented in Ref. [35, 36] where the phase only hologram includes both the phase and amplitude properties that get modulated. Before we get into that, the basic concepts that make this complex amplitude modulation possible are addressed.

Gratings:

Recall that the pixelation of the SLM acts as a diffraction grating. This inherent diffraction results in many unwanted diffraction peaks (coming off of the SLM) which are spatially filtered out, leaving only the desired order. Once a hologram is encoded onto the SLM to modulate the light, the modulated light occurs on-axis with some unmodulated light. This could lead to interference between the modulated and unmodulated light. To rectify this, one can encode another diffraction grating onto the SLM (as part of the hologram), to separate the modulated and unmodulated light into different diffraction orders. In most cases a blazed grating (linear phase ramp from 0 to 2π) is employed which has the advantage of causing all the modulated light to move into a first diffraction order, away from the unmodulated zeroth order. Making the grating frequency high would also separate the first and higher orders, allowing for spatial filtering by using an aperture. This is accomplished through the tactical placement of an aperture in the focal plane between both

lenses of a telescope setup (combination of two lenses for the purposes of magnifying the beam), see **Figure** 2.2.

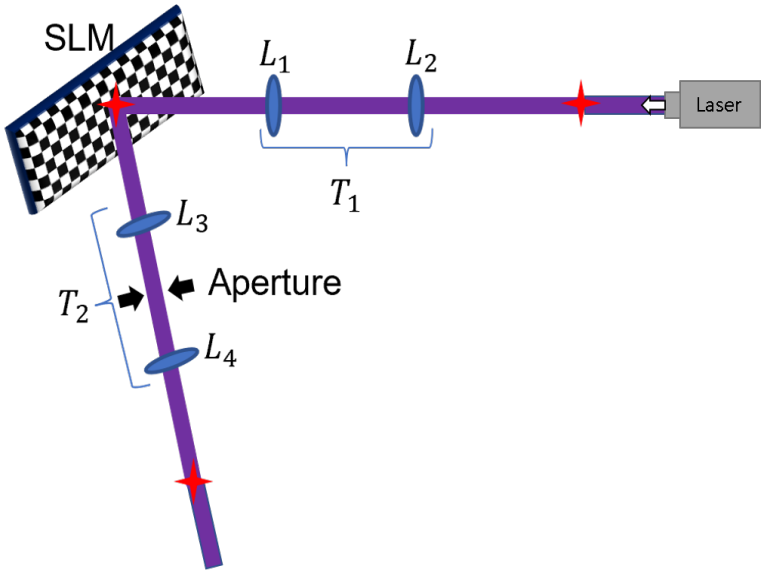


Figure 2.2: SLM setup: The object plane (represented by the red star) on the right is imaged by means of a telescope (T_1), consisting of lenses L_1 and L_2, onto the SLM. This object plane is then further imaged by telescope T_2 to the next object plane (star at the bottom of the image). The aperture is placed between lenses L_3 and L_4 for the purpose of spatial filtering.

This blazed grating diffracts the light away from the zeroth order in a manner dependent on the spatial frequency of the grating. The transfer function for such a grating to be encoded takes the form of [37]:

$$T = \exp[i2\pi(G_x x + G_y y)], \tag{2.3}$$

with $G_x = \frac{1}{L_x}$ and $G_y = \frac{1}{L_y}$ as the spatial frequency of the grating in the x and y directions respectively, and L_x and L_y acting as the periods of the gratings (number of lines making up the gratings) in each direction.

Creating a Hologram:

Recall that the SLM produces a phase-only response. This means that by considering any angular position on the complex unit circle, any phase value can be realized. SLMs cannot create light and therefore cannot directly create a variation of the intensity of the light. If, however, we can push some light into other diffraction orders, we can affect the variation of the amplitude. This can be visualized by moving off of the unit circle to an intermediate radial value less than one, hence resulting in the decrease of the amplitude of the beam [37] (see **Figure** 2.3).

Say one were to modulate between two points on this unit circle, A and B, in order to achieve a desired modulation off of this unit circle at the brown dot in **Figure** 2.3. Let the phase values for these two points A and B be

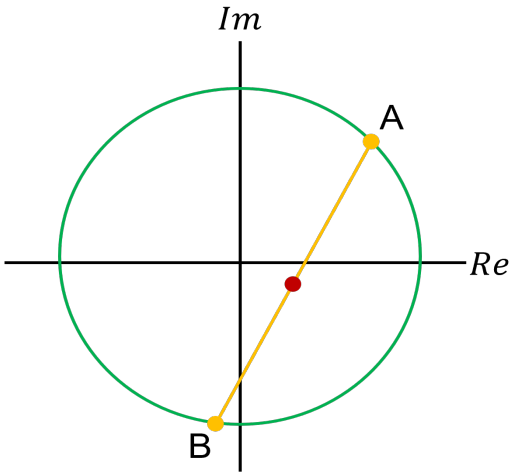


Figure 2.3: Phase and Amplitude Modulation: The green circle shows the unitary circle that defines phase only modulation. To perform the amplitude modulation as well involves moving to a point within this circle (the brown dot) say between two points A and B. This can be generalized for any position within the circle allowing one to effectively modulate to attain any phase and amplitude required.

$$\begin{aligned} A &= e^{(i\phi + i\theta)}, \\ B &= e^{(i\phi - i\theta)}, \end{aligned} \tag{2.4}$$

and let the desired complex value of the brown dot be

$$C = |C|e^{i\phi}. \tag{2.5}$$

To find $|C|$, we simply compute $C = \frac{A+B}{2}$ and compare it to Eq. (2.5):

$$\begin{aligned} C &= \frac{A+B}{2} \\ &= e^{i\phi}\frac{(e^{i\theta} + e^{-i\theta})}{2} \\ &= e^{i\phi}\cos(\theta), \end{aligned} \tag{2.6}$$

and so $|C| = \cos(\theta)$.

There are many methods to performing complex amplitude modulation. We will consider the case that the desired modulated field takes the form of

$$F(x,y) = A(x,y)e^{i\,\phi(x,y)}, \tag{2.7}$$

where $A(x,y)$ refers to the amplitude function and $\phi(x,y)$ is the phase of the field. The SLM has only a phase response and therefore the hologram encoded onto the SLM has to be of the form:

$$H(x,y) = e^{i\,\Psi(\phi,A)}, \tag{2.8}$$

such that the phase component (Ψ) includes both the required phase (ϕ) and amplitude (A) desired. This can be resolved by expressing $H(x,y)$ as a Fourier series over ϕ as follows:

$$H(x,Y) = \sum_{\gamma=-\infty}^{\infty} C_\gamma^A e^{i\gamma\phi}, \tag{2.9}$$

where the dependencies of C_1^A and ϕ, on x and y, have explicitly been left out to simplify notation. The C_γ^A terms are our Fourier coefficients of the expansion represented by:

$$C_\gamma^A = \frac{1}{2\pi}\int_{-\pi}^{\pi} e^{i\psi(\phi,A)}e^{-i\gamma\phi}d\phi. \tag{2.10}$$

The task is to have Eq. (2.9) reproduce Eq. (2.7), which is possible by considering only the first order term

$$H(x,y) = C_1^A e^{i\phi}, \tag{2.11}$$

where

$$C_1^A = cA(x,y), \tag{2.12}$$

and c is a positive constant, this is known as the Signal Encoding Condition [35]. Through the separation of the real and imaginary components of the integral in Eq. (2.10), in order to arrive at the required identity in Eq. (2.12), the following integral conditions have to be fulfilled:

$$\int_{-\pi}^{\pi} \sin[\Psi(\phi,A) - \phi]d\phi = 0, \tag{2.13}$$

$$\int_{-\pi}^{\pi} \cos[\Psi(\phi,A) - \phi]d\phi = 2\pi cA. \tag{2.14}$$

There is a condition [35] stipulating that the integral in Eq. (2.14) must have a maximum value of 2π implying that the coefficient c should have a maximum of 1. This suggests an efficiency limit based on the encoded hologram. Victor Arrizon did work on a class of functions $\Psi(\phi,A)$ with an odd symmetry over ϕ that guarantees the integral in Eq. (2.13) remains validated [35, 36]. Three such functions were suggested with several benefits and downfalls, but only the one that was used in the generation of the modes in this setup is discussed.

Identified as a computer generated hologram (CGH) of Type 3 (as per Victor Arrizon) the phase modulation function for the hologram is given by the function

$$\Psi(\phi, A) = f(A)\sin(\phi). \tag{2.15}$$

In order to determine the corresponding Fourier coefficient in the Fourier series, the Jacobi-Anger identity is used:

$$e^{i f(A)\sin(\phi)} = \sum_{m=-\infty}^{\infty} J_m[f(A)]e^{im\phi}. \tag{2.16}$$

In this equation the J_m terms are the integer-order (m) Bessel functions.

Plugging Eq. (2.15) into the initial hologram equation (Eq. (2.8)), comparing it to Eq. (2.11), and by employing the Jacobi-Anger identity yields:

$$\begin{aligned} e^{i f(A)sin(\phi)} &= C_1^A e^{i\phi}, \\ \implies \sum_{m=-\infty}^{\infty} J_m[f(A)]e^{im\phi} &= C_1^A e^{i\phi}. \end{aligned} \tag{2.17}$$

The last step in Eq. (2.17) is only true for $m = 1$. By taking this into consideration, and by using the signal encoding condition (Eq. (2.12)), we get:

$$J_1[f(A)] = cA. \tag{2.18}$$

The function $f(A)$ can be acquired by numerical inversion of Eq. (2.18), which although it is not shown here, is possible through numerical evaluation techniques (such as Matlab), and is required for the hologram.

To finally attain the required hologram for the SLM, all that has to be included is the grating to separate the modulated light from the unmodulated light. This is accomplished by adapting the function Ψ through incorporating a blazed grating as follows:

$$H(x, y) = f(A)\sin[\phi + 2\pi(G_x x + G_y y)], \tag{2.19}$$

where ϕ is the phase of the desired mode that one wishes to encode.

2.1.3 Calibration of an SLM

As mentioned earlier, one is required to calibrate the SLM to achieve the correct phase change based on the correct input voltage. The input beam of the laser is expanded through the use of a telescope setup (two lenses acting together to magnify the beam), and this expanded beam

is passed through a double-pinhole such that both resultant beams (after the pinhole) have the same intensity, and hit one half of either side of the SLM. A hologram is encoded onto the SLM such that the one half of the screen has a constant reference phase at 0π, while the other half has another phase encoded that can be varied. These two beams reflect off of the SLM and pass through the same lens, and overlap in the far field (the focus) where one would place a CCD camera to evaluate the success of the calibration, see **Figure** 2.4.

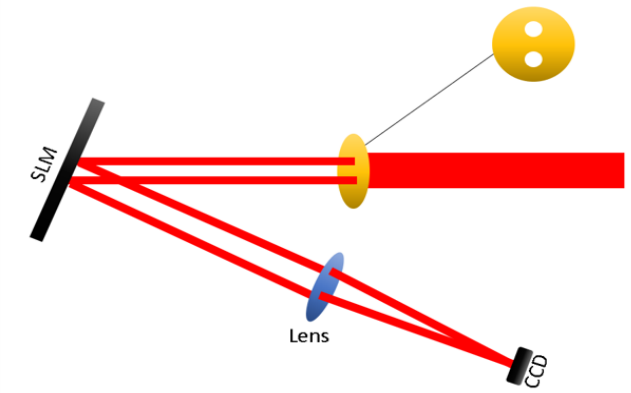


Figure 2.4: Calibration setup: It can be seen here that an expanded beam passes through a double pinhole, creating two thinner beams hitting either side of the SLM and reflecting off of it. These two beams pass through the same lens and focuses to the same point, at which a CCD camera is placed.

The two beams interfere at this position of overlapping, causing interference to occur as a result of the difference in phase between these two beams. When both holograms have the same phase encoded (no phase difference), then an indicator reference point is placed on the image of the CCD camera to determine how the fringes shift. When the phase difference is 2π then this indicator should shift one fringe away, and when the phase difference is π, the indicator should shift between these two fringes, displaying destructive interference. If this is not the case, then the voltages applied to the SLM need to be adjusted in the settings, and tested in a step-wise manner, performing these tests with each voltage, until the fringes shift in the correct manner. Only then is the SLM calibrated correctly. The results of our calibration is shown in **Figure** 2.5.

2.1.4 Investigating the efficiency of an SLM

It was addressed earlier that there are some efficiency issues related to SLMs since there is intrinsic diffraction caused by the pixelation of the screen. The theoretical efficiency due to this loss of light is around 80%. After calibrating the SLM we tested this theoretical efficiency value by introducing a simple blazed grating and comparing the power of the light before and after this grating was applied.

Before the grating was introduced, the power was found to be 0.228 mW. Once the diffraction grating was introduced, the mode of interest now exhibited a power of 0.162 mW. This then implied that the efficiency was 71%. Admittedly, this was not exactly the theoretical value, but

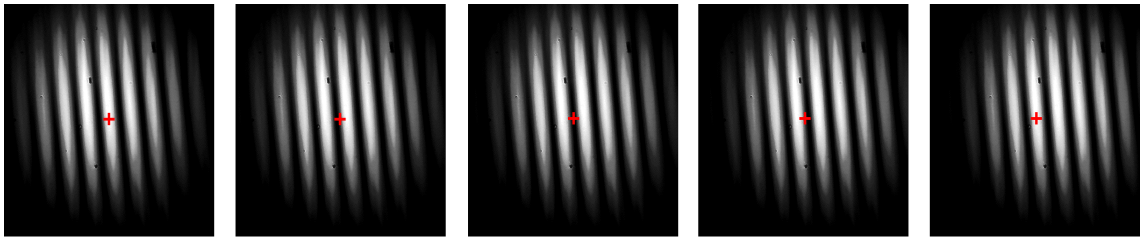


Figure 2.5: Shifting fringes during calibration: The red crosshair represents the reference point about which the fringes shift. The goal is to set the voltages of the SLM such that with a 2π phase shift, the crosshair appears on the bright fringe next to the initial one. These images show the crosshair at various locations as the phase shift was changed. The phase shifts in a, b, c, d, and e are $0, 0.5\pi, \pi, 1.5\pi$, and 2π respectively.

the point of the test was to determine the efficiency of the modulation. It was deduced that the SLM introduced a 29% loss of intensity for the modulated light. This large percentage of lost light could be the result of poorly cleaned optics or incorrectly placed optics.

2.2 Aberrations

2.2.1 Zernike polynomials

One conventional and established technique to correct for astigmatism, or any other aberrations caused within optical setups, is to use the sequence of polynomials that are orthogonal over a unit circle - the Zernike polynomials [44].

The Zernike polynomials are formulated, in polar coordinates, by:

$$Z_n^m(r,\theta) \pm iZ_n^{-m}(r,\theta) = R_n^m(r)\exp(\pm im\theta). \tag{2.20}$$

By equating the real and imaginary components one arrives at the even and odd Zernike polynomials formulated by [44],

$$\begin{aligned} Z_n^m(r,\theta) &= R_n^m(r)\cos(m\theta) \text{ for } m \geq 0, \\ Z_n^{-m}(r,\theta) &= R_n^m(r)\sin(m\theta) \text{ for } m > 0. \end{aligned} \tag{2.21}$$

In these equations $0 \leq r \leq 1$ is the radius of the unit circle, θ is the azimuthal angle stipulating the angular position on the unit circle measured clockwise from the y-axis, m and n are non-negative integers such that $n \geq m$, and $R_n^m(r)$ is the standard radial function described by:

$$R_n^m(r) = \sum_{l=0}^{(n-m)/2} \frac{(-1)^l(n-l)!}{l![\frac{1}{2}(n+m)-l]![\frac{1}{2}(n-m)-l]!} r^{n-2l}. \tag{2.22}$$

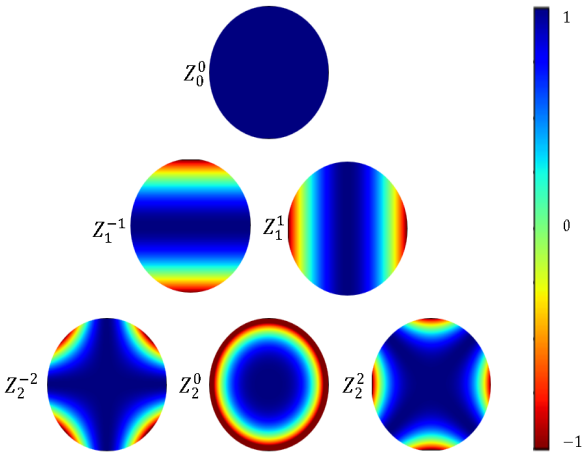


Figure 2.6: Zernike modes: These represent the contribution of the main lower order Zernike modes to what the wavefront would like. These are thus also the modes one would adjust to correct for the corresponding abberation. The Z_0^0 mode is usually referred to as the piston mode. When one would like to correct for squashing in either the vertical or horizontal direction, the y-tilt (Z_1^{-1}) and x-tilt (Z_1^1) is respectively adjusted. To correct for astigmatism either the Z_2^{-2} mode or Z_2^2 mode is adjusted, and if the aberration occurs in the centre, the defocus (Z_2^0) is used [44, 45].

These Zernike polynomials can be used to describe the optical wavefront of the beam. The general function expressing a wavefront is given by;

$$W(r,\theta) = \sum_{n,m} C_n^m Z_n^m, \tag{2.23}$$

with the C_n^m terms indicating the weighting of each of the Zernike modes Z_n^m. The Zernike coefficients used to describe the wavefront are independent of the number of polynomials used in the sequence. The condition of orthogonality implies that any number of subsequent terms can be added without affecting those that have already been computed. This allows a person to control the structure of the wavefront, in a systematic way without causing any further unwanted over-correction. The first few Zernike modes are given in **Figure** 2.6. To correct for unwanted aberrations found in the wavefront, one has to adjust the Zernike coefficients of the corresponding Zernike modes seen in **Figure** 2.6 by changing the sign and magnitude of the coefficient until the abberation is no longer present.

2.3 Generated modes using an SLM

Initially, the task was to generate optical modes by using SLMs in the effort to learn and understand the protocol of shaping light. There was an underlying issue that led to the modes not attaining the correct spatial profile, it was deduced that the calibration was incorrect. Once this had been fixed, and the modes had been regenerated, we could finally verify the modes looked correct. Some of these modes are shown in **Figure** 2.7.

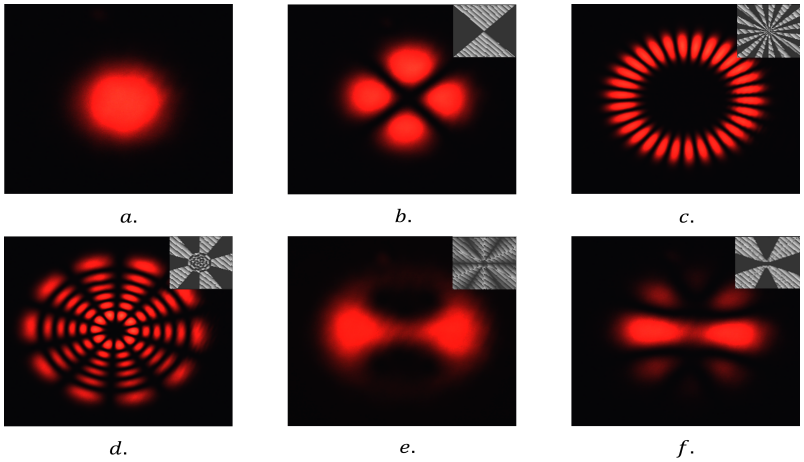


Figure 2.7: Generated modes: Each of these images shows a different mode to which the light intensity profile was shaped. The holograms corresponding to the modulated modes, other than the Gaussian mode, is given on the inset of each image.

2.4 Chapter conclusion

Spatial light modulators are a very useful optical component for performing the structuring of the spatial profiles of light, although it presents a drawback in that it causes a loss of efficiency. The advantage about SLMs are that, not only can one encode the desired hologram for a particular mode, one can also correct for any beam aberrations through the encoding of the Zernike polynomials. This ability to structure light with SLMs plays a role when measurements need to be taken in a particular basis.

Chapter 3

Understanding entangled photons

Entanglement stands as the root of a number of modern techniques in attempting to develop quantum cryptography [46], communication [47, 48], and information theory [49]. A relevant procedure, known as Spontaneous Parametric Down-Conversion (SPDC) [50] is one of the methods responsible for the generation of two entangled photons.

3.1 Spontaneous parametric down-conversion

Spontaneous parametric down-conversion is a non-linear optical process whereby a high-frequency (short wavelength) source of light, known as a pump beam, impinges on and interacts with a non-linear birefringent crystal [51, 52]. This interaction spontaneously converts this high-frequency beam into a pair of lower frequency (longer wavelength) photons which are entangled spatially, temporally, or even through states of polarization [52]. For historical purposes these two photons are individually referred to as signal and idler photons [51]. The are many different types of non-linear crystals that can be used, and they can be made from many different sorts of materials. The choice of non-linear crystal affects the phase matching condition (related to the conservation laws between the initial and output photons) which dictates whether or not the two down-converted photons propagate parallel to one another (collinear) [53]. The two beams of photons do not necessarily possess the same wavelength (and hence frequency and energy) [54, 55], although the degenerate case ($\lambda_s = \lambda_i$) is often considered [56]. A typical SPDC setup is one where the two entangled beams are collinear [51] and have the same wavelength (and hence frequency).

3.1.1 Phase Matching Conditions

During this down-conversion process, the laws of energy and momenta conservation cannot be violated. It is also important to recognize that there is no energy retained in, or dissipated by the medium. The conservation is thus only relevant for photons before and after the crystal. This leads to some constraints placed on the quantum system which are known as the phase matching conditions [57], given by.

$$\begin{aligned} \mathbf{k}_s.\mathbf{r}_s + \mathbf{k}_i.\mathbf{r}_i &= \mathbf{k}_p.\mathbf{r}_p, \\ \omega_s + \omega_i &= \omega_p. \end{aligned} \tag{3.1}$$

Under the condition that the degenerate case is considered ($\omega_s = \omega_i$) with the propagation direction of all three beams as collinear, this becomes [53, 58]:

$$\begin{aligned} k_s + k_i &= k_p, \\ 2\omega_s &= \omega_p. \end{aligned} \tag{3.2}$$

Note that the magnitude of the wave vector obeys a dispersion relation:

$$k(\omega) = n(\omega)\frac{\omega}{c}. \tag{3.3}$$

The wave vector mismatch [58] is used very commonly as a means to stipulate when perfect phase matching occurs. This is given by

$$\Delta k = k_s + k_i - k_p = 0. \tag{3.4}$$

Under the degenerate collinear propagation assumption of perfect phase matching, this reduces to:

$$\begin{aligned} n(\omega_s)\frac{\omega_s}{c} + n(\omega_i)\frac{\omega_i}{c} &= n(\omega_p)\frac{\omega_p}{c}, \\ \therefore 2n(\omega_s)\omega_s &= n(\omega_p)\omega_p, \\ \therefore n(\omega_s) &= n(2\omega_s). \end{aligned} \tag{3.5}$$

Dispersion, however, prevents this condition from ever perfectly occurring in common materials. The non-linear crystals used have the property of birefringence, which allows one to achieve this desired phase matching in the lab environment, even when the beams are not propagating in a collinear fashion. The fact that these crystals are birefringent means there are different indices of refraction for different polarizations. The effective refractive index (that which the light is subjected to due to the propagation through this medium) of the crystals can be adjusted by changing the temperature, or solid angle relative to the axis of propagation, depending on the crystal choice. Modifying these parameters (for example, the temperature and solid angle) would alter the path of propagation of the incoming light, with the result of enforcing the desired phase matching conditions.

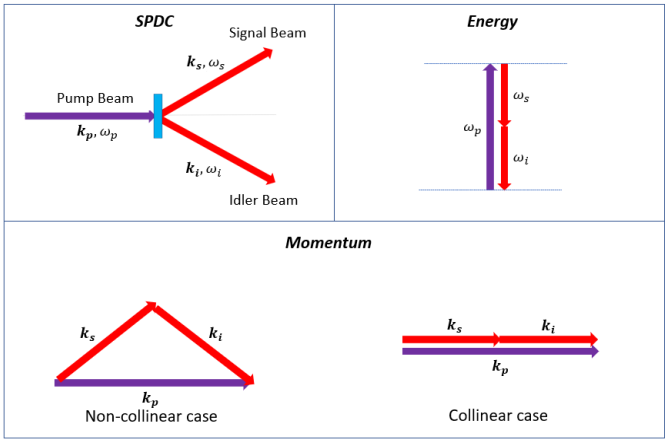


Figure 3.1: Spontaneous Parametric Down Conversion: The concept of SPDC is illustrated as well as the momentum and energy conservation between the signal, idler, and pump beams.

3.1.2 SPDC Quantum State

The process thus far has been described as an input photon, impinging on a non-linear crystal, and two lower-frequency photons are emitted from the crystal. The quantum state of the generated two-photon pair has been extensively studied over the years. The formulation provided below describes the spatial structure of the quantum state, in terms of a modal decomposition over an arbitrary basis:

$$|\psi\rangle = \int_s \int_i d\mathbf{k}_s d\mathbf{k}_i \phi(\mathbf{k}_s, \mathbf{k}_i) \hat{a}^\dagger(\mathbf{k}_s) \hat{a}^\dagger(\mathbf{k}_i) |0,0\rangle, \tag{3.6}$$

where the terms, $\hat{a}^\dagger(\mathbf{k}_s)$ and $\hat{a}^\dagger(\mathbf{k}_i)$ represent the quantum creation operators for the signal and idler mode respectively with wave vectors $\mathbf{k}_s$ and $\mathbf{k}_i$. $|0,0\rangle$ is the vacuum state and $\phi(\mathbf{k}_s, \mathbf{k}_i)$ represents a function of the input pump mode along with the phase matching conditions for the quantum system [51, 59].

Under a plane-wave expansion of the pump beam, the function representing the pump mode and phase matching conditions can be written as [51, 59]:

$$\phi(\mathbf{k}_s, \mathbf{k}_i) = \int_p d\mathbf{k}_p \tilde{E}_p(\mathbf{k}_p) \xi(\mathbf{k}_p - \mathbf{k}_s - \mathbf{k}_i) \delta(\omega - \omega_s - \omega_i). \tag{3.7}$$

The δ-function here represents the conservation of energy during the interaction,

$$\delta(\omega - \omega_s - \omega_i) = \begin{cases} 1 \text{ if } \omega = \omega_s - \omega_i \\ 0 \text{ if } \omega \neq \omega_s - \omega_i \end{cases}, \tag{3.8}$$

whilst the ξ-function is a function relating to the imperfect phase matching conditions [59].

The pump beam propagates through a finite sized crystal of length L. We are only concerned with the interaction that transpires between the transverse plane of the crystal, and the transverse spatial distribution of the beam's field. It is then a sensible decision to work with the transverse component $\mathbf{q}$ of the wave vector as opposed to the usual wave vector $\mathbf{k}$ in what comes. Furthermore, it is assumed that the pump beam is monochromatic with angular frequency $\omega_p = \omega_s + \omega_i$ and an electric field amplitude of $E_p(\mathbf{q}_p)$ [51, 59] equivalent to the spatial distribution of the pump at the input of the non-linear crystal with w as the beam waist. The $\tilde{E}_p(\mathbf{k}_p)$ term from Eq. (3.7) thus becomes:

$$\begin{aligned}\tilde{E}_p(\mathbf{q}_p) &= \tilde{E}_p(\mathbf{q}_p)\delta(\omega - \omega_s - \omega_i) \\ &= \tilde{E}_p(\mathbf{q}_p)\delta(\omega - \omega_p).\end{aligned} \tag{3.9}$$

with $\tilde{E}_p(\mathbf{q}_p)$ being the Fourier transform of the electric field amplitude of $E_p(\mathbf{q}_p)$.

We now move on to describe the properties of the crystal, which affects the phase matching conditions. For a finite crystal of length L in the longitudinal direction, and large transverse area, the phase matching condition becomes [51, 59]:

$$\xi(\mathbf{k}_p - \mathbf{k}_s - \mathbf{k}_i) = \delta(\mathbf{q}_p - \mathbf{q}_s - \mathbf{q}_i) \times \sqrt{\frac{L}{\pi k_p}}\text{sinc}\left(\frac{L\Delta k_z}{2}\right)\exp\left(\frac{-iL\Delta k_z}{2}\right). \tag{3.10}$$

Here $\Delta k_z = k_{p,z} - k_{s,z} - k_{i,z}$. The terms given by $k_{\cdot,z} = \sqrt{k^2 - q^2} = \sqrt{n^2(\omega)\omega^2/c^2 - q^2}$ is the longitudinal component of the wave vector $\mathbf{k}$, analogous to the transverse component which was denoted as $\mathbf{q}$, ω is the angular frequency of the corresponding beam, and $n(\omega)$ is the refractive index as said before.

The function $\phi(\mathbf{k}_s, \mathbf{k}_i)$, which now becomes $\phi(\mathbf{q}_s, \mathbf{q}_i)$ since the transverse components are again employed, stands as

$$\begin{aligned}\phi(\mathbf{q}_s, \mathbf{q}_i) = &\int_p d\mathbf{q}_p \tilde{E}_p(\mathbf{q})\delta(\omega - \omega_p)\delta(\mathbf{q}_p - \mathbf{q}_s - \mathbf{q}_i) \\ &\times \sqrt{\frac{L}{\pi k_p}}\text{sinc}\left(\frac{L\Delta k_z}{2}\right)\exp\left(\frac{-iL\Delta k_z}{2}\right)\delta(\omega - \omega_s - \omega_i).\end{aligned} \tag{3.11}$$

Determining the integral for the wave vector $\mathbf{k}$ is equivalent to determining the integral over the transverse component $\mathbf{q}$ and the angular frequency ω, and since there is a delta-function present, the computation of the integral becomes very easy. Only the situation for when $\delta(0)$ is present under the integral is considered, hence causing $\omega = \omega_p = \omega_s + \omega_i$ and $\mathbf{q}_p = \mathbf{q}_s + \mathbf{q}_i$:

$$\phi(\mathbf{q}_s, \mathbf{q}_i) = \tilde{E}_p(\mathbf{q}_s + \mathbf{q}_i)\sqrt{\frac{L}{\pi k_p}}\text{sinc}\left(\frac{L\Delta k_z}{2}\right)\exp\left(\frac{-iL\Delta k_z}{2}\right). \tag{3.12}$$

When the angle between the signal and idler beams is small enough, the z-component of the momentum vector $\sqrt{k^2 - q^2}$ can be approximated as $k - \frac{q^2}{2k}$ where $q = |\mathbf{q}|$. Then, after solving the Fourier transform integral, the phase matching function becomes [51]:

$$\phi(\mathbf{q}_s, \mathbf{q}_i) = \overbrace{\sqrt{\frac{2}{\pi}} \frac{w_p}{\sqrt{2\pi}} e^{-\frac{w_p^2}{4}|\mathbf{q}_s + \mathbf{q}_i|^2}}^{\text{Pump}} \underbrace{\sqrt{\frac{L}{\pi k_p}} \text{sinc}\left(\frac{L|\mathbf{q}_i - \mathbf{q}_s|^2}{4k_p}\right) e^{-i\frac{L|\mathbf{q}_i - \mathbf{q}_s|^2}{4k_p}}}_{\text{Phase Matching term}}. \tag{3.13}$$

In the thin crystal limit, the phase matching condition is only applicable in the transverse direction. This is mathematically identical to setting the phase matching term in the above equation to one [59]. This then implies that the phase matching function, and hence the entangled SPDC state, depends strictly on quantities relating to the pump beam.

3.2 Spiral Bandwidth

To ensure that one indeed has entangled photons, one would have to detect each down-converted photon in a specific mode (dependent on a set of orthogonality and conservation laws) in coincidence. The LG modes have been investigated before for its role in SPDC [60, 61] and is the set of modes investigated here. The radial (p) indices of the pump, signal, and idler modes are intentionally set to zero leaving only the OAM index (ℓ) to be worked with. Since momentum is conserved, OAM naturally also follows this conservation i.e. [51, 62, 63]

$$\ell_p \hbar = \ell_s \hbar + \ell_i \hbar. \tag{3.14}$$

Assuming the pump beam is a Gaussian beam, with $\ell_p = 0$, the value for the signal and idler modes are restricted by $\ell_s = -\ell_i$. Now, to have a coincidence, one has to detect a signal photon with OAM of $-|\ell|$ while at the same time detecting the idler photon to have OAM = $+|\ell|$ [62]. This would occur for all values of $|\ell|$, but with each ℓ having a different probability, these are known as the probability amplitudes and are denoted by $|C_{\ell_s,\ell_i}|^2$ under the usual condition that the sum of all probabilities equate to unity:

$$\sum_{\ell_s,\ell_i} |C_{\ell_s,\ell_i}|^2 = 1. \tag{3.15}$$

These C_{ℓ_s,ℓ_i} are known as the coincidence amplitudes and are determined by the overlap integral between the initial pump mode, and both the signal and idler modes all in the LG basis [51, 62]. Generalizing this for any OAM and radial momenta, this overlap integral looks as follows:

$$\begin{aligned} C^{\ell_s,\ell_i}_{ps,pi} &= \langle \psi_s, \psi_i | \psi_{\text{SPDC}} \rangle \\ &= \int\int d\mathbf{q}_s d\mathbf{q}_i \phi(\mathbf{q}_s, \mathbf{q}_i) \left[LG^{\ell_s}_{p_s}(\mathbf{q}_s)\right]^* \left[LG^{\ell_i}_{p_i}(\mathbf{q}_i)\right]^*. \end{aligned} \tag{3.16}$$

Remember, when the thin crystal limit is considered, the longitudinal component of the phase matching conditions is ignored such that $\phi(\mathbf{k}_s, \mathbf{k}_i)$ effectively only depends on the pump mode, which would also be an *LG* mode. The *LG* modes, and in fact all solutions to the Helmholtz equation, is a countable set of modes [64]. This means that the biphoton state equation from equation (3.16) can instead be accurately represented as a sum over the signal and idler indices:

$$|\psi\rangle = \sum_{\ell_s}\sum_{\ell_i}\sum_{p_s}\sum_{p_i} C^{\ell_s,\ell_i}_{ps,pi}|\ell_s, p_s\rangle|\ell_i, p_i\rangle. \tag{3.17}$$

This state equation can again further be generalized by introducing extra indices denoting the beam size. Experimentally, one can control the 'detection' of the beam size. The beam width of the pump beam can also be controlled, although it is usually fixed. A more useful quantity, the relative beam waist γ is used, which relates the beam waists of the signal and idler photons, to that of the pump beam (source) [62, 63] ($\gamma_s = \frac{w_p}{w_s} = \gamma_i = \frac{w_p}{w_i}$). Usually, these two gamma values are equalized ($\gamma_s = \gamma_i = \gamma$) such that only one value is usually needed in computations related to SPDC.

The probability amplitude of each biphoton state is dependent on this beam ratio γ [51]. For small values of γ, the probability amplitudes go down as the value of the angular momentum increases. When plotting the probability of the biphoton state against the corresponding angular momenta values, a plot (sort of resembling a Cauchy distribution curve) arises. This plot is typically referred to as an entanglement spectrum, specifically for the *LG* basis, a spiral spectrum, and an example of such a spiral spectrum figure can be seen in **Figure** 3.2. The spiral bandwidth (SB) is the width of the spectrum. An issue arises here, however, as this plot (centered around 0 in the case of $\ell_p = 0$ [65]) represents different probabilities for each pair of ℓ_s and ℓ_i values (higher probability for lower $|\ell|$) values. One would usually like to flatten the spectrum such that all the probabilities are equalized. This would generate a complete high-dimensional, maximally entangled Bell basis of states (such that the probability of all these $|\ell|$ values are equal) [52].

There are two very useful quantities that can be utilized to distinguish how many modes are available for quantum communication, computation, and many other quantum protocols. The first is the Full-width at Half-maximum (FWHM) [66]. To determine the FWHM, you simply half the value of the maximum probability and impose this as your minimum considered probability value. The number of modes that then have a probability higher than this is considered the FWHM. To make this concrete, looking at **Figure** 3.2 *b*. one can notice that the maximum probability is around 0.06, thus the Half-maximum is 0.03. The amount of modes with probability above this value, and hence the FWHM is 15 modes. This is the number of relevant detectable modes within the spectrum, and provides an indication as to how much information can be encoded per photon.

The next useful quantity is known as the Schmidt number [62, 67, 68]

$$K = \frac{1}{\sum[C^{\ell_s,\ell_i}_{ps,pi}]^4}. \tag{3.18}$$

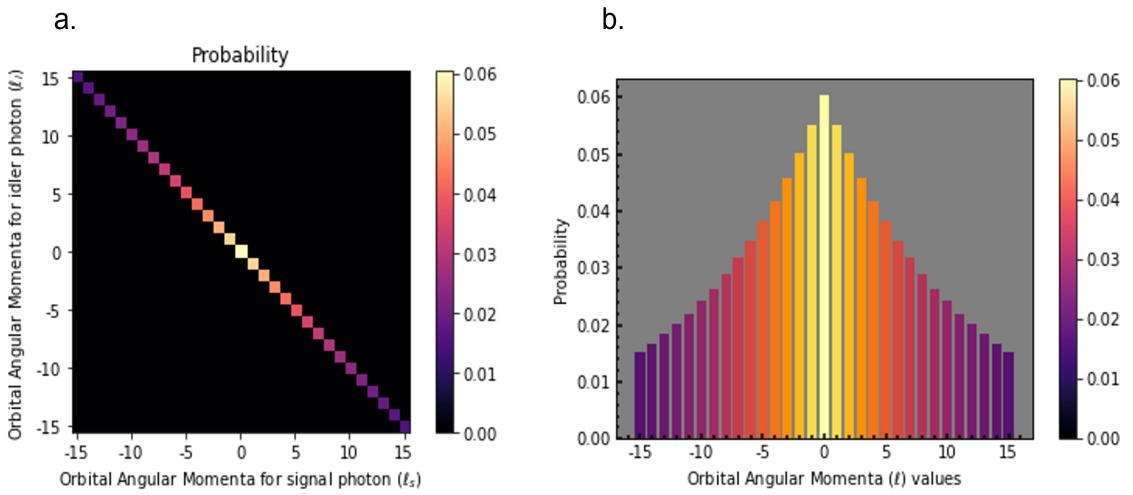


Figure 3.2: Theoretical spiral bandwidth plots: The concept of the OAM spectrum is depicted here. This is for the case when $\ell_p = 0$. As discussed, the probability is maximum at the centre when $\ell_s = \ell_i = 0$ and drops off for higher order modes. The reason that we only have an anti-diagonal in *a*. in this case is due to the restriction imposed on the values of ℓ_s and ℓ_i. Since there are only elements along the anti-diagonal, it is easy to visualize a 2D cross-sectional probability distribution as show in *b*.

This quantity is useful in determining the dimension of entanglement in the quantum system. When this value of K is larger, one has a higher entanglement dimension [62]. This also implies that when using photons to carry information, more information can be encoded simultaneously per photon.

3.3 Bell Measurement

3.3.1 Understanding the origins of entanglement - CHSH inequality

It all began in the year 1935 in the famous paper written by Einstein, Podolsky, and Rosen (commonly known as the EPR paradox). The idea of the paper relies on demonstrating a thought experiment in an attempt to portray their logic of why quantum mechanics was incomplete. The most notably introduced concepts were those of locality, realism, determinism, and completeness [69]. Let us briefly delve into some of these concepts so that we may understand the issues that the EPR trio had come across.

Locality specifically refers to the physical distance between two interacting quantum systems, and the time it takes for such an interaction to occur. A non-local interaction is considered to be an interaction occurring over a long space-like separation, where an experiment performed in one location on one interacting member influences the second member instantaneously, regardless of the distance that lies between them [70, 71, 72].

The next concept introduced is that of completeness. In the context of the EPR paper, a theory is considered complete if there is a mapping of the measured quantity to a physical element in

reality [69]. Therefore, realism implies the physical existence of a measured quantity, so long as it is predicted with complete certainty.

The distinction between determinism and probabilistic theories is that a deterministic system is one where the outcome of a measurement is definite and certain (for a specific choice of input parameters and external effects), while the outcome of a probabilistic system is not. Probabilistic theories are, as the name suggests, probability dependent. The outcome of a measurement on the same system, in a probabilistic theory, can yield different results corresponding with different probability values. The Copenhagen interpretation of quantum mechanics is hence of a probabilistic nature whilst classical mechanics is of a deterministic nature.

Lastly, a hidden variables theory, either local (Einstein [69]) or non-local (Bohm [73],)is a theory suggesting the presence of hidden, or missing, variables in quantum mechanics that would correct for the incompleteness present in quantum mechanics. These theories suggest a secret unknown complete state describing the quantum system.

With these concepts now defined, we can move back on to the topic of the EPR paper and discuss its significance. As stated before, the original motivation for the paper was to demonstrate the incompleteness of the quantum theory. The Copenhagen interpretation of quantum theory suggests that the physical state of any quantum system is completely defined by the wave function of the system [73] - something that only provides the probabilities of a result if the exact same measurement were to be repeated on an ensemble of experiments. This probabilistic nature was criticized by Einstein who believed that for real physical results to be the output of a measurement, one would require the existence of precise and well-defined variables as is the case in the deterministic classical regime. The thought experiment that was thus presented in the paper was the following:

Two systems, specifically particles, were to interact with one another in a correlated manner such that neither the position, nor the momentum, of the system as a whole could be determined, but by making a measurement on the position, or momentum, of one particle, one would be able to predict with complete certainty what the position, or momentum, of the second particle would be. A key assumption in this thought experiment was that the principle of locality holds. This meant that that if the particles were sufficiently spatially separated, the measurement on one particle should not influence the measurement on the second. However, if these two particles were to be sufficiently spatially separated, and a measurement were to be made on one particle of this bipartite wave function, the wave function (under the Copenhagen interpretation) would collapse such that the first particle would be found in a state, but since the wave function had collapsed, the second particle would indeed be found in a specified state due to the resultant measurement on particle one. It appeared that even though locality was assumed, a measurement on one particle would have indeed influenced the measurement of the state of the distant particle. An example situation of such a case would be to consider two electrons in a singlet state, by measuring the first particle to be in the "up" spin state, one can conclude that the second particle would be in the "down" spin state, solely by virtue of the collapsing nature of the wave function under this interpretation. This influence of the first particle's measurement on the second appeared to occur instantaneously, which would violate Einstein's relativity theory. This led to the conclusion

that the theory of quantum mechanics as it currently had stood was incomplete and led to the suggestion of a hidden variables theory [74].

It was initially unclear what Einstein's issue was with the quantum theory, but through close examination of his famous statement: "It seems hard to sneak a look at God's cards. But that he plays dice and uses 'telepathic' methods' (as the present quantum theory requires of him) is something I cannot believe for a moment" [75] , it appears that his issue did not lie with determinism or realism, but with locality. This is clear through his famous statement of initially dubbing entanglement as "spooky-action-at-a-distance" [71, 72].

One year after the EPR paper had been published, the term entanglement was coined [76]. In this attempt to explain this seemingly paradoxical phenomenon, it was found that even though these particles are indeed entangled, no actual 'information' ever travels faster than the speed of light. The second particle's state is determined by making a measurement on the first particle of the entangled pair. This is the case because of the Copenhagen formulation used in quantum mechanics. Information transfer is never an issue, hence there is in fact no violation of relativity. What happens in entanglement is that when a measurement is made on one entangled particle, the second particle reduces to a state which is unknown until a measurement on this particle is then also made. Since the initial measurement would yield a random result, and since these measurements would have to be made physically by an observer, there is no violation of special relativity.

Over the years, several approaches to understand entanglement were of course introduced. One of these, which was already mentioned, is the Hidden Variables Theory. There was also a theory of non-locality which was compatible with the theory of special relativity and allowed for entanglement to be described without violating the speed of light [77]. The last approach mentioned here is based on the work of John Stewart Bell. His work gave rose to the Bell inequality [20, 78, 79]. The essence of this inequality is that two entangled particles do not satisfy the Bell inequality, as they violate the idea of locality. An experimental adaption to the Bell inequality was developed and named the Clauser-Horne-Shimony-Holt (CHSH) inequality [80]. This inequality was to be used experimentally to show a violation of the local hidden variables theory.

3.3.2 CHSH inequality

The CHSH inequality was used many times over the years, to report Bell violations related to the correlations present in superposition states of two polarization entangled photons [81, 82] . There is, however, no stipulation that one cannot extend this to other degrees of freedom, beside polarization, for example OAM-entangled states may also be used. To proceed further with this topic, it can be useful to work with orbital angular momentum as the considered degree of freedom. The orbital angular momentum index theoretically spans the whole number line $[-\infty, \infty]$. We will assume a qubit state, analogous to the qubit state for the polarization degree of freedom (equation (1.32)), to proceed with this topic. The generalized OAM-qubit state is given by [18, 83]:

$$|\psi\rangle = \cos(\theta/2)|\ell_1\rangle + e^{i\phi}\sin(\theta/2)|\ell_2\rangle, \tag{3.19}$$

resulting in a similar sphere construction akin to the polarization's Poincaré sphere, this being known as a Bloch Sphere (see **Figure** 3.3).

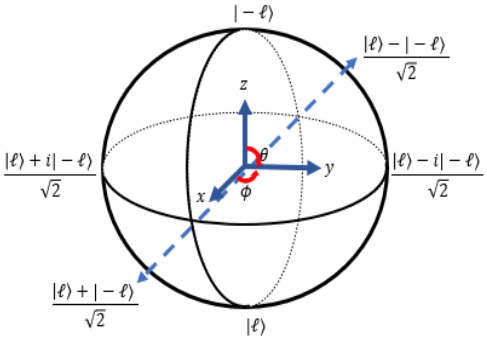


Figure 3.3: Bloch Sphere: This demonstrates what is meant by the Bloch sphere. The states on the surface of the Bloch sphere represent the state of the photon. The substates $|\ell\rangle$ are used since one works in the OAM subspace.

The idea is to work with the superposition of OAM states between two entangled photons [84, 85] which is equivalent to working with states described on the equatorial circle of the Bloch sphere. Under the condition that one works in the *LG* basis with all radial indices set to 0, and by setting the OAM index of the pump beam to 0 ($\ell_p = 0$), these superposition states can be defined by [84, 85]:

$$|\theta\rangle = \frac{1}{\sqrt{2}}(|\ell\rangle + e^{2i\theta}|-\ell\rangle). \tag{3.20}$$

The biphoton state is given by:

$$|\Psi\rangle = \frac{1}{\sqrt{2}}(|\ell\rangle|-\ell\rangle + |-\ell\rangle|\ell\rangle). \tag{3.21}$$

By placing SLMs within each path of the signal and idler photons, the superposition state for each photon can be encoded onto its respective SLM. One detects photons (in these respective states) in coincidence using an optical setup throughout the procedure. These coincidences are directly related to the probability, similar to the overlap integrals introduced in the previous subsection. These probabilities are determined by cycling through all the possible θ values. At first, θ_s is kept constant and θ_i is scanned over a series of values, each time determining the probabilities. Once one has scanned over these θ_i values, one can increment θ_s and systematically run through the θ_i values again.

The probabilities, and hence a proportional relation for the coincidences, are determined in the usual way via the overlap integral [83, 84, 85]:

$$\begin{aligned} C(\theta_s,\theta_i) &= |\langle\theta_s,\theta_i|\Psi\rangle|^2 \\ &= |\langle\theta_s|\langle\theta_i||\Psi\rangle|^2 \\ &= \frac{1}{8}|(\langle\ell_s| + e^{-2i\theta_s}\langle-\ell_s|)(\langle\ell_i| + e^{-2i\theta_i}\langle-\ell_i|)(|\ell_s\rangle| - \ell_i\rangle + |-\ell_s\rangle|\ell_i\rangle)|^2, \end{aligned} \tag{3.22}$$

and by the orthogonality of the OAM states,

$$\begin{aligned} C(\theta_s,\theta_i) &= \frac{1}{8}|e^{-2i\theta_s} + e^{-2i\theta_i}|^2 \\ &= \frac{1}{8}(e^{-2i\theta_s} + e^{-2i\theta_i})(e^{2i\theta_s} + e^{2i\theta_i}) \\ &= \frac{1}{8}(2 + e^{2i(\theta_s-\theta_i)} + e^{-2i(\theta_s-\theta_i)}) \\ &= \frac{1}{4}(1 + \cos(\theta_s - \theta_i)) \\ &= \frac{1}{8}(\cos^2(\theta_s - \theta_i)), \end{aligned} \tag{3.23}$$

which of course adopts a maximum value when $\theta_s - \theta_i = m\pi\ , \forall\ m \in \mathbb{Z}$.

The accepted CHSH inequality is [80]:

$$S = |E(\theta_s,\theta_i) - E(\theta_s,\theta_i^{'}) + E(\theta_s^{'},\theta_i) + E(\theta_s^{'},\theta_i^{'})| \leq 2\sqrt{2}, \tag{3.24}$$

where the primes (′) simply imply that the primed states are different from their respective unprimed states. The $E(\theta_s,\theta_i)$ term represents the photon correlation between the measurements in the signal and idler arms, it is experimentally determined by computing [83, 84, 86]

$$E(\theta_s,\theta_i) = \frac{C(\theta_s,\theta_i) - C(\theta_s^{\perp},\theta_i) - C(\theta_s,\theta_i^{\perp}) + C(\theta_s^{\perp},\theta_i^{\perp})}{C(\theta_s,\theta_i) + C(\theta_s^{\perp},\theta_i) + C(\theta_s,\theta_i^{\perp}) + C(\theta_s^{\perp},\theta_i^{\perp})}, \tag{3.25}$$

where $\theta^{\perp} = \theta + \pi/2$. The result of this computation is known as the Bell parameter. When this Bell parameter exceeds the value of 2 ($|S| > 2$) it is said that the system is of a quantum nature and violates general assumptions surrounding classical physics, including the theory of locality [85]. Under this violation, it is concluded that the quantum system is entangled. It has been deduced from theory that the largest violation of the Bell Inequality occurs at orientations $\theta_s = 0, \theta_i = \frac{\pi}{8\ell}, \theta_s^{'} = \frac{\pi}{4\ell}$, and $\theta_i^{'} = \frac{3\pi}{8\ell}$ [84, 85].

3.4 Quantum State Tomography

Once an experimenter has verified that the setup indeed produces entangled photons (through the violation of the bell inequality), one would endeavour to reconstruct the quantum state of

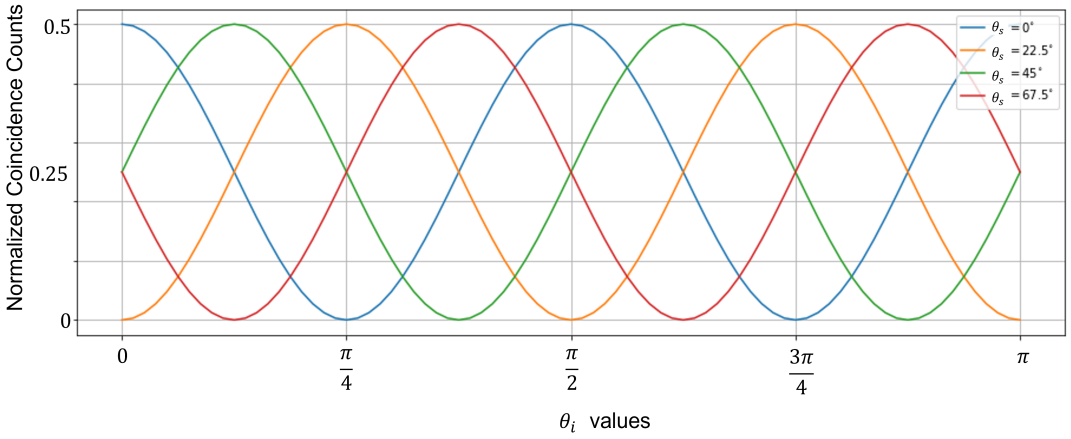


Figure 3.4: Bell Measurement: This is a simulated perfect Bell measurement case displaying the trend of the bell measurement curve. The normalized coincidence counts would usually be plotted as a function of the relative angle between the superposition of OAM states. The θ_s (corresponding to the signal photons hitting its SLM) values are kept at a constant value, while the θ_i (corresponding to the idler photons hitting its SLM) values are varied. This is done for four cases of $\theta_s = \{0, \frac{\pi}{4}, \frac{\pi}{2}, \frac{3\pi}{4}\}$.

these two entangled photons. This procedure is known as Quantum State Tomography (QST) and is responsible for establishing accurate information about a quantum system whose state is not yet known [87, 88]. The technique draws its roots from general tomography where one would use sectional images of a particular object, to build up the full image of the object from scratch, such as an X-Ray. In quantum mechanics, it is familiar that any measurement on a quantum system would change the state that it is in, rendering it impossible to make multiple measurements on a single state. This is the reason as to why one requires an ensemble of identical copies to make the required measurements which allows for the reconstruction of the desired state through tomography. This quantum state reconstruction technique was first suggested in the celebrated paper by Fano in 1957 [89], and has been a cornerstone of quantum state reconstruction in many experimental procedures ever since [90, 91, 92]. Here we will describe the procedure to perform a QST in the OAM subspace, firstly for a qubit case, and thereafter for higher dimensional cases.

3.4.1 Theory of QST

To begin, recall the general formulation for the density matrix given by Eq. (1.37):

$$\rho = \sum_m p_m |\psi_m\rangle\langle\psi_m|, \tag{3.26}$$

where the pure states,

$$|\psi_m\rangle = \sum_i \sum_j c_m^{ij} |i\rangle_A \otimes |j\rangle_B, \tag{3.27}$$

are two particle qubit states defining the m^{th} state with $|i\rangle$ as the eigenstate of photon A, $|j\rangle$ as the eigenstate of photon B, and where c_m^{ij} are complex coefficients. There is an issue that lies in the fact that one requires these complex coefficients to be known which, in general, cannot directly be measured [87]. We therefore choose a different formulation of the density matrix, better suited to performing different perspective measurements on a quantum system, given in terms of the rotational Pauli matrices, and the identity matrix [18]:

$$\begin{aligned}\rho &= (\frac{1}{2}\sum_{i=0}^{3}\rho_i\sigma_i)\otimes(\frac{1}{2}\sum_{j=0}^{3}\rho_j\sigma_j)\\ &= \frac{1}{4}\sum_{i=0}^{3}\sum_{j=0}^{3}\rho_{ij}\sigma_i\otimes\sigma_j,\end{aligned} \tag{3.28}$$

where σ_0 is the identity matrix, and σ_1,σ_2,and σ_3 are the Pauli matrices.

The qubit pair can be described geometrically as existing on the surface of a sphere known as the Bloch sphere (**Figure** 3.5) (more specifically a higher order Bloch sphere), similar to the Poincaré sphere introduced in the first chapter (see **Figure** 1.5).

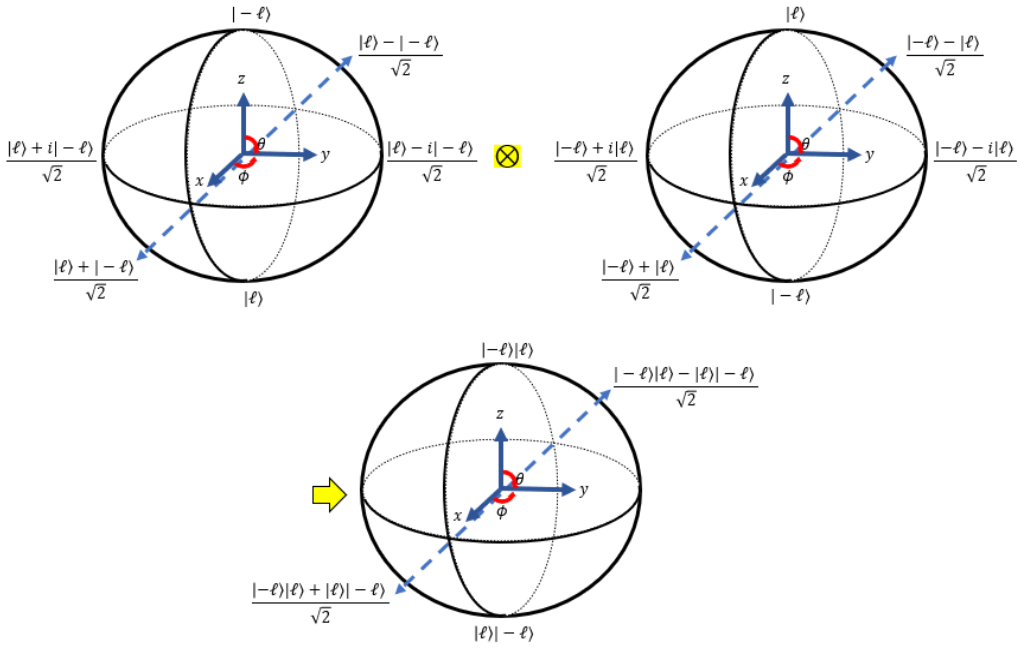


Figure 3.5: Higher Order Bloch Sphere: This depicts what is meant by the higher order Bloch sphere. The states on the surface of the first two Bloch spheres represent the state of each individual photon respectively. The substates $|\ell\rangle$ are used since the OAM subspace is used.

Since the matrices $\sigma_{i,j}$ are 2×2 matrices, there exist two eigenvectors ($|F^1\rangle$ and $|F^2\rangle$) and corresponding eigenvalues (λ^1 and λ^2) for each, hence

$$\begin{aligned}\sigma_i \otimes \sigma_j =&(\lambda_i^1|F_i^1\rangle\langle F_i^1| + \lambda_i^2|F_i^2\rangle\langle F_i^2|) \otimes (\lambda_j^1|F_j^1\rangle\langle F_j^1| + \lambda_j^2|F_j^2\rangle\langle F_j^2|)\\ =&\lambda_i^1\lambda_j^1(|F_i^1\rangle\langle F_i^1| \otimes |F_j^1\rangle\langle F_j^1|) + \lambda_i^1\lambda_j^2(|F_i^1\rangle\langle F_i^1| \otimes |F_j^2\rangle\langle F_j^2|)\\ &+ \lambda_i^2\lambda_j^1(|F_i^2\rangle\langle F_i^2| \otimes |F_j^1\rangle\langle F_j^1|) + \lambda_i^2\lambda_j^2(|F_i^2\rangle\langle F_i^2| \otimes |F_j^2\rangle\langle F_j^2|).\end{aligned} \tag{3.29}$$

The notation $|\cdot\rangle\langle\cdot|$ is a projector, as described in the first chapter, and can simply be determined by making a measurement on the system. The problem here is that the tensor product $|\cdot_A\rangle\langle\cdot_A| \otimes |\cdot_B\rangle\langle\cdot_B|$ can only be determined by performing a joint measurement on both photons simultaneously (hence the reliance on determining the measurements in coincidence). The expectation values for the matrix elements of the density matrix are calculated using a projective measurement given by

$$\begin{aligned}\rho_{ij} =&\lambda_i^1\lambda_j^1\langle F_i^1F_j^1|\rho|F_i^1F_j^1\rangle + \lambda_i^2\lambda_j^2\langle F_i^2F_j^2|\rho|F_i^2F_j^2\rangle\\ &+ \lambda_i^1\lambda_j^2\langle F_i^1F_j^2|\rho|F_i^1F_j^2\rangle + \lambda_i^2\lambda_j^1\langle F_i^2F_j^1|\rho|F_i^2F_j^1\rangle,\end{aligned} \tag{3.30}$$

where as before the notation $|ab\rangle = |a\rangle \otimes |b\rangle$ is used.

For each value of i and j, the expectation value ρ_{ij} requires 4 measurements. That means that for 16 matrix elements, a total of 64 measurements is required, although it has been seen that in fact only 36 measurements are required as some measurements have the same computation [18].

Experimentally, the physical values of the density matrix can be taken from the normalized coincidence count rates for the set of measurements (which is denoted C_{exp}) obtained from a photodetector system. The measurement states encoded onto each SLM can be one of six, thus providing the 36 required measurements for determining the density matrix. These 36 elements give an over-complete set of probabilities within which are those that belong to the density matrix that is desired (this follows the approach set in [91]). These six measurement states are given by:

$$\begin{aligned}|\psi_1\rangle =&|\ell\rangle,\\ |\psi_2\rangle =&|-\ell\rangle,\\ |\psi_3\rangle =&|\frac{1}{\sqrt{2}}(|\ell\rangle + |-\ell\rangle),\\ |\psi_4\rangle =&\frac{1}{\sqrt{2}}(|\ell\rangle + e^{i\frac{\pi}{2}}|-\ell\rangle),\\ |\psi_5\rangle =&\frac{1}{\sqrt{2}}(|\ell\rangle + e^{i\pi}|-\ell\rangle),\\ |\psi_6\rangle =&\frac{1}{\sqrt{2}}(|\ell\rangle + e^{i\frac{3\pi}{2}}|-\ell\rangle).\end{aligned} \tag{3.31}$$

What one does now is compose a guessed density matrix

$$\rho_g = \frac{G^\dagger G}{Tr(G^\dagger G)}, \tag{3.32}$$

with G being a matrix by nature, defined by a linear combination of the generalized (for a four-dimensional matrix) Gell-Mann matrices and the Identity matrix [86, 87]. A projective measurement of this density matrix is performed again through the use of the states in Eq. (3.31), yielding another 36 elements (C_{guess}) which is normalized (as probabilities).

At this point, there are normalized coincidence counts (probabilities) given by C_{exp}, and there are the normalized measurements (probabilities) based on the guessed state that are given by C_{guess}. One would seek to compare the similarity by means of the maximum likelihood estimation [18, 87, 92], which is to minimize the Chi-squared quantity given by

$$\chi^2 = \left(\sum_{i=1}^{36} \frac{C^i_{exp} - C^i_{guess}}{\sqrt{C^i_{exp} + 1}} \right). \tag{3.33}$$

The guessed density matrix is then consistently updated until this relation is minimized. This provides the closest, and most accurate, reconstructed biphoton state. There are a few conditions that this guessed density matrix is required to satisfy: it has to have positive eigenvalues, have a unit trace, and be hermitian. An example of a 2-dimensional QST measurement and the corresponding real, and imaginary density matrices, are shown in **Figure** 3.6.

We now move to higher dimensional quantum state tomography [93, 87]. The generalization for the density matrix of d^2-dimensional biphoton qudit can again be formulated as a linear combination of the Identity matrix and generalized Gell-Mann matrices:

$$\rho = \frac{1}{d^2} \tau_0 \otimes \tau_0 + \sum_i \sum_j d_{ij} \tau_i \otimes \tau_j. \tag{3.34}$$

Here, τ_0 is the identity matrix, and τ_n are the generalized Gell-Mann matrices. An example of a 4-dimensional QST measurement is shown in **Figure** 3.7

3.4.2 Extracting information from QST measurements

The desired quantum state can now be constructed successfully, leading to the question of can one characterize the quality and purity of this state? These questions can be answered by calculating three widely known measures, fidelity, linear entropy, and the concurrence [94, 18].

The fidelity was introduced all the way back in Chapter 1 (Eq. (1.68)). It is redefined here, this time in terms of the guessed density matrix (ρ_g), and the unknown density matrix of the target state ρ_{exp} [23],

$$F = \left(Tr \left[\sqrt{\sqrt{\rho_{exp}} \rho_g \sqrt{\rho_{exp}}} \right] \right)^2. \tag{3.35}$$

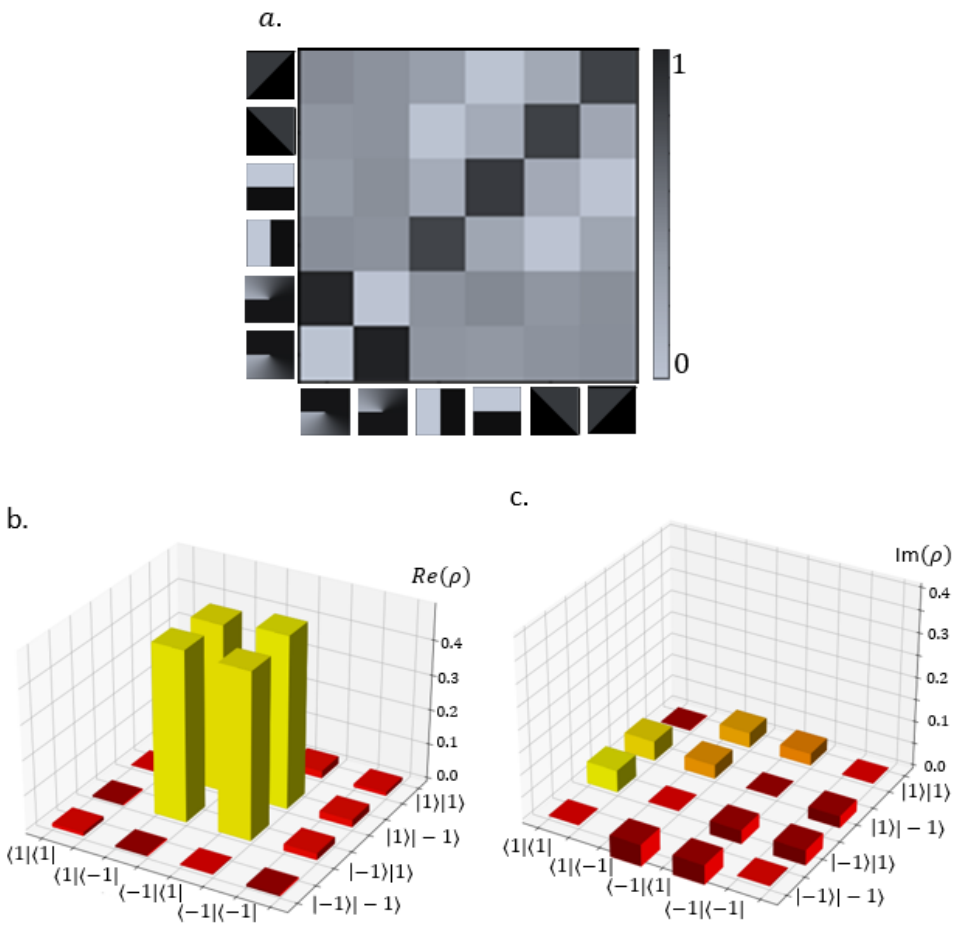


Figure 3.6: Two-Dimensional QST: This shows the full tomography measurement of the coincidence counts of an entangled two-photon system, projected into the measurement states corresponding to the given phase maps ($a.$), as well as the real ($b.$), and imaginary ($c.$) components of the density matrix.

Just as before, a value of $F = 1$ implies complete similarity between the two density matrices, and $F = 0$ implies none whatsoever.

The next relevant measure is that of the linear entropy, which is closely related to the purity (P) of the system. Reviewing Eq. (1.60),

$$S_{lin}(\rho) = 2(1 - Tr(\rho^2)), \tag{3.36}$$

and by recalling that the purity $P = Tr[\rho^2]$, one can classify the mixedness in the system. For a pure state, the purity $P = 1$ such that the linear entropy is 0, indicating no mixedness in the system, which intuitively makes sense.

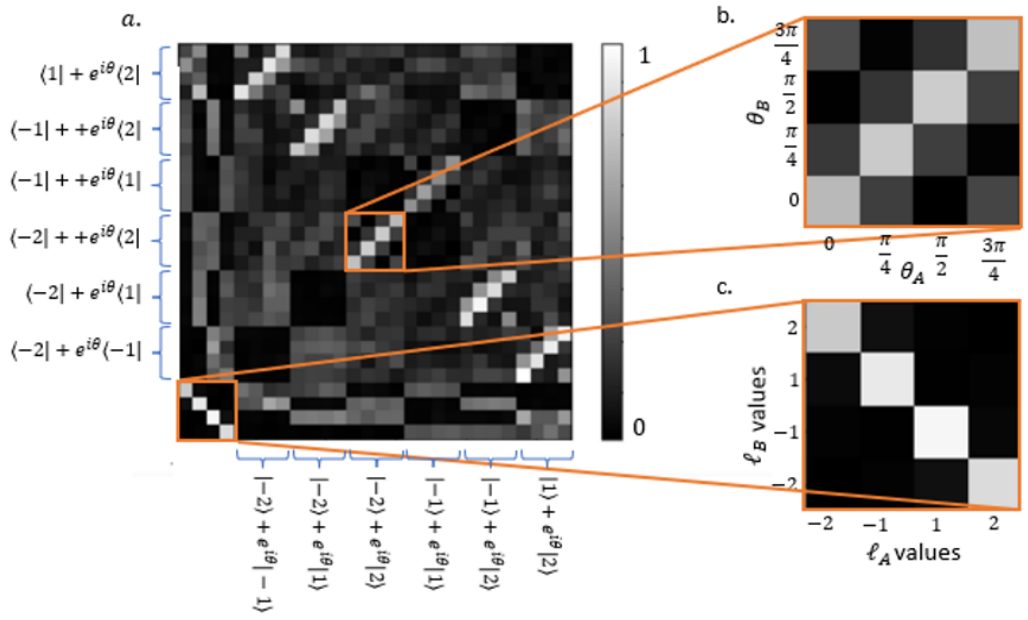


Figure 3.7: 4-dimensional QST: This shows the complete QST measurement ($a.$) for a four-dimensional ($\ell = \{-2, -1, 1, 2\}$) case of a two-photon entangled system. The block in ($c.$) represents the four pure states (The bras and kets are omitted for notational simplicity). Each mini block indicates the normalized coincidence counts for the corresponding states. The block in ($b.$) shows how the QST measurement can be read, in terms of the superposition of two states. The equations in ($a.$) display the superposition OAM states that correspond to each curly bracket.

.

The final measure is that of concurrence which was also introduced in the first chapter (see 1.10.1). A concurrence of $C = 0$ represents a quantum system that possesses no entanglement, whereas on the other end of the spectrum, $C = 1$ describes a system of maximal entanglement. A bipartite system that is larger than a pair of qubits (qutrits and so on) has no general formula to calculate the concurrence for the system.

3.5 Chapter conclusion

Entangled photons make for a very popular research interest, and the process used to generate these entangled photons has been extensively investigated. During an optical experiment related to entangled photons, there is often exposure to external sources of light, which can affect the quantum setup in a very negative way. It is therefore a necessity to ensure the photons are indeed entangled through the testing of the violation of the Bell inequality. One can also generate the entanglement spectrum for these photons, and reconstruct the entangled biphoton state through a quantum state tomography measurement. These quantum measurements are experimentally realized in the next chapter, where a relevant optical setup to perform these measurements, is also discussed.

Chapter 4

Building a quantum optical setup

4.1 Physics of building the setup

The optical setup that was employed to make the quantum measurements introduced in the previous chapter is shown in **Figure** 4.1. This was so chosen to allow for the generation of entangled photons, and the deliverance of these photons to the detection system. Doing this allowed for the measurements to be made on the quantum system.

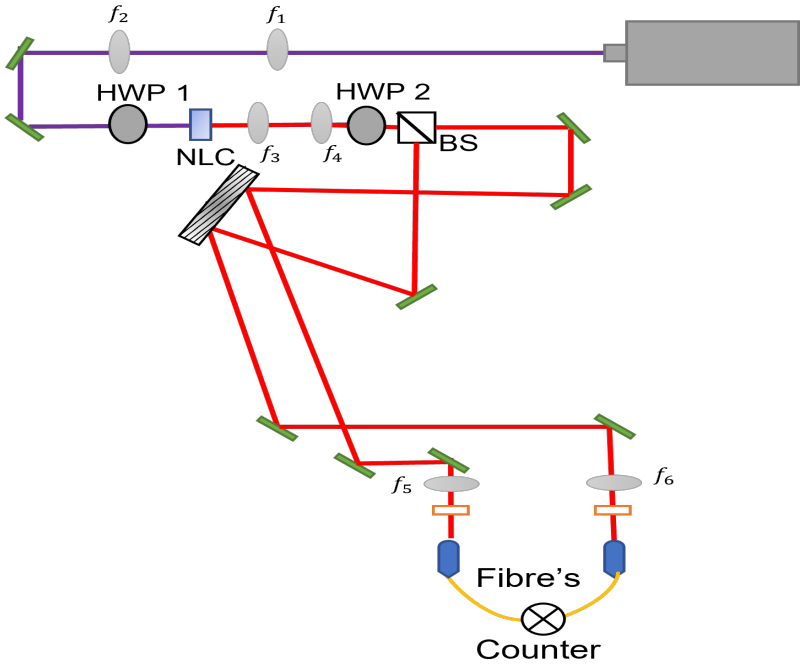


Figure 4.1: Experimental setup: The labels f_i refer to the lenses used in the setup. They are set up in pairs of two to work as a telescope imaging system. HWP 1 and 2 refer to the half wave plates before the crystal and SLM respectively. NLC is the non-linear crystal which in this case was a PPKTP crystal. BS is the beam splitter, and the two orange boxes before the fibres and fibre couplers are the 810nm bandpass filters which allow only photons with that wavelength to pass through.

The entangled photons were generated, in our case, through the process of SPDC where the pump beam sourced from a $405nm$ laser, and impinged on a PPKTP crystal which produced two lower frequency entangled photons of wavelength $810nm$. For measurement purposes, the overlap integral (Eq. (3.16)) had to be evaluated, which gave us the complex probability coefficient corresponding to a mode combination of the entangled photons. The overlap integral was evaluated at the site of the entangled photon generation, which occurred on the plane of the crystal. These entangled photons (which are a quantum phenomenon) were assumed to be in a superposition of all states until a measurement was made. Depending on the signal and idler states, the distribution of the coefficient values were found. This evaluation of the coefficients was experimentally realized by determining the coincidence counts in the detection system, by imaging (using a telescope) the plane at the crystal to the fibre coupler.

The fibres that were used to transport the photons from the setup to the detectors were single mode fibres. These fibres are designed to only permit Gaussian modes to be coupled into them. A question arises though, how do the states of these entangled photons, described initially by a superposition of states, become Gaussian? The answer lies in the reciprocity of light. If an incoming Gaussian mode passes through a hologram, an OAM mode would arise, if instead this OAM mode were to be the incoming mode that passes through the SLM, with the conjugate of its phase encoded, a Gaussian mode would now be the result, this is the reciprocity of light (see **Figure** 4.2).

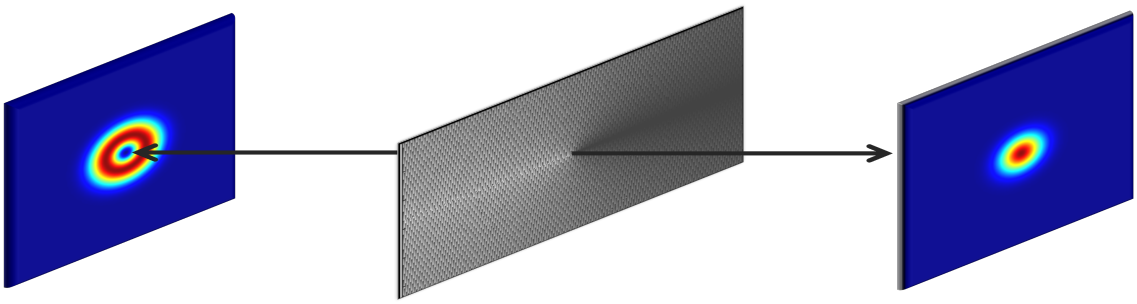


Figure 4.2: Reciprocity of light: Passing a Gaussian through a hologram would result in a particular desired mode. When reversing the procedure, and passing this mode through the hologram with the conjugate phase of the current mode encoded on it, the returned mode would then be a Gaussian again.

The LG basis is an orthonormal basis, which means that

$$\langle \ell_m | \ell_n \rangle = \begin{cases} 1 \text{ if } m = n \\ 0 \text{ if } m \neq n \end{cases}. \tag{4.1}$$

If one encodes the signal arm SLM with the conjugate phase of an $\ell = 1$ mode, only a Gaussian mode would result. This is true too for the idler arm, however since the signal and idler photons are entangled, in order to attain a Gaussian mode for the idler arm, one would have to correspondingly encode the conjugate of an $\ell = -1$ mode on the idler arm SLM. One can encode a hologram in any basis, so long as one stays consistent with the choice in both arms. This choice of

selecting the basis for measurement is known as post-selection and this process was used when we sought to couple the Gaussian modes into the fibres.

The Gaussian modes that came off of the SLMs were respectively imaged and coupled into the fibres simultaneously through the use of imaging systems, without the loss of information. These Gaussian modes were then imaged into photoelectric detectors known as Avalanche Photo Detectors. These devices generated a voltage response with every single photon detection.

Both arms were independently connected to a different APD, the voltage responses were then also generated independently of one another. Each arm thus had a separate display as to how many counts of photon detections were present. These voltage signals were then further transmitted to a counter (controlled by computer software such as LABView) which was responsible for deducing whether or not there was a delay between these respective counts, an example of such a device is the HydraHarp 400 which has a precision of $1ps$. This counter was programmed to detect all these voltages from both arms over a designated period of time, known as the integration (average detection) time. This controlled the accuracy of the detection, if one were to assign a longer integration time, more voltages, and hence photon detections, would occur, allowing for a more accurate deduction. Within this integration time, we also encoded a gating time, more easily understood as a coincidence window. If the voltages generated from the APD both got detected within this gating time, the signal was considered as a coincidence. These coincidence counts were a direct indication to the value of the complex probabilities that could be computed through the overlap integral. The fact that the conjugate phase has to be encoded on the SLMs to acquire a Gaussian mode for the detections to occur, matches the fact that complex conjugates of the signal and idler modes are present in the overlap integral.

There were also false, or accidental, coincidence counts that took place . This resulted from external sources of light that reached the detectors as well. Since these detections were unwanted and irrelevant, we sought to eliminate them. To quantize this amount of accidentals, the laser was simply turned off, leaving only the detectors on. The value of any counts and coincidences that were found was recorded. Having both the total coincidence counts, and these accidentals, allowed us to calculate the actual relevant coincidence counts. A useful ratio in quantum experiments is the quantum contrast, which is a measure of the ratio of the detected coincidences to the accidental ones. This presented as a useful tool to evaluate how acceptable the results in the quantum experiment were.

4.2 Possible practical limitations

Something that had to be kept in mind when building the optical setup was that the pump beam diameter had to be smaller than the size of the non-linear crystal, but not too small such that the intensity was high enough to burn the crystal. Finding this optimum beam size affected the choice of lenses used for the correct magnification. Moreover, different types and sizes of non-linear crystals would have had different lengths, and would have therefore led to different degrees of power loss that would not have been beneficial. A big drop in the efficiency would have affected the accuracy of the measurements.

The SLM had a fixed dimension, and so the beam size had to be further altered depending on what we wanted to do. The beam could not be magnified too small since it could have also burnt the SLM, and if we were to overfill the SLM, we would want to do so such that there was minimal loss of light. This meant that careful calculation was required to reduce the loss of efficiency as far as possible.

Another aspect that was considered was the range of optical modes that was used to make a measurement. Physically, the diameter of some modes were too big (compared to the dimensions of the detection system) that we could not detect any modes beyond them. So even though the theoretical range of detections was infinite, we were limited physically by the sizes of the optical components

4.3 Establishing control over the setup

There were some parameters of control, possible of refining the accuracy of the results in the setup, that was investigated in this experiment. Firstly, since we relied on the correct modulation of light through the use of SLMs, the correct calibration of the SLM was required. The concept of the gating and integration times have also been introduced, which if set incorrectly, would have invalidated the legitimacy of the coincidence measurements. The last parameter of control that was investigated was that of the temperature of the non-linear crystal, which affected the collinearity of the entangled photons, and therefore the coincidence counts.

4.3.1 Temperature:

There were two methods of testing for the optimal temperature for the crystal. This had to be done since the experiment was performed in a lab where the ambient temperature was not at room temperature. The first test was to investigate how the two entangled photon paths adapted as the temperature was altered. For this test, a Spiricon SP620u camera from Ophir was placed in the path of the beam after the non-linear crystal. The results are shown in **Figure** 4.3.

The second of these temperature tests was to alter the temperature and examine the effect on the coincidence counts and the quantum contrast. The results are shown in **Figure** 4.4. 6 measurement values were recorded for both the quantum contrast and coincidence count values at each temperature value. This set of 6 values was used to determine the standard deviation, and hence the standard error, for both the quantum contrast and the coincidence count values, which are shown in the figures as the error bars. In **Figure** 4.4 *a*. one can notice that the temperature variation resulted in a decline in the quantum contrast. This was most likely due to the fact that the temperature affected the collinearity of the down-converted photons, and thus the system may not have been aligned for the detection of these photons at various temperatures, resulting in the drop-off of the quantum contrast. In *b*. one can see a very strange dip in the coincidence values between the temperature range $54°C - 59°C$. This doesn't seem to make logical sense. What could have happened is that the ambient temperature of the room had altered due to the automatic air conditioning system installed. Nevertheless, the optimum temperature of $61°C$ was still consistent, as the coincidence counts were higher than previous temperatures. Once again, we

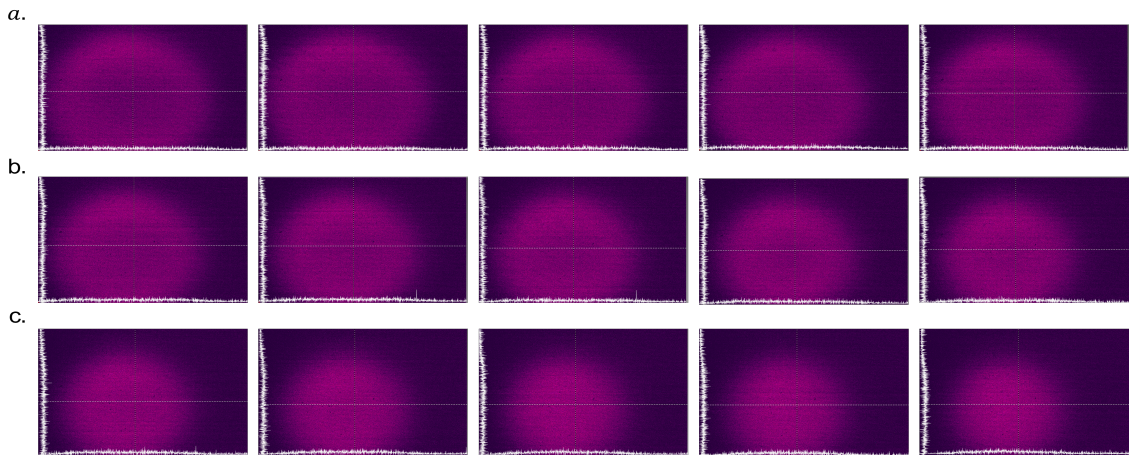


Figure 4.3: Crystal temperature: The evolution of the down-converted photons, in a room with an ambient temperature of $18°C$, is shown as the temperature is altered. *a*. represents temperatures from $49°C - 53°C$, *b*. from $54°C - 58°C$, and *c*. from $59°C - 63°C$. As the temperature increases, the trend noticed is that the region of light occupies a smaller region on the camera, this means that the two down-converted beams becomes more and more collinear. In our experiment, the optimal choice was when the temperature reached $61°C$. This was chosen because the physical profile of the light had a larger cross-sectional area at the chosen temperature, which allowed for more higher order modes to be detected.

did not optimize for maximum coincidence counts, as our range of detectable modes would have decreased if we chose a higher temperature.

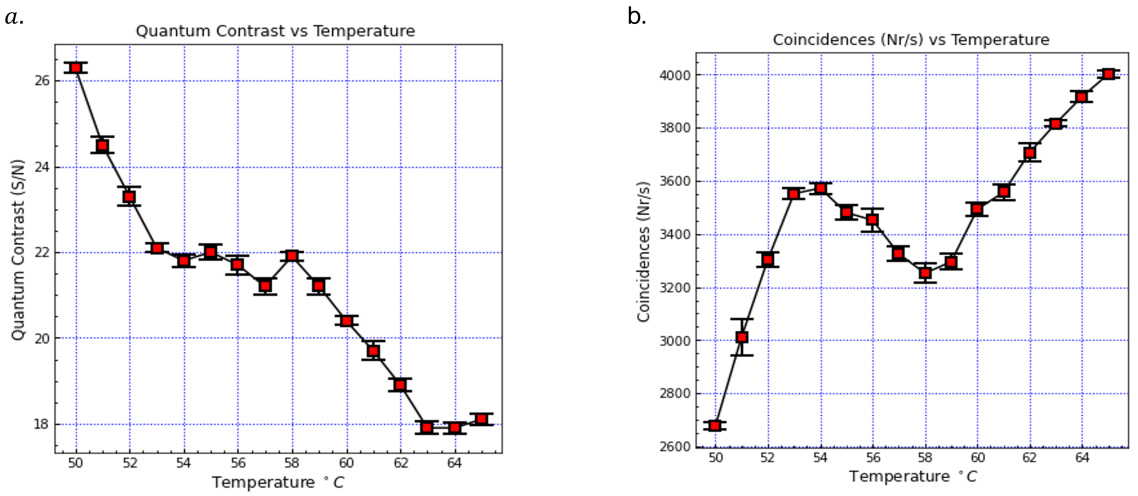


Figure 4.4: Temperature dependence: In *a*. the relationship between the quantum contrast and temperature is shown while in *b*. the relationship between the coincidence counts and temperature is shown.

The choice of optimal temperature was largely dependent on the purpose of the experiment which lead to a variation when compared to some literature values. Our temperature value of $61°C$ is comparative to the authors' with a result of $68°C$ in reference [95] where they had performed a similar optimal temperature investigation. On the other hand, when the experiment is performed

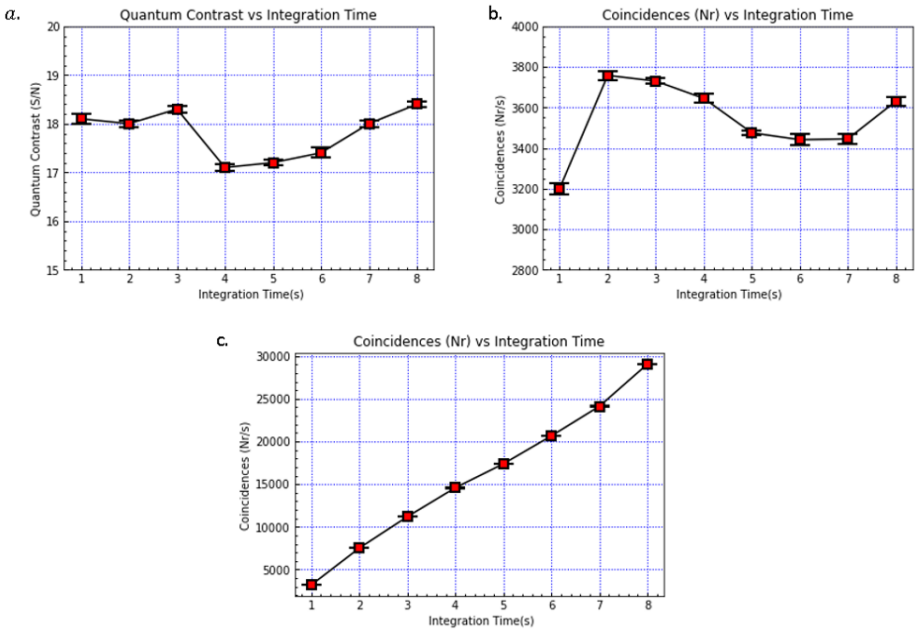


Figure 4.5: Integration time dependence: In *a*. the plot of the quantum contrast vs the integration time is shown. In *b*. the numbers of coincidences per second is plotted against the integration time. In *c*. a plot of the total coincidence counts as a function of the changing integration time can be seen.

for entirely different purposes as in reference [96] the temperature choice could be vastly different (around 28°C).

4.3.2 Integration Time:

The integration time is effectively the time window allocated to detecting photons. The longer the window, the more accurate the measurements since more coincidences can occur. The integration time was also altered to examine the effect on the quantum contrast and coincidence counts (see **Figure** 4.5). The error bars for this figure were generated similar to that of the temperature case, where also 6 values of the quantum contrast and coincidence counts were recorded for each integration time increment. In the Figure, one can notice that there is generally no variation in the plot shown in *a*. and *b*. , although in *b* there is an outlier that was probably caused by an accidental block of the beam. The reason that there is no real trend change in either of *a*. or *b*. is due to the fact that the gating time was kept constant, so the coincidences tally per second did not change, merely the total value of these coincidences measurements as seen in *c*.

4.3.3 Gating time:

The final parameter variation test performed was that of adjusting the gating time (coincidence window). To repeat the meaning of the gating time, it is a window within which simultaneous detection of two independent signals are seen as a coincidence. The results of this test of control

can be seen in **Figure** 4.6 where the error bars were again determined in the usual way with 6 values recorded for each data point. When the window within which coincidences were determined (gating time) was increased, some photons which were not necessarily entangled still got detected as if they were in coincidence. This is what caused the increasing coincidence per second trend in *b*. and by allowing many more accidental detections, the quantum contrast also dropped as seen in *a*..

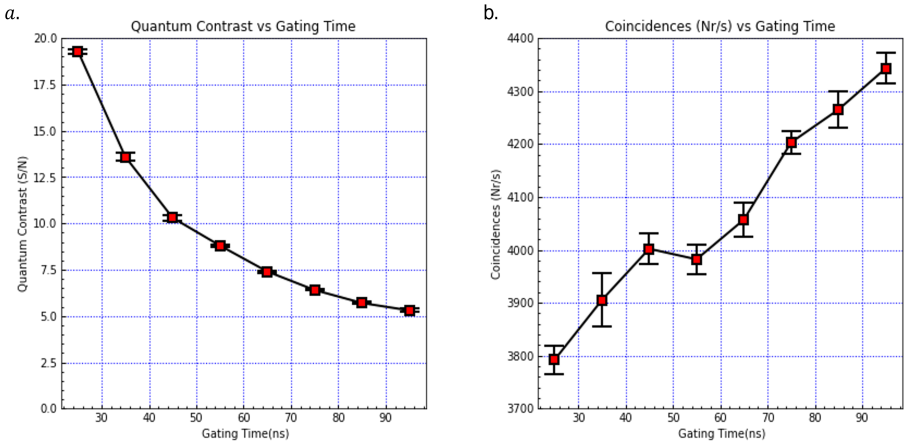


Figure 4.6: Gating time dependence: In *a*. a plot of the quantum contrast as a function of the gating time is shown, while *b*. shows the plot of the coincidences as a function of the gating time.

These parameters, should be correctly adjusted to have a quality experimental setup. By having these parameters wrongfully altered, one can run into a number of problems. One could get delayed with attempting to find a solution to the issue of low coincidences or low quantum contrast. One could also not even realize the problem has to do with parameters and be tempted to unnecessarily alter or fix the system.

4.4 Measurement results

The setup was optimized through repetitive alignment and we could finally move on to the gathering of our results. Throughout all these measurements, the control parameters were set to a fixed value. These were the temperature, which was chosen to be $61°C$, the integration time which was chosen to be $5s$, and the gating time which was kept at $30ns$. In each of these measurements, the accidental coincidence counts were filtered out, leaving only the actual relevant data required for the measurements. This was accomplished as follows:

By letting the total coincidence data be given by C_T, and the contrast be given as QC (coincidences over accidentals), the accidentals (A) could be determined by:

$$A = \frac{C_T}{QC}, \tag{4.2}$$

and to get the coincidence counts without the accidentals (C_{actual}), we could determine

$$C_{actual} = C_T - A. \tag{4.3}$$

These new coincidence counts were what was used in the analysis.

Spiral Bandwidths:

SLMs placed in the signal and idler arms were used to scan through OAM values in the range of $\ell = -5$ to $\ell = 5$ with the coincidence counts recorded in order to generate the spiral bandwidth measurements. Two intensity spectrums were generated for this range, a 'good' result where the measurement was taken in a dark room, and a 'bad' result where external light sources were purposefully introduced to examine the effect. These two results are shown in **Figure** 4.7 *a*. and *b*. The spiral bandwidth for the 'good' case is given in **Figure** 4.7 *c*.

An analytical procedure was performed to determine the degree of asymmetry in the spiral bandwidth from **Figure** 4.7 *c*. To do this, the corresponding intensity peaks on either side of the $\ell = 0$ peak (for instance at $\ell = 1$ and $\ell = -1$) was compared as a ratio and averaged over the whole range of ℓ values. This allowed for a computation of a value of symmetry between the left and right halves of the spectrum. This similarity value came out to be 0.98. The full-width at half-maximum (FWHM) for this spiral bandwidth was found to be $\Delta\ell = 7$ which meant that there were seven highly correlated modes detectable by the system.

At first sight, **Figure** 4.7 *a*. seemed like a relatively perfect intensity spectrum, but by examining the spiral spectrum plot of the diagonal elements given in *c*. it was deduced that there was actually an asymmetry present in the spiral spectrum. Moreover, there were many off-diagonal cross-terms present which were unwanted. This meant that even though the measurement was made in a dark room, there was still external light sources present contributing to the unwanted noise. It was clear by looking at **Figure** *b*. that there were many off-diagonal elements present when external light sources were intentionally introduced.

There were a few more comparative analytical techniques that were put to use here to determine some relevant information about the quantum system. We have already discussed the asymmetry comparison between mirroring halves about the central peak of the spiral bandwidth. Some other methods include determining the contribution of the accidentals to the total coincidence counts and plotting and determining if there are any cross-talk elements present, other than the desired diagonal elements in the OAM intensity spectrum. To identify the contribution of the accidentals, and to truly appreciate the power of removing the accidentals from the data, the unfiltered coincidence data was compared with the coincidence data that had no accidentals included, It was therefore also possible to deduce the spectrum of solely the accidentals as well. Doing this demonstrated the contribution of external sources, and showed how careful one has to be during a quantum experiment, to eliminate any unwanted errors, (see **Figure** 4.8).

Usually, when looking at the spiral spectrum, the diagonal elements of the OAM intensity spectrum is plotted as a 2D plot. Instead, the vertical, or horizontal, cross-section of this OAM intensity spectrum was examined. This gave us the power to determine whether there was cross-talk in the system or not. In a perfect scenario where only the diagonal elements were present, with no

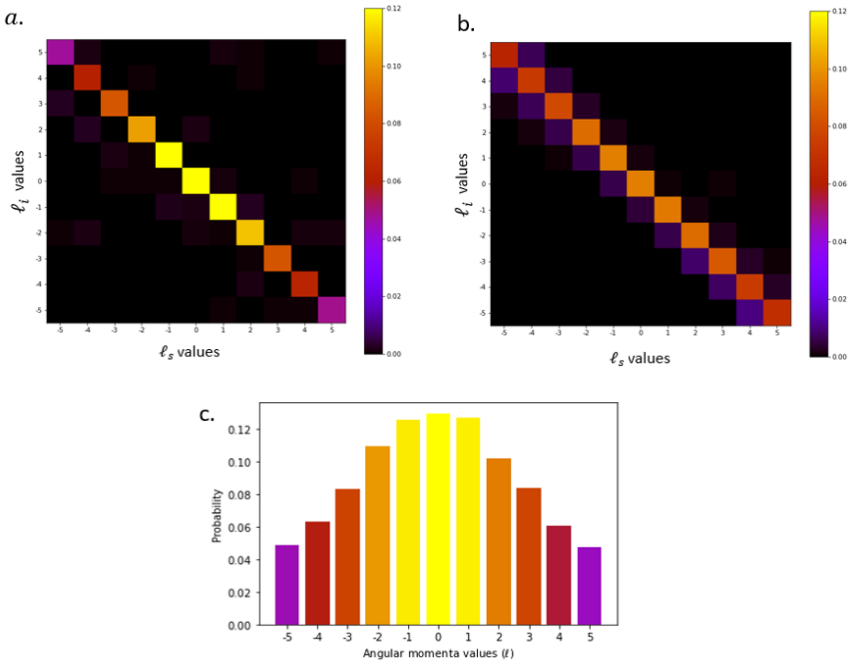


Figure 4.7: Spiral bandwidth for $\ell = \{-5, 5\}$: *a*. displays the OAM intensity spectrum when the measurement is made in a completely dark room. In *b*. one can see an OAM intensity spectrum where external light sources have been introduced. The spiral bandwidth for the 'good' case (shown in *a*.) is shown in *c*.

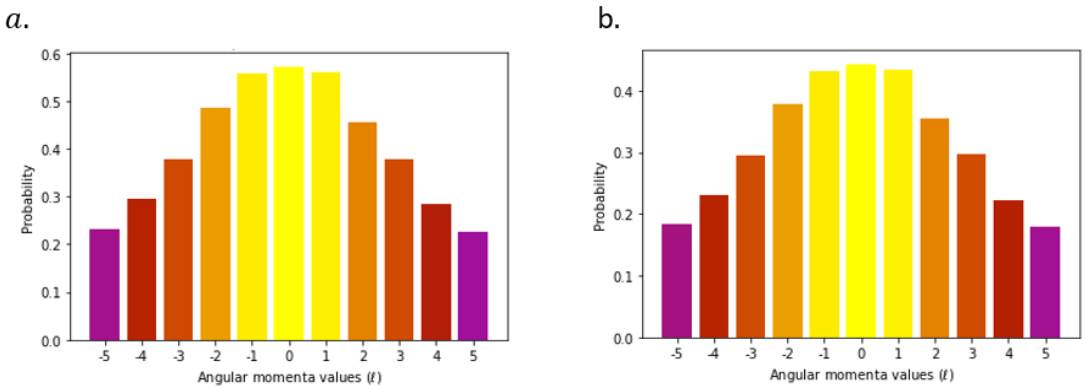


Figure 4.8: Accidental component of the coincidence counts: *a*. gives an indication of the spiral bandwidth with the accidentals not being removed from the data. *b*. shows what the spectrum of only the accidental coincidences looks like. Clearly the contribution of the accidentals cannot be noticed by simply examining the spectrum from **Figure** 4.7 *c*. One has to explicitly aim to notice this contribution which could potentially result in a large error if this is not accounted for.

cross-talk, inspecting these cross-sections would only yield a peak at the desired values, with all other peaks at 0. There is usually always cross talk peaks in experiments as one can never produce a completely perfect spiral bandwidth, one would strive to simply create as perfect a spectrum, with as little cross talk as possible. **Figure** 4.9 shows two cross-sections taken for this spectrum.

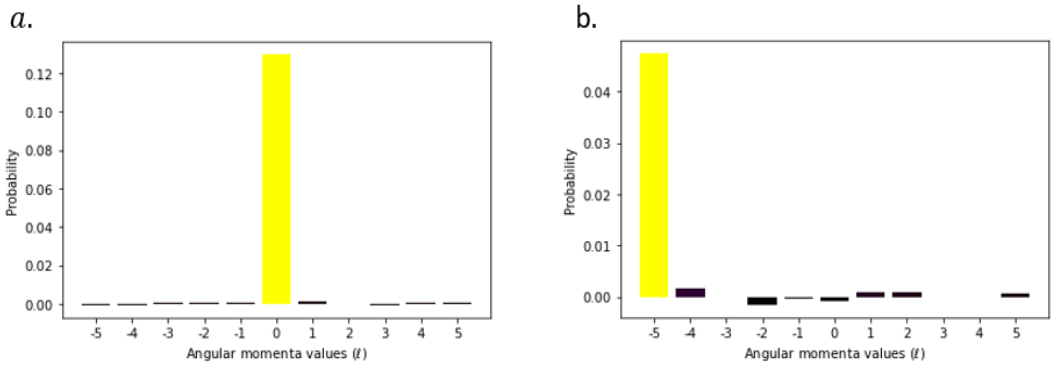


Figure 4.9: Cross-sections of the $\ell = \{-5, 5\}$ spectrum: The cross-section in a. shows the well defined peak at $\ell_s = 0$, where the cross-section has also been created by looking at the elements corresponding to $\ell_i = 0$. It can be seen that most elements, other than the peak, is near but not precisely at 0. The same trend can be seen in b. only this time with the defined peak at $\ell_s = -5$ for the cross-section about $\ell_i = 5$.

Spiral bandwidths, OAM intensity spectrums, and the analysis thereof, for the OAM ranges of $\ell = \{-15, 15\}$ and $\ell = \{-25, 25\}$ were also performed, and in each of these cases, a similar survey on the quality of these bandwidths was done. The results are shown in **Figure** 4.10 and **Figure** 4.11 respectively.

By analyzing the results for the spiral bandwidth analysis for $\ell = \{-15, 15\}$ shown in **Figure** 4.10 the familiar well defined diagonal of intensities on the density plot in a. was noticed. The presence of the undesired off-diagonal elements present in a. was also noticed. The corresponding spiral spectrum shown in b. also did not feature the desired equal intensities for equal $|\ell|$ values, this meant that the similarity comparison was once again repeated and resulted in a value 0.95 between mirroring halves of the spectrum. By taking the cross-section of the spiral spectrum about $\ell_i = -10$ (resulting in the peak at $\ell_s = 10$ as seen in f.) it was clear that there were a lot of unwanted peaks across the spectrum, reiterating the issue of the cross-talk elements in the intensity spectrum.

By examining the results for the spiral bandwidth analysis for $\ell = \{-25, 25\}$ shown in **Figure** 4.11 it was clear that despite the well-defined diagonal of intensities, there were again off-diagonals (see a.) hence causing us to make cross-sectional analyses about $\ell_i = 0$ (see e.) and about $\ell_i = 10$ (see f.). In the latter cross-sectional analysis, the presence of the off-diagonals could be seen explicitly. It was clear by looking at b. that the mirroring halves were again not symmetrical, thus causing a similarity comparison to be performed which yielded a similarity of 0.8 which was very poor.

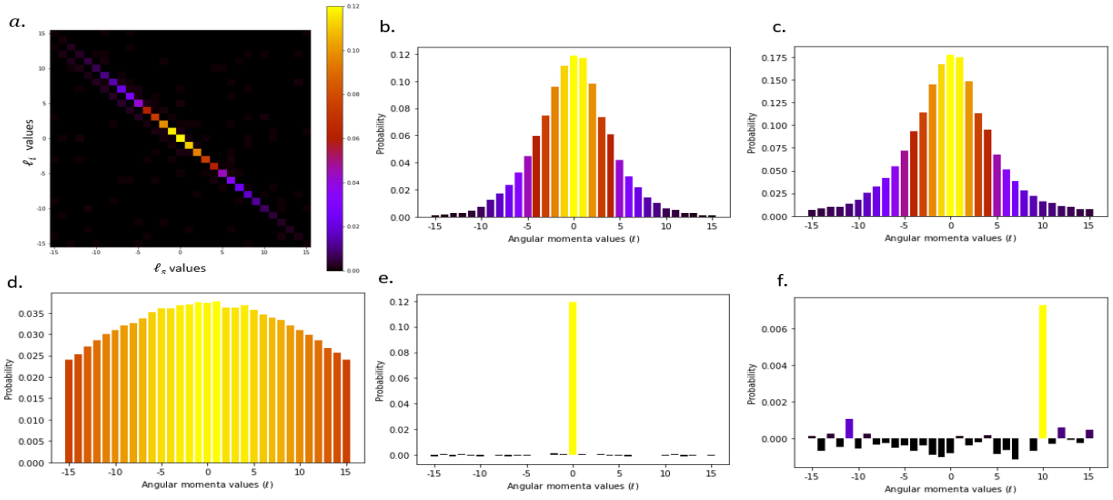


Figure 4.10: Spiral bandwidth analysis for $\ell = \{-15, 15\}$: *a.* is once again the OAM intensity spectrum and *b.* is the corresponding spiral spectrum for the entangled photons. *c.* shows the spectrum when the accidentals are included in the data set and *d.* is the spectrum showing the contribution of only the accidentals. Cross-sections of the spiral bandwidths about $\ell_i = 0$ and $\ell_i = -10$ is shown in *e.* and *f.* respectively.

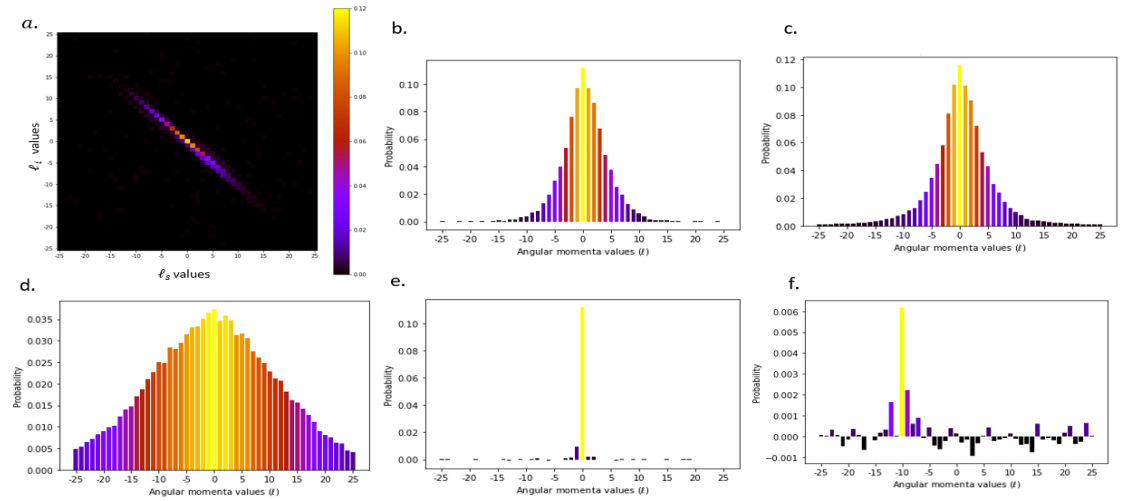


Figure 4.11: Spiral bandwidth analysis for $\ell = \{-25, 25\}$: The OAM intensity spectrum is presented in *a.* while *b.* shows the corresponding spiral spectrum. In *c.* and *d.* one can see the spiral spectrum of the total coincidences and accidentals respectively. The spectrum of the cross-section about $\ell_i = 0$ is shown in *e.*, and about $\ell_i = 10$, whose corresponding highest peak is at $\ell_s = -10$, is shown in *f.*

Bell Measurement:

To test whether the quantum setup indeed generated a pair of entangled down-converted photons, it was paramount to perform a Bell measurement and test for the violation of the CHSH inequality. This was done for two cases, in the $|\ell| = 1$ subspace (see **Figure** 4.12 *a.*), and in the $|\ell| = 2$ subspace (see **Figure** 4.12 *b.*). A Bell parameter was of course determined for each case,

by use of Eq. (3.24). In the $|\ell| = 1$ subspace the Bell parameter yielded a result of $S = 2.76 \pm 0.05$, which violated the CHSH inequality by 12 standard deviations ($SD = 0.0625$), and for the $|\ell| = 2$ subspace it was $S = 2.57 \pm 0.04$, which confirmed the violation of the CHSH inequality by 23 standard deviations ($SD = 0.025$). This verified that the two photons were indeed entangled with one another. There is a clear discrepancy between these two values which is possibly due to misalignment of the non-linear crystal when realigning and optimizing the setup for the two measurements.

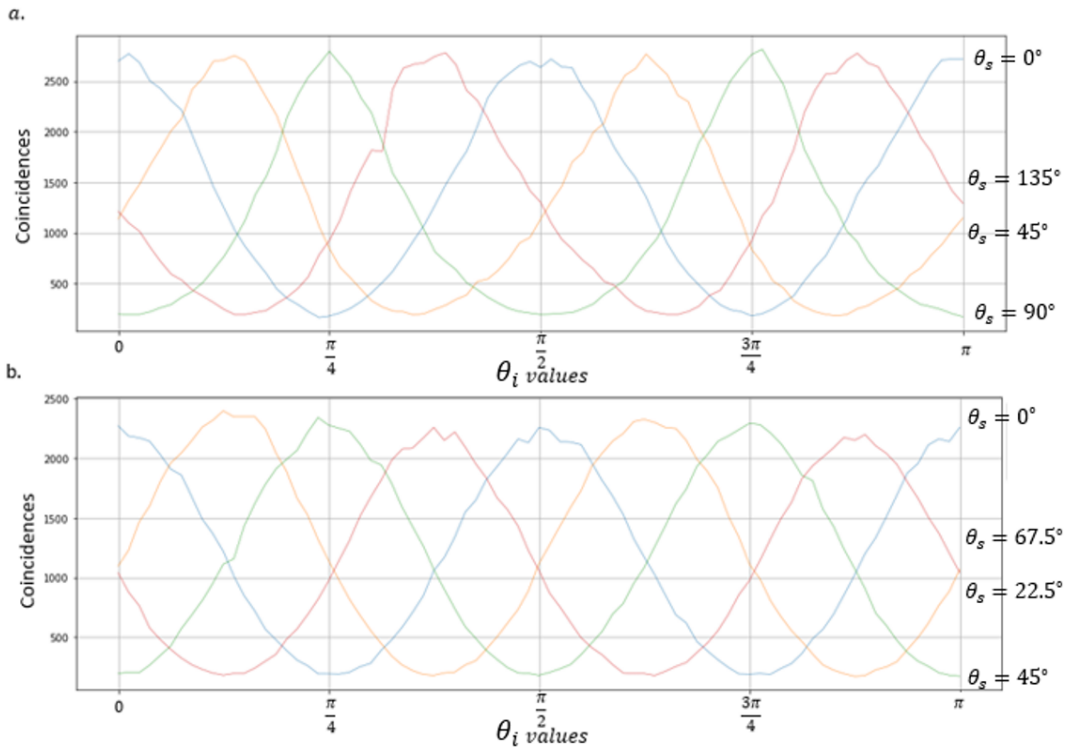


Figure 4.12: Bell measurements using the CHSH inequality: These results show the normalized coincidence counts plotted as a function of the θ_i values while keeping the θ_s values constant as shown in the legends. This is done for the $|\ell| = 1$ subspace in a. and the $|\ell| = 2$ subspace in b.

Quantum State Tomography measurements:

Once the violation of the CHSH inequality was confirmed for both the $|\ell| = 1$ and $|\ell| = 2$ subspaces, we endeavoured to reconstruct the density matrices for different dimensions. What follows are a series of figures corresponding to the QST measurements that was taken, and the reconstructed real and imaginary density matrices for a 2D system with basis states $\ell = 10$ and $\ell = -10$ (**Figure** 4.13), a 3D system with basis states $\ell = \{-1, 0, 1\}$ (**Figure** 4.14), and a 4D system with basis states $\ell = \{-2, -1, 1, 2\}$ (**Figure** 4.15). This was accomplished by performing the maximum likelihood estimation using the Chi-squared quantity in Eq. (3.33). The fidelity and entropy measures for each case was evaluated, as well as the concurrence for the 2-dimensional QST measurement, and the results are discussed below.

For the 2D QST measurement (**Figure** 4.13) the linear entropy was determined to be $L = 0.08 \pm 0.01$, the fidelity was found to be $F = 0.93 \pm 0.01$, and the concurrence was $C = 0.87 \pm 0.03$. Since the concurrence was close to 1 it was confirmed that the state was indeed entangled, and based on the measurement of the fidelity also nearing a value of 1, it was concluded that this state resembled a near-maximally entangled state.

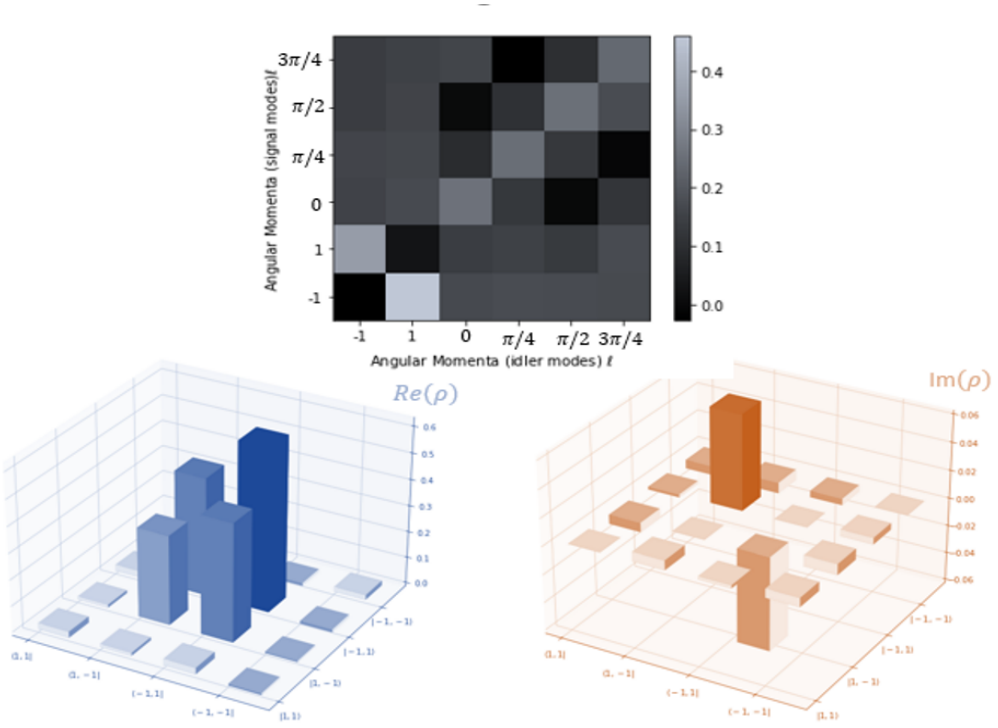


Figure 4.13: 2D QST: This figure shows a QST measurement, as well as the reconstructed real and imaginary density matrices for the basis states $\ell = 1$ and $\ell = -1$. The blocks with labels 0, $\frac{\pi}{4}$, $\frac{\pi}{2}$, and $\frac{3\pi}{4}$ correspond to the phase difference between the superposition states (blocks with 1 and -1).

For the 3D QST measurement (**Figure** 4.14), the linear entropy was calculated as $L = 0.14 \pm 0.01$, and the fidelity was $F = 0.90 \pm 0.02$. This higher dimensional case clearly had a decrease in the fidelity, but still had a value close to 1 which indicated its state was near maximally mixed. The linear entropy also climbed implying that the state was not completely pure.

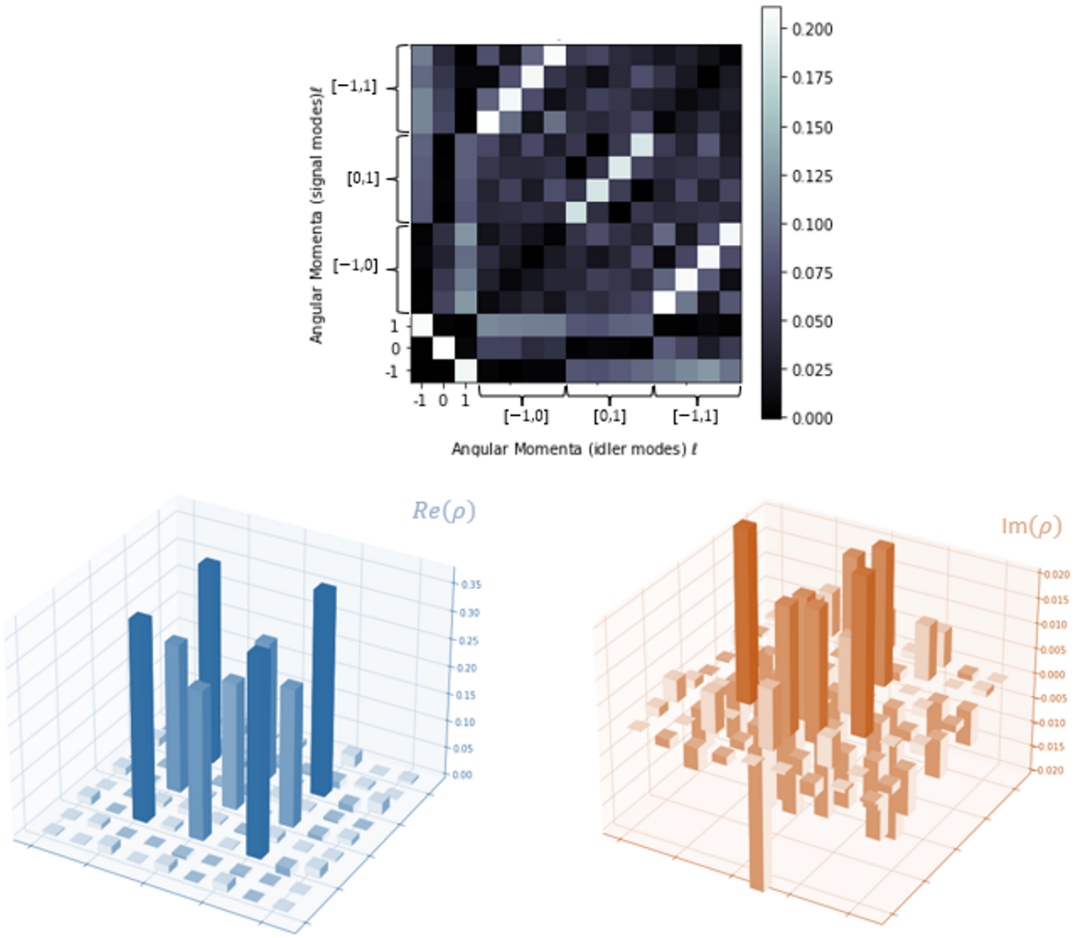


Figure 4.14: 3D QST: A 3D QST measurement is displayed with its corresponding density matrices. The labels denoted with square brackets show which OAM states are superpositioned with one another.

In the case of the 4D QST measurement (**Figure** 4.15), the linear entropy was determined to be $L = 0.26 \pm 0.05$ while the fidelity was $F = 0.85 \pm 0.01$. There was a clear dip in the fidelity which meant that the reconstructed state was moving away from a maximally entangled one. Moreover, the trend also appeared to reconstruct a less pure state with a higher-dimensional QST measurement.

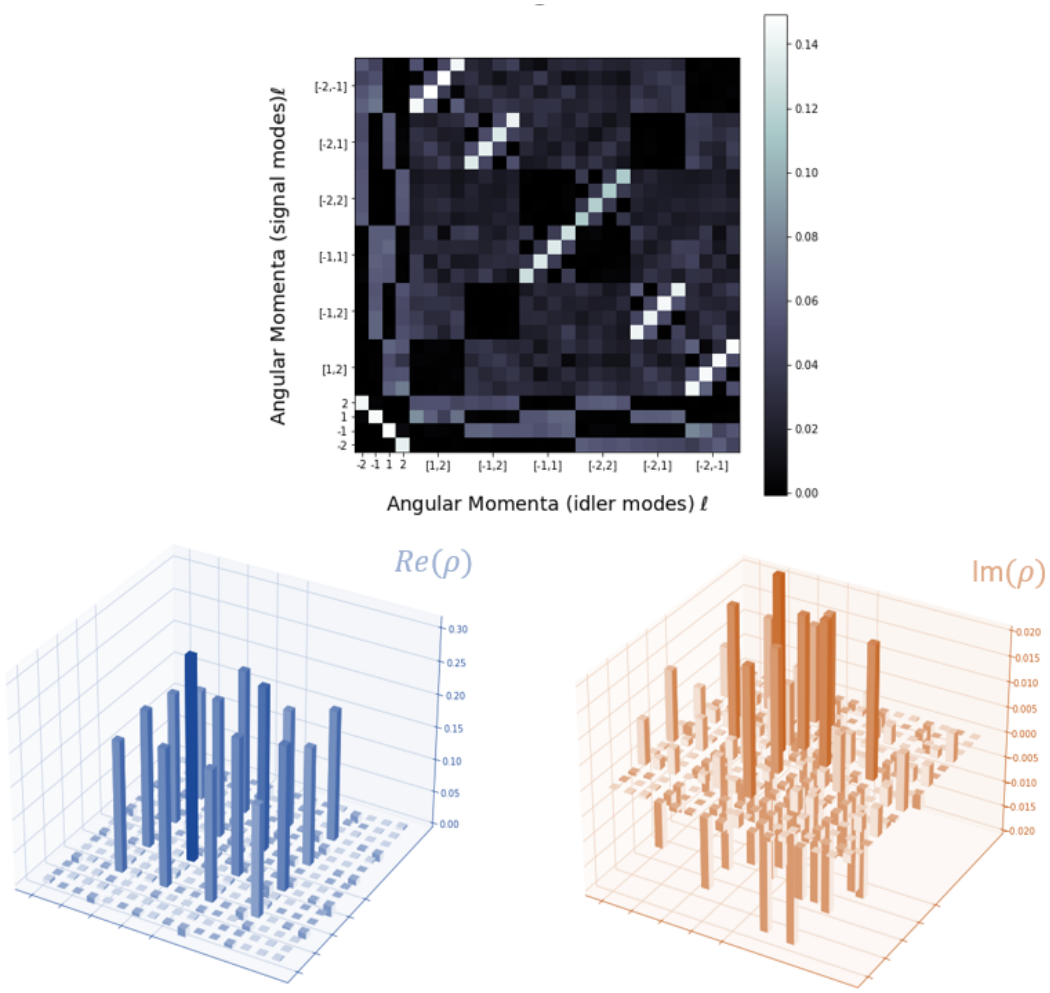


Figure 4.15: 4D QST: A 4D QST and its density matrices are shown here.

It can be easily concluded that with an increase in the dimension of the QST measurement, the Fidelity lowered and the linear entropy increased. Thus the system became less pure with a higher dimension, while at the same time the similarity between the experimental and reconstructed density matrices decreased.

4.5 Chapter conclusion

This chapter solidifies the understanding, interpretation, and use of the quantum measurements related to photon entanglement. The quantum measurements that were investigated include a spiral bandwidth analysis, a Bell measurement which allowed for the verification of entanglement within a quantum system, and quantum state reconstruction for different dimensions through a quantum state tomography measurement. It was noticed that with a higher dimension comes a loss in the purity and fidelity of a reconstructed state. This chapter also demonstrated the control over an optical setup that has to be established, in order to have a proper functioning quantum

setup. What usually proves a useful task, is to change the pump beam from a Gaussian beam, to a more creative spatial profile, in the hopes to achieve a desired entanglement spectrum for the purpose of increasing the dimension of entanglement. This is addressed in the next chapter.

Chapter 5

Pump Shaping and Entanglement Control

Since their realization and discovery, entangled photons have been extensively used in the development and research of several quantum technologies, such as in quantum computation [97, 98], quantum communication [47, 48], and quantum cryptography [46, 99] protocols. There has been a recent surge in the endeavour to move towards high-dimensional entangled states for the benefit of more information capacity, and robustness to a noisy environment. As mentioned throughout this dissertation, there are many aspects influencing the entangled state, such as the phase matching conditions, magnification of the beam, and the type of non-linear crystal used, but ultimately what remains of interest is that of the spiral (modal) spectrum of the entangled biphoton state. As it currently stands (with a Gaussian pump beam), each photon can attain a particular state so long as it obeys the OAM conservation relation, $\ell_s = -\ell_i$. Furthermore, this is only the case for a set of two states with the same probability ($|\ell| = 1$ has a higher probability than $|\ell| = 2$). To get access to a higher dimensional state, this restriction of strictly two states having the same probability has to be lifted. It is therefore useful to develop some form of control over the modal spectrum.

The modal spectrum is, by definition, determined through the overlap integral of the pump beam's transverse mode (Gaussian in the usual situation) and that of the two down-converted entangled photons. This leaves room for two natural methods of controlling the modal spectrum. The first is through an exercise of post-selection. This is performed by altering in which basis a measurement is made (by changing the hologram on the SLMs before the detector), which changes the efficiency of each measurement, examples include flattening the spectrum [100] and concentrating the entanglement [101]. This, however, is not a method of actually engineering a state. The alternative method, which is that of interest, is to shape the input pump beams transverse profile, this is known as pump shaping. This approach was firstly seen in the pioneering work on OAM entanglement [102] where the conservation of OAM was confirmed down to the single photon level by using different pump beams (an SLM shaping the pump beam therefore has to be included in the optical setup). There have been numerous studies since then relating the spiral spectrum of down-converted entangled photons from a non-linear crystal pumped by a conventional Gaussian [103], Ince-Gaussian [52], Laguerre-Gaussian [104], Hermite-Gaussian

[105], Bessel-Gaussian [106], and vector vortex beams [107]. In the OAM basis with an LG defined pump beam, the coefficients of the spiral spectrum can be analytically determined as shown in [63], and by generating a pump beam from a superposition of LG modes, a pump with phase singularities embedded inside the wavefront has also been realized [108, 109]. Combining many of these modes in superposition, or any in creative way, allows for a multitude of exotic pump modes to be generated.

These studies provided a stepping stone in the direction of gaining full control over a modal spectrum. They are aimed at designating a pump mode, and investigating the effect on the spectrum. The reverse is a bit more tricky, stipulating the desired modal spectrum, and attempting to calculate the pump beam that would yield such a spectrum. This has been previously addressed theoretically in the OAM subspace through a guess-and-optimize approach where the initial pump beam is chosen, through an educative guess, and altered by optimizing under a simultaneous perturbation stochastic approximation (SPSA) technique [110]. Though useful, it creates undesired noise resulting in only an approximate solution to the problem at hand.

We provide an alternative solution to this, in a basis-independent tensor procedure whereby the problem is inverted, allowing one to determine the analytical solutions for the pump beam, based on the desired modal spectrum.

5.1 Theory and mathematics

Consistent to this project, the shaping of light occurs through the employment of SLMs, although there are many other techniques that can be used.

A monochromatic pump beam is assumed, and a thin-crystal limit is considered to simplify the mathematics involved. This is experimentally equivalent to an experimental quantum setup for collinear down-conversion, where the phase matching condition can be set to unity in the overlap integral (by the thin crystal limit). This entangled state can therefore be completely determined by the pump profile ϕ such as in Eq. (5.1), which is reiterated here as:

$$|\psi\rangle = \int_s \int_i d\mathbf{k}_s d\mathbf{k}_i \phi(\mathbf{k}_s, \mathbf{k}_i) \hat{a}^\dagger(\mathbf{k}_s) \hat{a}^\dagger(\mathbf{k}_i) |0, 0\rangle. \tag{5.1}$$

The state of the pump and down-converted photons can be expressed in any basis in the set of solutions to the paraxial Helmholtz equation. The Hilbert space, of the solutions to this Helmholtz equation, is separable which means that there are countable bases (indexed by countable sets such as integers) in which the states of these photons can be described. Denote such a countable arbitrary basis as $\mathbb{B}$, that is defined by a set of mode functions (LG, BG etc) given by $\{F_{\bar{j}}\}$ where $\bar{j}$ itself is a multi-index related to a specific basis function from that set. For instance, if one were to work in the LG basis, $\bar{j} = \{\ell, p\}$, and if one were in the HG basis, $\bar{j} = \{m, n\}$.

This means that in such a basis $\mathbb{B}$, the SPDC state becomes

$$|\Psi_{SPDC}\rangle = \sum_{\bar{s},\bar{i}} C_{\bar{s},\bar{i}} |\bar{s}\rangle_s |\bar{i}\rangle_i, \tag{5.2}$$

with $|\bar{s}\rangle_s$ and $|\bar{i}\rangle_i$ as the eigenstates for the signal and idler modes in our basis:

$$\begin{aligned} |\bar{s}\rangle_s &= \int_s d\mathbf{k}_s F_{\bar{s}}\, \hat{a}^\dagger(\mathbf{k}_s)|0\rangle, \\ |\bar{i}\rangle_i &= \int_i d\mathbf{k}_i F_{\bar{i}}\, \hat{a}^\dagger(\mathbf{k}_i)|0\rangle. \end{aligned} \tag{5.3}$$

The $C_{\bar{s},\bar{i}}$ terms are the joint complex probability amplitudes of finding the signal and idler photons in their respective eigenstates, and are related to the pump profile through:

$$C_{\bar{s},\bar{i}} = \langle \bar{s}|_s \langle \bar{i}|_i \Psi_{SPDC}\rangle = N \int d\mathbf{k}_s d\mathbf{k}_i \phi F_{\bar{s}}^* F_{\bar{i}}^*, \tag{5.4}$$

with N as a normalization coefficient enforcing the normalization condition of $\sum_{\bar{s},\bar{i}} |C_{\bar{s},\bar{i}}|^2 = 1$. The parameters related to the beam waists are controlled by means of the optical components and therefore play no role. This Eq. (5.4) is that which we are tasked to invert, which will permit us to calculate the requisite pump profile for a desired spectrum.

To do this, one firstly starts off by expressing the pump profile in terms of the basis $\mathbb{B}$, this can be done since the pump profile should also be a solution to the Helmholtz equation. Therefore,

$$\phi(\mathbf{k}_s, \mathbf{k}_i) = \sum_{\bar{p}} \chi_{\bar{p}} F_{\bar{p}}. \tag{5.5}$$

The $\chi_{\bar{p}}$ term represents the set of coefficients which can allow for the determination of the pump profile. These coefficients can be beautifully extracted from the multi-linear system of equations:

$$C_{\bar{s},\bar{i}} = \sum_{\bar{p}} \chi_{\bar{p}} N \int d\mathbf{k}_s d\mathbf{k}_i F_{\bar{p}} F_{\bar{s}}^* F_{\bar{i}}^*, \tag{5.6}$$

which can be succinctly written in a more convenient form in terms of only tensors:

$$C_{\bar{s},\bar{i}} = \sum_{\bar{p}} \chi_{\bar{p}} A_{\bar{p},\bar{s},\bar{i}}, \tag{5.7}$$

with

$$A_{\bar{p},\bar{s},\bar{i}} = N \int d\mathbf{k}_s d\mathbf{k}_i F_{\bar{p}} F_{\bar{s}}^* F_{\bar{i}}^*. \tag{5.8}$$

The tensor $A_{\bar{p},\bar{s},\bar{i}}$ is completely determined by the choice of basis used, tensor $C_{\bar{s},\bar{i}}$ is the desired spectrum for the down-converted coefficient amplitudes, and the χ is what needs to be

determined. Regrettably, to invert Eq. (5.7) is not a simple task as the system is usually over-determined. A unique solution does not always exist since not every unknown variable can be determined. One can, however, use a minimization technique (similar to matrices) to attain the best solution to this inversion.

The minimization procedure is performed by use of the Frobenius norm,

$$\Phi(\chi) = \sum_{\bar{s},\bar{i}} |C_{\bar{s},\bar{i}} - \sum_{\bar{p}} \chi_{\bar{p}} A_{\bar{p},\bar{s},\bar{i}}|^2. \tag{5.9}$$

This norm is the sum of the squared-norm of the difference between the desired spectrum $C_{\bar{s},\bar{i}}$ and the spectrum obtained experimentally. Since the terms in Φ are subsequently quadratic, there has to exist a critical point ($\frac{\partial}{\partial\chi}\Phi(\chi)|_{\chi=\chi'} = 0$) represented by $\chi' = min_\chi(\Phi(\chi))$.

By solving $\frac{\partial}{\partial\chi}\Phi = 0$,this minimizer χ' must satisfy [64]

$$\sum_{\bar{s},\bar{i},\bar{p}_1} A^*_{\bar{s},\bar{i},\bar{p}} A_{\bar{s},\bar{i},\bar{p}_1} \bar{\chi}_{\bar{p}_1} = \sum_{\bar{s},\bar{i}} A^*_{\bar{s},\bar{i},\bar{p}} C_{\bar{s},\bar{i}}. \tag{5.10}$$

The required coefficients χ must exist and has to satisfy this new multi-linear system (Eq. (5.10)). Solving this system has to provide an optimal and unique solution for the pump profile. This χ solution presents the pump coefficient in the chosen basis, and minimizes the difference between the desired spectrum $C_{\bar{s},\bar{i}}$ and the experimentally-observed spectrum, which is denoted here as

$$B_{\bar{s},\bar{i}} = \sum_{\bar{p}} \chi_{\bar{p}} A_{\bar{p},\bar{s},\bar{i}}, \tag{5.11}$$

such that our SPDC state can be formulated as

$$|\Psi_{SPDC}\rangle = \sum_{\bar{s},\bar{i}} B_{\bar{s},\bar{i}} |\bar{s}\rangle_s |\bar{i}\rangle_i. \tag{5.12}$$

In the event that the inversion is perfectly solvable, it naturally follows that $C_{\bar{s},\bar{i}} = B_{\bar{s},\bar{i}}$ for all indices. This solution discussed here treats all terms and all indices on the same footing, which experimentally, is not always beneficial. Although this solution is more general, it might prove useful, to give one the power of selecting a subspace of this full Hilbert space since this is the case for most experiments, for example, only being concerned about the OAM subspace and ignoring the radial indices in LG modes.

To tailor pumps for these scenarios, a set of weighting factors is incorporated to create a weighted norm instead:

$$\Phi_w(\chi) = \sum_{\bar{s},\bar{i}} w^2_{\bar{s},\bar{i}} |C_{\bar{s},\bar{i}} - \sum_{\bar{p}} \chi_{\bar{p}} A_{\bar{p},\bar{s},\bar{i}}|^2. \tag{5.13}$$

This would permit one to eliminate unwanted terms by simply setting all related weighting factors to 0. For instance, to ignore the radial modes in the LG basis, one would set all the weighting factors ($w_{\ell_s,\ell_i,p_s,p_i}$) to 0 for all values of $p_s, p_i > 0$, and the other factors to 1 (or any other desired number). This norm also has a new multi-linear system that can be solved, given by [64]

$$\sum_{\bar{s},\bar{i},\bar{p}_1} w^2_{\bar{s},\bar{i}} A^*_{\bar{s},\bar{i},\bar{p}} A_{\bar{s},\bar{i},\bar{p}_1} \bar{\chi}_{\bar{p}_1} = \sum_{\bar{s},\bar{i}} w^2_{\bar{s},\bar{i}} A^*_{\bar{s},\bar{i},\bar{p}} C_{\bar{s},\bar{i}}. \tag{5.14}$$

whose solution χ'_w presents us with the optimal pump shape in the specified subspace. Under the condition that each of the weightings are set to 1, this reduces to the original minimizer solution that yields a unique solution. By setting some factors to be 0, one essentially discards an equation in the original multi-linear system (Eq. (5.10)), leaving behind more free variables. This allows for the possibility of multiple solutions to exist, although in the event that this occurs, any choice of solution is legitimate to generate the desired pump profile.

This is the mathematical approach to finding the desired beam, which has been kept basis-independent. This pump shaping method has been published and can be found in Ref. [64]. In this study, the approach was validated by using the results (spiral spectrum) from state-of-the-art theories, and reproducing the pump profiles that these papers used as their input [63, 108, 109]. New results were also presented in the HG basis, verifying the basis independence. What follows are two examples of pump shaping using our approach, where the generated pump profiles for the desired spectrum, for both the LG and HG basis, is determined. This was accomplished by means of solving the relevant linear systems on Mathematica.

5.1.1 LG basis

Firstly, the related equations for the pump shaping problem, when the LG basis is used, is shown. The relevant eigenfunction for the LG modes are given by Eq. (1.17). The down-converted SPDC state in this basis reduces to

$$|\Psi_{SPDC}\rangle = \sum_{\ell_s,\ell_i,p_s,p_i} C^{p_s,p_i}_{\ell_s,\ell_i} |\ell_s, p_s\rangle |\ell_i, p_i\rangle, \tag{5.15}$$

with the coefficients given by

$$C^{p_s,p_i}_{\ell_s,\ell_i} = N \int d\mathbf{k}_s d\mathbf{k}_i \, \phi, (LG^{p_s}_{\ell_s})^* \, (LG^{p_i}_{\ell_i})^*, \tag{5.16}$$

and the arbitrary pump profile expressed as

$$\phi_w = \sum_{\ell,p} \chi^p_\ell LG^p_\ell. \tag{5.17}$$

To begin the pump shaping procedure, a desired spectrum with no radial modes were chosen, which had the joint complex probability coefficients of the form C_{ℓ_s,ℓ_i}. Five equal maximum intensity peaks were chosen as the desired spectrum set by $C_{-4,-4} = C_{-2,-2} = C_{0,0} = C_{2,2} = C_{4,4} = \frac{1}{\sqrt{5}}$, such that the resultant spectrum after the pump determination looked as shown in **Figure** 5.1. The desired spectrum, with the 5 chosen equal peaks, is clearly present in the figure, but there is also some 'noisy' peaks present (off-diagonals) likely arising due to some 'leaked' light from the pump beam affecting modes outside of our detection subspace. Despite these unwanted peaks, the method still generates a pump-beam capable of creating the required spectrum.

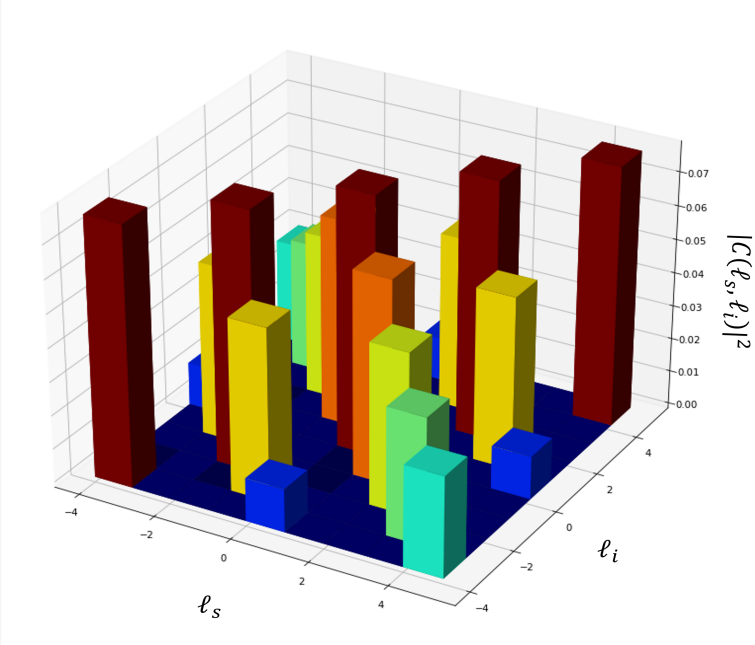


Figure 5.1: LG spectrum from $\ell_{s,i} = -4$ to $\ell_{s,i} = 4$: The desired spectrum with equalized coefficients $C_{-4,-4} = C_{-2,-2} = C_{0,0} = C_{2,2} = C_{4,4} = \frac{1}{\sqrt{5}}$ is shown here.

It turns out that to acquire such a down-converted spectrum, a pump beam formed by a superposition of LG modes is required, whose analytical expression was found to be:

$$\begin{aligned}\phi = {} & 0.14851146\, LG(-8,0) + 0.01979261\, LG(-4,0) + 0.00189168\, LG(0,0) \\ & + 0.01979261\, LG(4,0) + 0.14851146\, LG(8,0).\end{aligned} \tag{5.18}$$

Since the analytical expression is clearly defined, the physical pump profile could be plotted on python yielding what is shown in **Figure** 5.2.

5.1.2 HG basis

Similarly to what was done with the LG basis, the related equations for the HG basis (Eq. (1.13)) is shown.

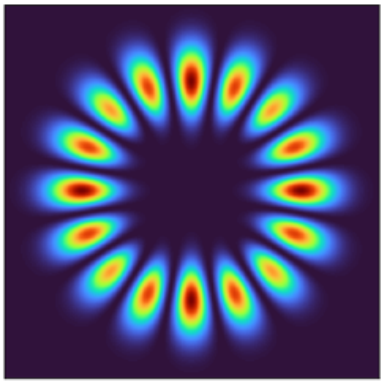


Figure 5.2: LG pump profile: The requisite pump profile for the chosen desired coefficients $C_{-4,-4} = C_{-2,-2} = C_{0,0} = C_{2,2} = C_{4,4} = \frac{1}{\sqrt{5}}$.

The SPDC state in this basis is

$$|\Psi_{SPDC}\rangle = \sum_{m_s,m_i,n_s,n_i} C^{n_s,n_i}_{m_s,m_i} |m_s, n_s\rangle |m_i, n_i\rangle. \tag{5.19}$$

The coefficients here are determined by

$$C^{n_s,n_i}_{m_s,m_i} = N \int d\mathbf{k}_s d\mathbf{k}_i \, \phi, (HG^{n_s}_{m_s})^* \, (HG^{n_i}_{m_i})^*, \tag{5.20}$$

and the expression for the arbitrary pump profile is expressed as

$$\phi_w = \sum_{m,n} \chi^n_m HG^n_m. \tag{5.21}$$

The desired spectrum chosen for this basis was chosen such that all n indices were set to 0, hence leaving only the m indices to be worked with. The joint complex probability coefficients (denoted as C_{m_s,m_i}) selected were $C_{0,0} = C_{1,1} = C_{2,2} = C_{3,3} = C_{4,4} = C_{5,5} = C_{6,6} = C_{7,7} = C_{8,8} = \frac{1}{\sqrt{9}}$, with the corresponding spectrum shown in **Figure** 5.3. This figure indicates the presence of the desired 9 peaks of equal magnitude. There is no appearance of any cross-terms as was the case for the LG basis. This could make sense by comparing the two pump profiles. In the case of the LG basis, the spatial profile is of an annular nature. When choosing a subspace of LG modes, there could always be similar spatial profiles, outside of the desired subspace, resembling the structure of some spatial profiles within the chosen subspace. This means that the issue of 'leaked light' will always be an issue for LG modes. For the HG basis, the spatial profile is of a grid-like nature in the sense that the choice of m and n values stipulate the number of horizontal or vertical dark nodes on the wavefront. No number of strictly horizontal nodes will allow the spatial profile of a beam to resemble that of a beam with strictly vertical nodes. Therefore, if one were to stipulate a subspace of only m-modes (as was the case), there would be no leaked modes arising from the pump profile. This explains why there is no off-diagonal elements for the HG spectrum.

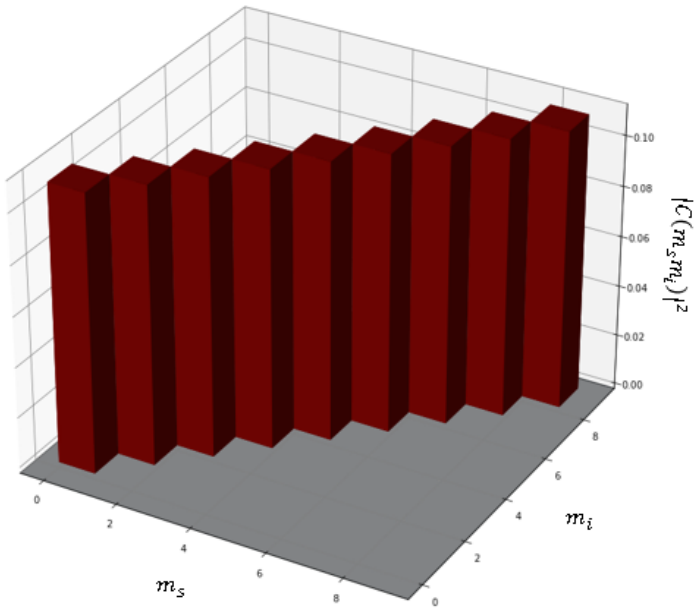


Figure 5.3: HG spectrum from $m_{s,i} = 0$ to $m_{s,i} = 8$: The desired spectrum with coefficients $C_{0,0} = C_{1,1} = C_{2,2} = C_{3,3} = C_{4,4} = C_{5,5} = C_{6,6} = C_{7,7} = C_{8,8} = \frac{1}{\sqrt{9}}$ is shown here.

The analytical expression needed for the pump profile, to acquire such a spectrum, was found to be,

$$\begin{aligned}\phi = {} & 0.00216885\, HG(0,0) + 0.00167313\, HG(2,0) + 0.00137927\, HG(4,0) \\ & + 0.00076836\, HG(6,0) + 0.0002\, HG(8,0).\end{aligned} \tag{5.22}$$

This expression allowed for the plotting of the pump profile, which can be seen in **Figure** 5.4.

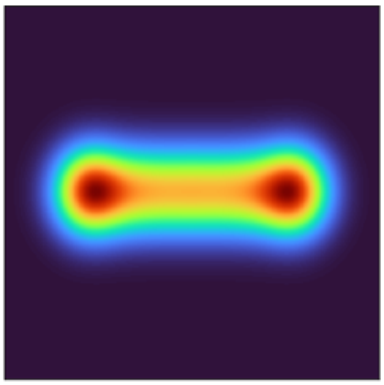


Figure 5.4: HG pump profile: The pump profile for the chosen desired spectrum whose coefficients are given by $C_{0,0} = C_{1,1} = C_{2,2} = C_{3,3} = C_{4,4} = C_{5,5} = C_{6,6} = C_{7,7} = C_{8,8} = \frac{1}{\sqrt{9}}$.

5.2 Chapter conclusion

We have manifested a technique of shaping the pump profile (possibly producing some exotic patterns) such that the entanglement spectrum becomes as desired. This technique is useful in that it is basis-independent for all modes that are solutions to the paraxial Helmholtz equation, and the power comes in that by choosing a desired entanglement spectrum, the algorithm generates the pump profile that would be required.

Chapter 6

Conclusion

In the first chapter, an introduction to the spatial modes of light was presented, with attention drawn to the Laguerre-Gaussian modes, and Hermite-Gaussian modes, which are solutions to the paraxial Helmholtz equation in cylindrical and cartesian coordinates respectively. Concepts related to quantum mechanics and quantum entanglement, specifically applicable in the field of optics and photonics, was also presented here. The concept of entanglement between photons was conveyed, and some measures related to quantifying the degree of entanglement between these photons were also presented.

Since this field is dependent on the structuring of light, one is required to realize methods to perform this tailoring of the field of light. One usually works with the spatial modes of light, which was introduced in the first chapter, it thus makes sense to understand the desire of shaping light into various exotic patterns. In the second chapter, spatial light modulators (SLMs) are introduced which serve as the components of choice in our lab for performing this tailoring of light. A mathematical overview of how these SLMs work, and how efficient they are, is also clearly discussed. The SLMs use what is known as a computer generated hologram to shape the light in the desired way. This hologram is carefully designed to manipulate the phase and amplitude of light, by producing a phase response on the SLM. The method of complex amplitude modulation considered followed the protocol introduced by Victor Arrizon, and is well known for its efficiency in light modulation. These SLMs are not only utilized for shaping the spatial profile of light, but also in the measurements of many properties in quantum experiments.

Possibly the most important of these quantum properties is the phenomenon of photon entanglement. Photon entanglement is a surging topic of interest in recent times, and one method to generate these entangled photons in a lab environment is through the process of spontaneous parametric down-conversion (SPDC). This was detailed in the third chapter. This process occurs when a high frequency initial pump beam of photons impinges on a non-linear crystal, generating two low frequency down-converted photons of longer wavelength. These down-converted photons are entangled with one another and through the use of SLMs, many quantum measures can be performed. The first of these that was discussed is the spiral bandwidth, which effectively displays a probability distribution spectrum corresponding to the entangled photon states. The general trend for when a Gaussian beam is used as the pump beam, is that the probability drops off for higher OAM states. The next measurement that was discussed is the Bell measurement, which verifies that the two photons are indeed entangled. It was shown that if the value of the

Bell measurement violated the CHSH inequality, then the two photons were entangled. The final measurement introduced is related to recreating the quantum state of the two down-converted photons. This is performed through a quantum state tomography measurement where a series of projective measurements is used in a minimization procedure to reconstruct the desired state.

After the theory of these measurements were detailed, an experimental realization of these measurements was demonstrated in chapter 4. This chapter also acted as a description of how to achieve full control over the parameters in an optical setup. Some of these parameters include the perfect alignment, correct crystal temperature, and a perfectly set gating and integration time.

The final chapter introduced the novel work of basis-independent pump shaping. It was discussed in the third chapter that one would strive to equalize the complex probably coefficients between modes. This desire arises since we seek to increase the bandwidth of modes we can use to encode information on photons. The pump shaping procedure introduced in this chapter provides the capability of selecting a desired basis (such as the LG or HG basis). The approach utilizes a tensor minimization technique, whereby a chosen desired entanglement spectrum is stipulated, and the requisite pump profile required to generate such a spectrum is returned as the output.

This methodical pump shaping technique has been designed for bases indexed by discrete countable parameters, such as the Hermite Gaussian, or Laguerre-Gaussian modes. To improve on this aspect, this procedure could be adapted to include bases indexed by continuous parameters, such as the Bessel-Gaussian modes. An additional improvement would be to alter the SPDC parameters and choose other phase matching conditions.

Our pump shaping technique has also only been realized on a theoretical level, by verifying some state-of-the-art results published by the authors. Further work would be to test the theory in an experimental environment, by designing an entanglement spectrum, finding the pump profile, pumping the non-linear crystal with this pump beam, generating the experimental spectrum, and comparing the theoretical prediction with the experimental result. The confirmation of this technique would allow for the implementation of pump shaping in protocols such as quantum teleportation, and quantum key distribution, in an attempt to increase the bandwidth of modes with which we could use to encode information.

Bibliography

[1] Victor Christianto. "A Review of Schrödinger Equation and Classical Wave Equation". In: *Prespacetime Journal* 5.5 (2014).

[2] Jan Faye. "Copenhagen interpretation of quantum mechanics". In: (2002).

[3] D. Griffiths. *Introduction to quantum mechanics Third Edition*. Cambridge University Press, 2017.

[4] Mark Fox. *Quantum optics: an introduction*. Oxford master series in atomic, optical, and laser physics. Oxford: Oxford Univ. Press, 2006. URL: https://cds.cern.ch/record/1001868.

[5] Alvin Bayliss, Charles I Goldstein, and Eli Turkel. "An iterative method for the Helmholtz equation". In: *Journal of Computational Physics* 49.3 (1983), pp. 443–457.

[6] Erich Zauderer. "Complex argument Hermite–Gaussian and Laguerre–Gaussian beams". In: *JOSA A* 3.4 (1986), pp. 465–469.

[7] Anna T O'Neil and Johannes Courtial. "Mode transformations in terms of the constituent Hermite–Gaussian or Laguerre–Gaussian modes and the variable-phase mode converter". In: *Optics communications* 181.1-3 (2000), pp. 35–45.

[8] Bahaa EA Saleh and Malvin Carl Teich. *Fundamentals of photonics*. john Wiley & sons, 2019.

[9] Arnold F Nikiforov and Vasiliĭ Borisovich Uvarov. *Special functions of mathematical physics*. Vol. 205. Springer, 1988.

[10] M Padgett et al. "An experiment to observe the intensity and phase structure of Laguerre–Gaussian laser modes". In: *American Journal of Physics* 64.1 (1996), pp. 77–82.

[11] Stephen M Barnett, Mohamed Babiker, and Miles J Padgett. *Optical orbital angular momentum*. 2017.

[12] Enrique J. Galvez and Nikolay Zhelev. "Orbital angular momentum of light in optics instruction". In: *Tenth International Topical Meeting on Education and Training in Optics and Photonics*. Ed. by Marc Nantel. Vol. 9665. International Society for Optics and Photonics. SPIE, 2007, pp. 48 –53.

[13] David S Simon. "Topology and physics: a historical overview". In: ().

[14] Paul Adrien Maurice Dirac. *The principles of quantum mechanics*. Oxford university press, 1981.

[15] E. Kreyszig. *Introductory functional analysis with applications*. Wiley Classics Library. John Wiley and Sons, Inc., New York, 1989.

[16] Galen C Duree Jr. *Optics for dummies*. John Wiley & Sons, 2011.

[17] Eileen Otte et al. "High-dimensional cryptography with spatial modes of light: tutorial". In: *JOSA B* 37.11 (2020), A309–A323.

[18] Ermes Toninelli et al. "Concepts in quantum state tomography and classical implementation with intense light: a tutorial". In: *Advances in Optics and Photonics* 11.1 (2019), pp. 67–134.

[19] C. Zander. "Classical and quantum dynamics of information and entanglement properties of fermion systems". PhD thesis. University of Pretoria, 2012.

[20] I. Change M. Nielsen. *Quantum Computation and Quantum Information: 10th Anniversary Edition*. 10th. USA: Cambridge University Press, 2011. ISBN: 1107002176.

[21] B. Sanders J. Kim G. Gour. "Limitations to sharing entanglement". In: *Contemporary Physics* 53.5 (2012), pp. 417–432. URL: https://doi.org/10.1080/00107514.2012.725560.

[22] John Langerholc. "Trace Formalism for Quantum Mechanical Expectation Values". In: *Journal of Mathematical Physics* 6.8 (1965), pp. 1210–1218.

[23] Paolo Zanardi and Daniel A Lidar. "Purity and state fidelity of quantum channels". In: *Physical Review A* 70.1 (2004), p. 012315.

[24] D Ter Haar. "Theory and applications of the density matrix". In: *Reports on Progress in Physics* 24.1 (1961), p. 304.

[25] AIP Conference Proceedings 2066. *Introduction to quantum entanglement*. 2019. URL: https://doi.org/10.1063/1.5089051.

[26] Univeristy of Oregon. *Mixed states and pure states*. 2009. URL: https://pages.uoregon.edu/svanenk/solutions/Mixed_states.pdf.

[27] D. Poole. *Linear Algebra: A Modern Introduction*. Cengage Learning, 2014. ISBN: 9781285463247. URL: https://books.google.co.za/books?id=V-UbCgAAQBAJ.

[28] Gunnar Björk, Per Jonsson, and Luis L Sánchez-Soto. "Single-particle nonlocality and entanglement with the vacuum". In: *Physical Review A* 64.4 (2001), p. 042106.

[29] Nicholas A Peters, Tzu-Chieh Wei, and Paul G Kwiat. "Mixed-state sensitivity of several quantum-information benchmarks". In: *Physical Review A* 70.5 (2004), p. 052309.

[30] W. Wootters. "Entanglement of Formation of an Arbitrary State of Two Qubits". In: *Physical Review Letters* 80.2245 (1997). URL: arXiv:quant-ph/9709029.

[31] W. Wootters V. Coffman J. Kundu. "Distributed entanglement". In: *Physical Review Letters* 61.052306 (2000). URL: https://arxiv.org/abs/quant-ph/9907047.

[32] Scott Hill and William K Wootters. "Entanglement of a pair of quantum bits". In: *Physical Review Letters* 78.26 (1997), p. 5022.

[33] Richard Jozsa. "Fidelity for Mixed Quantum States". In: *Journal of Modern Optics* 41.12 (1994), pp. 2315–2323. DOI: 10.1080/09500349414552171.

[34] Shay Keren-Zur et al. "Shaping light with nonlinear metasurfaces". In: *Adv. Opt. Photon.* 10.1 (2018), pp. 309–353. DOI: 10.1364/AOP.10.000309.

[35] Victor Arrizón et al. "Pixelated phase computer holograms for the accurate encoding of scalar complex fields". In: *JOSA A* 24.11 (2007), pp. 3500–3507.

[36] Victor Arrizón. "Complex modulation with a twisted-nematic liquid-crystal spatial light modulator: double-pixel approach". In: *Optics Letters* 28.15 (2003), pp. 1359–1361.

[37] C. Rosales-Guzmán and A. Forbes. *How to Shape Light with Spatial Light Modulators*. 2017.

[38] Jonathan Pinnell et al. "Modal analysis of structured light with spatial light modulators: a practical tutorial". In: *JOSA A* 37.11 (2020), pp. C146–C160.

[39] Yu-Xuan Ren et al. "Experimental generation of Laguerre-Gaussian beam using digital micromirror device". In: *Applied Optics* 49.10 (2010), pp. 1838–1844.

[40] Mohammad Mirhosseini et al. "Rapid generation of light beams carrying orbital angular momentum". In: *Optics Express* 21.25 (2013), pp. 30196–30203.

[41] Stirling Scholes et al. "Structured light with digital micromirror devices: a guide to best practice". In: *Optical Engineering* 59.4 (2019), p. 041202.

[42] Gregor Thalhammer et al. "Speeding up liquid crystal SLMs using overdrive with phase change reduction". In: *Optics Express* 21.2 (2013), pp. 1779–1797.

[43] Jun Liu and Jian Wang. "Demonstration of polarization-insensitive spatial light modulation using a single polarization-sensitive spatial light modulator". In: *Scientific Reports* 5.1 (2015), pp. 1–7.

[44] Vasudevan Lakshminarayanan and Andre Fleck. "Zernike polynomials: a guide". In: *Journal of Modern Optics* 58.7 (2011), pp. 545–561.

[45] Y. H. Hsieh et al. "Integral-based parallel algorithm for the fast generation of the Zernike polynomials". In: *Opt. Express* 28.2 (2020), pp. 936–947. DOI: 10.1364/OE.380567. URL: http://www.osapublishing.org/oe/abstract.cfm?URI=oe-28-2-936.

[46] Thomas Jennewein et al. "Quantum Cryptography with Entangled Photons". In: *Phys. Rev. Lett.* 84 (20 2000), pp. 4729–4732. DOI: 10.1103/PhysRevLett.84.4729. URL: https://link.aps.org/doi/10.1103/PhysRevLett.84.4729.

[47] Rupert Ursin et al. "Entanglement-based quantum communication over 144 km". In: *Nature physics* 3.7 (2007), pp. 481–486.

[48] Michal Horodecki, Pawel Horodecki, and Ryszard Horodecki. "Mixed-state entanglement and quantum communication". In: *Quantum information*. Springer, 2001, pp. 151–195.

[49] Jens Eisert. "Entanglement in quantum information theory". In: *Quant-ph* (2006).

[50] Christophe Couteau. "Spontaneous parametric down-conversion". In: *Contemporary Physics* 59.3 (2018), 291–304. ISSN: 1366-5812. DOI: 10.1080/00107514.2018.1488463. URL: http://dx.doi.org/10.1080/00107514.2018.1488463.

[51] Filippo M Miatto, Alison M Yao, and Stephen M Barnett. "Full characterization of the quantum spiral bandwidth of entangled biphotons". In: *Physical Review A* 83.3 (2011), p. 033816.

[52] Baghdasar Baghdasaryan and Stephan Fritzsche. "Enhanced entanglement from Ince-Gaussian pump beams in spontaneous parametric down-conversion". In: *Phys. Rev. A* 102 (5 2020), p. 052412. DOI: 10.1103/PhysRevA.102.052412. URL: https://link.aps.org/doi/10.1103/PhysRevA.102.052412.

[53] Valentin G Dmitriev, Gagik G Gurzadyan, and David N Nikogosyan. *Handbook of nonlinear optical crystals*. Vol. 64. Springer, 2013.

[54] Christophe Couteau. "Spontaneous parametric down-conversion". In: *Contemporary Physics* 59.3 (2018), pp. 291–304.

[55] Alexander S Solntsev et al. "LiNbO3 waveguides for integrated SPDC spectroscopy". In: *Apl Photonics* 3.2 (2018), p. 021301.

[56] M V Fedorov, Yu M Mikhailova, and P A Volkov. "Gaussian modelling and Schmidt modes of SPDC biphoton states". In: *Journal of Physics B: Atomic, Molecular and Optical Physics* 42.17

(2009), p. 175503. DOI: 10.1088/0953-4075/42/17/175503. URL: https://doi.org/10.1088/0953-4075/42/17/175503.

[57] Suman Karan et al. "Phase matching in β-barium borate crystals for spontaneous parametric down-conversion". In: *Journal of Optics* 22.8 (2020), p. 083501.

[58] Robert W. Boyd. *Nonlinear Optics, Third Edition*. 3rd. USA: Academic Press, Inc., 2008. ISBN: 0123694701.

[59] Bahaa EA Saleh et al. "Duality between partial coherence and partial entanglement". In: *Physical Review A* 62.4 (2000), p. 043816.

[60] SP Walborn et al. "Entanglement and conservation of orbital angular momentum in spontaneous parametric down-conversion". In: *Physical Review A* 69.2 (2004), p. 023811.

[61] HH Arnaut and GA Barbosa. "Orbital and intrinsic angular momentum of single photons and entangled pairs of photons generated by parametric down-conversion". In: *Physical Review Letters* 85.2 (2000), p. 286.

[62] Shilong Liu et al. "Increasing two-photon entangled dimensions by shaping input-beam profiles". In: *Physical Review A* 101.5 (2020), p. 052324.

[63] Alison M Yao. "Angular momentum decomposition of entangled photons with an arbitrary pump". In: *New Journal of Physics* 13.5 (2011), p. 053048. DOI: 10.1088/1367-2630/13/5/053048. URL: https://doi.org/10.1088/1367-2630/13/5/053048.

[64] Nicholas Bornman et al. "Optimal Pump Shaping for Entanglement Control in Any Countable Basis". In: *Advanced Quantum Technologies* 4.10 (2021), p. 2100066.

[65] H Di Lorenzo Pires, HCB Florijn, and MP Van Exter. "Measurement of the spiral spectrum of entangled two-photon states". In: *Physical Review Letters* 104.2 (2010), p. 020505.

[66] Dong-Sheng Ding et al. "Broad spiral bandwidth of orbital angular momentum interface between photon and memory". In: *Communications Physics* 2.1 (2019), pp. 1–8.

[67] CK Law and JH Eberly. "Analysis and interpretation of high transverse entanglement in optical parametric down conversion". In: *Physical Review Letters* 92.12 (2004), p. 127903.

[68] Yingwen Zhang and Filippus S Roux. "Modal spectrum in spontaneous parametric down-conversion with noncollinear phase matching". In: *Physical Review A* 89.6 (2014), p. 063802.

[69] B. Podolsky A. Einstein and N. Rosen. "Can Quantum-Mechanical Description of Physical Reality Be Considered Complete?" In: (1935), pp. 777–780.

[70] Robert B Griffiths. "Quantum locality". In: *Foundations of Physics* 41.4 (2011), pp. 705–733.

[71] Tim Maudlin. "What Bell proved: A reply to Blaylock". In: *American Journal of Physics* 78.1 (2010), pp. 121–125.

[72] Tim Maudlin. "What bell did". In: *Journal of Physics A: Mathematical and Theoretical* 47.42 (2014), p. 424010.

[73] David Bohm. "A suggested interpretation of the quantum theory in terms of" hidden" variables. I". In: *Physical review* 85.2 (1952), p. 166.

[74] Jeffrey Bub. "Quantum Entanglement and Information". In: *The Stanford Encyclopedia of Philosophy*. Ed. by Edward N. Zalta. Summer 2020. Metaphysics Research Lab, Stanford University, 2020.

[75] Helen Dukas and Banesh Hoffmann. "Albert Einstein, the human side: new glimpses from his archives." In: *Albert Einstein* (1979).

[76] E. Schrodinger. "Quantum Theory and Measurement". In: (1936), p. 807.

[77] L. Vaidman. "Quantum Nonlocality". In: *Entropy MDPI* 21.447 (2019). URL: https://www.mdpi.com/1099-4300/21/5/447/pdf-vor.

[78] J. Bell. "On the Problem of Hidden Variables in Quantum Mechanicss". In: *Review of Modern Physics* 38.3 (1966). URL: https://people.isy.liu.se/jalar/kurser/QF/references/Bell1966.pdf.

[79] R. Werner M. Wolf. "Bell Inequalities and Entanglement". In: *Quant-ph* (2001). URL: https://cds.cern.ch/record/518517/files/0107093.pdf.

[80] John F Clauser et al. "Proposed experiment to test local hidden-variable theories". In: *Physical Review Letters* 23.15 (1969), p. 880.

[81] BR Gadway, EJ Galvez, and F De Zela. "Bell-inequality violations with single photons entangled in momentum and polarization". In: *Journal of Physics B: Atomic, Molecular and Optical Physics* 42.1 (2008), p. 015503.

[82] Alain Aspect, Jean Dalibard, and Gérard Roger. "Experimental test of Bell's inequalities using time-varying analyzers". In: *Physical Review Letters* 49.25 (1982), p. 1804.

[83] B Jack et al. "Entanglement of arbitrary superpositions of modes within two-dimensional orbital angular momentum state spaces". In: *Physical Review A* 81.4 (2010), p. 043844.

[84] I.M. Nape. "Hybrid entanglement for quantum communication". PhD thesis. University of the Witwatersrand, 2017.

[85] J Leach et al. "Violation of a Bell inequality in two-dimensional orbital angular momentum state-spaces". In: *Optics Express* 17.10 (2009), pp. 8287–8293.

[86] M.A. de Oliveira. "Quantum cryptography with structured light". PhD thesis. University of the Witwaterstand, 2020.

[87] Megan Agnew et al. "Tomography of the quantum state of photons entangled in high dimensions". In: *Physical Review A* 84.6 (2011), p. 062101.

[88] G Mauro D'Ariano, Matteo GA Paris, and Massimiliano F Sacchi. "Quantum tomography". In: *Advances in Imaging and Electron Physics* 128 (2003), pp. 206–309.

[89] Ugo Fano. "Description of states in quantum mechanics by density matrix and operator techniques". In: *Reviews of Modern Physics* 29.1 (1957), p. 74.

[90] B Jack et al. "Precise quantum tomography of photon pairs with entangled orbital angular momentum". In: *New Journal of Physics* 11.10 (2009), p. 103024.

[91] Nathan K Langford et al. "Measuring entangled qutrits and their use for quantum bit commitment". In: *Physical Review Letters* 93.5 (2004), p. 053601.

[92] K Banaszek et al. "Maximum-likelihood estimation of the density matrix". In: *Physical Review A* 61.1 (1999), p. 010304.

[93] Rob T Thew et al. "Qudit quantum-state tomography". In: *Physical Review A* 66.1 (2002), p. 012303.

[94] Ryszard Horodecki et al. "Quantum entanglement". In: *Reviews of Modern Physics* 81.2 (2009), p. 865.

[95] Sang Min Lee et al. "Polarization-entangled photon-pair source obtained via type-II non-collinear SPDC process with PPKTP crystal". In: *Optics express* 24.3 (2016), pp. 2941–2953.

[96] Fabian Steinlechner et al. "A high-brightness source of polarization-entangled photons optimized for applications in free space". In: *Optics express* 20.9 (2012), pp. 9640–9649.

[97] Chris Monroe. "Quantum information processing with atoms and photons". In: *Nature* 416.6877 (2002), pp. 238–246.

[98] Charles H Bennett and David P DiVincenzo. "Quantum information and computation". In: *Nature* 404.6775 (2000), pp. 247–255.

[99] C. Schaffner A. Broadbent. "Quantum cryptography beyond quantum key distribution". In: *Des. Codes Cryptogr.* 78 (2015), pp. 351–382. URL: https://doi.org/10.1007/s10623-015-0157-4.

[100] Melanie McLaren et al. "Two-photon optics of Bessel-Gaussian modes". In: *Physical Review A* 88.3 (2013), p. 033818.

[101] M Yang et al. "Entanglement concentration for non-maximally entangled states of qudits". In: *Optics Communications* 282.7 (2009), pp. 1482–1487.

[102] Alois Mair et al. "Entanglement of the orbital angular momentum states of photons". In: *Nature* 412.6844 (2001), pp. 313–316.

[103] Ryan S Bennink. "Optimal collinear Gaussian beams for spontaneous parametric down-conversion". In: *Physical Review A* 81.5 (2010), p. 053805.

[104] Shilong Liu et al. "Coherent manipulation of a three-dimensional maximally entangled state". In: *Physical Review A* 98.6 (2018), p. 062316.

[105] SP Walborn et al. "Multimode hong-ou-mandel interference". In: *Physical Review Letters* 90.14 (2003), p. 143601.

[106] Pauline Boucher, Hugo Defienne, and Sylvain Gigan. "Engineering spatial correlations of entangled photon pairs by pump beam shaping". In: *Optics Letters* 46.17 (2021), pp. 4200–4203.

[107] Antonio Z Khoury, Paulo H Souto Ribeiro, and Kaled Dechoum. "Transfer of angular spectrum in parametric down-conversion with structured light". In: *Physical Review A* 102.3 (2020), p. 033708.

[108] Juan P Torres et al. "Preparation of engineered two-photon entangled states for multidimensional quantum information". In: *Physical Review A* 67.5 (2003), p. 052313.

[109] JP Torres, A Alexandrescu, and Lluis Torner. "Quantum spiral bandwidth of entangled two-photon states". In: *Physical Review A* 68.5 (2003), p. 050301.

[110] James C Spall. "Implementation of the simultaneous perturbation algorithm for stochastic optimization". In: *IEEE Transactions on Aerospace and Electronic Systems* 34.3 (1998), pp. 817–823.